Experimental Study of UHPC with High Fire Resistance and Meso-Scale Modelling

by

Xiangwei Liang

A thesis submitted for the fulfilment of the requirement for the degree of

Doctor of Philosophy

School of Civil and Environmental Engineering

Faculty of Engineering and Information Technology

University of Technology Sydney

2018

CERTIFICATE OF ORIGINAL AUTHORSHIP

I certify that the work in this thesis has not previously been submitted for any degree nor has it been submitted as part of requirements for a degree except as fully acknowledged within the text.

I also certify that the thesis has been written by me. And help that I have received in my research work and the preparation of the thesis itself has been acknowledged. In addition, I certify that all information sources and literature used are indicated in the thesis.

Xiangwei Liang

August 2018

ACKNOWLEDGEMENT

I would like to take this special opportunity to express my sincere gratitude to my principal supervisor, Prof. Chengqing Wu for his outstanding guidance, support and encouragement throughout this study. His dedication and personality are inspirational and make him one of my role models. Countless interactions between us through meetings, phone calls and emails ensure my heading in the right direction and help resolve numerous problems and confusions on my research road. Hearty thanks also go to my co-supervisors, A/Prof. Alex Ng and Dr. Jun Li. It was beneficial and pleasing having a talk with them frequently and their invaluable advice and support greatly smooth the path to accomplishing my research project.

I gratefully acknowledge the financial support from the University of Technology Sydney (UTS) for the UTS Doctoral Scholarship and the Faculty of Engineering and Information Technology Top-Up Scholarship. The APA scholarship provided by the University of Adelaide before I transferred my PhD study to UTS on 1 February 2016 is heartily acknowledged as well.

Also, I would like to express my thanks to many of my colleagues and friends. I am grateful to Dr. Fangrui Zhang, Dr. Ye Xia, Dr. Juechun Xu, and Dr. Nimasha Weerasinghamohottige, who were so warm-hearted and provided me with kind guidance and generous help at the beginning of this project. Special thanks go to Dr. Jian Liu, Dr. Weiqiang Wang and Dr. Jianguang Fang for their ongoing support to my research, Dr. Yu Su, Mr. Zhu Chen, Mr. Yekai Yang and Mr. Cheng Wu for their cooperation in the experiments, Dr. Lixiang He and Dr. Kai Liu for their significant support. I would like to convey my sincere gratitude to Dr. Peter Du and my neighbours Mr. Roger Heyne and Mr. Pusheng Zhang for their support in my daily life.

Finally, I would like to extend my love and gratitude to my wife Zoe (You) You and my family for their continuous support and encouragement, without which this project would not have been completed.

LIST OF PUBLICATIONS

Journal Papers

Liang, X., and Wu, C. (2018). "Meso-scale modelling of steel fibre reinforced concrete with high strength." *Construction and Building Materials*, 165, 187-198.

Liang, X., and Wu, C. (2018). "Investigation on thermal conductivity of steel fibre reinforced concrete using meso-scale modelling." *International Journal of thermophysics*, 39: 142. https://doi.org/10.1007/s10765-018-2465-1.

Liang, X., Wu, C., Su, Y., Chen, Z., and Li, Z. (2018). "Development of ultra-high performance concrete with high fire resistance." *Construction and Building Materials*, 179, 400-412.

Liang, X., Wu, C., Yang, Y., and Li, Z. (2019) "Experimental study on ultra-high performance concrete with high fire resistance under simultaneous effect of elevated temperature and impact loading." *Cement and Concrete Composites*, Accepted.

Liang, X., Wu, C.Q., Yang, Y., Wu, C and Li, Z. "Coupled effect of temperature and impact loading on tensile strength of ultra high performance fibre reinforced concrete ." *Composite Structures*, Under review.

Conference Papers

Liang, X., and Wu, C. (2016). "Bond-slip behavior of steel fibre in UHPC under elevated temperature." *The 14th International Symposium on Structural Engineering*, ISSE-14, Beijing, China, 12-15 October.

Liang, X., and Wu, C. (2016). "Effect of steel fibre on thermal behavior of concrete under elevated temperature." *24th Australian Conference on the Mechanics of Structures and Materials*, ACMSM24, Perth, Australia, 6-9 December.

Liang, X., and Wu, C. (2017). "Study on responses of UHPCs under combined effects of impact and high temperature." *6th International Conference on Design and Analysis of Protective Structures* DAPS 2017, Melbourne, Australia, 29

November - 1 December.

LIST OF NOTATIONS

ΔU	change of system internal energy
ΔKE	change of system kinetic energy
ΔPE	change of system potential energy
λ	thermal conductivity
λ_0	thermal conductivity of plain concrete
λ_c	thermal conductivity of concrete
λ_s	thermal conductivity of steel fibre
ϕ_q	heat flux
1D	one-dimensional
2D	two-dimensional
3D	three-dimensional
σ	stress
σ_s	compressive stress in sample
ε	strain
ε_u	ultimate strain

ε_{uT}	ultimate strain under high temperature
ε_r	strain measured on reflection bar
ε_s	strain in sample
$\dot{\varepsilon}_s$	strain rate in sample
ε_t	strain measured on transmission bar
A	cross-section area or contacting area
A_b	bond area
A_s	cross-section area of sample
c	specific heat
c_0	wave velocity
c_c	specific heat of concrete
c_s	specific heat of steel fibre
D	diameter
DA	damage parameter
E	modulus of elasticity
E_0	initial modulus of elasticity

E_{0T}	initial modulus of elasticity under high temperature
E_s	modulus of elasticity of steel fibre
EXP	exponent in damage curve
f	force
f_c	compressive strength
$f_{c20°C}$	compressive strength under 20 °C or room temperature
f_{cT}	compressive strength under high temperature
f_y	yield strength
GB	bond shear modulus
h	convection or film coefficient
l_s	length of sample
q	rate of heat transfer
Q	heat
Q-0	UHPC sample with quartz sand as aggregate but without any fibre
Q-P	UHPC sample with quartz sand as aggregate and with PP fibre
Q-S	UHPC sample with quartz sand as aggregate and with steel fibre

Q-SP	UHPC sample with quartz sand as aggregate and with hybrid PP fibre and steel fibre
R_e	outer radius
S-0	UHPC sample with steel slag as aggregate but without any fibre
S-SP	UHPC sample with steel slag as aggregate and with hybrid PP fibre and steel fibre
$S_{\max}$	the maximum elastic slip
t	time
T	temperature
T_b	temperature of contacting fluid
T_s	temperature of solid surface
u	slip strain per unit length
$u_{\max}$	the maximum slip strain
v	velocity
V	volume
V_f	fibre content by volume
vol.	volume

U	internal energy
W	work

LIST OF ACRONYMS

BFS	Boundary Face Subdivide
CH	calcium hydroxide
C-S-H	calcium silicate hydrate
CFS	constraining facet set
CPS	constraining point set
CSS	constraining segment set
DOF	degree of freedom
DTeS	Delaunay tetrahedron set
DTS(CF)	Delaunay triangle set of constraining facets
FEA	finite element analysis
FRC	fibre reinforced concrete
FSI	Facet Subdivide Iterative
GGBFS	ground granulated blast furnace slag
HPC	high performance concrete
HSC	high strength concrete
K&C	Karagozian & Case

LDPM	lattice discrete particle model
NSC	normal strength concrete
PP	polypropylene
RC	reinforced concrete
RHT	Riedel, Hiermayer and Thoma
SCC	self-consolidating concrete
SCC-S	self-consolidating concrete reinforced with steel fibre
SHPB	split Hopkinson pressure bar
SFRC	steel fibre reinforced concrete
SSI	Segment Subdivide Iterative
UHPC	ultra-high performance concrete
UHPFRCC	ultra-high performance fibre-reinforced cementitious composites

TABLE OF CONTENTS

LIST OF FIGURES

LIST OF TABLES

ABSTRACT

Despite the use of state-of-the-art technology and materials, modern buildings are still vulnerable to fire. Damage made to ultra-high performance concrete (UHPC) by fire or high temperature is usually severer than normal strength concrete (NSC) or high performance concrete (HPC) due to its compact internal structure. For example, strength loss of UHPCs can reach up to 80% after exposure to 800 °C and explosive spalling is a common disaster to UHPCs. To develop a UHPC with high fire resistance, a total of six UHPC mixtures were designed and tested after subjected to elevated temperatures up to 1000 °C in this study. The effects of aggregate type, fibre type and heating rate were investigated. Residual compressive strengths and stress-strain relationships were studied. Besides, attention was paid to explosive spalling. Scanning electron microscope (SEM) analysis was conducted to help understand the mechanism of variation of internal micro-structure under different temperatures. It was found the mixture containing steel slag and hybrid fibre, i.e. steel fibre and polypropylene (PP) fibre, had excellent fire resistance. After being subjected to 1000 °C, this mixture retained a residual compressive strength of 112.8 MPa or a relative value of 69%.

Furthermore, to study the behaviour of the newly developed UHPC under simultaneous effect of fire and blast, both compressive and splitting tensile split Hopkinson pressure bar (SHPB) tests were carried out under combined action of high temperatures up to 800 °C and impact loading. The dynamic tests were done both under high temperatures (hot test) and after cooling down (cool test) and comparisons were made between the two scenarios. Based on the tests on this UHPC, mechanic and physical characteristics under the combined effect were studied. Besides, explosive spalling was observed in the tests and analysed in this work. It was interesting to find PP fibre could play a negative role in preventing explosive spalling between 320 and 380 °C.

To investigate the effect of steel fibre on thermal conductivity of steel fibre reinforced concrete (SFRC) (including UHPC), a meso-scale model for heat analysis was developed. Delaunay triangulation was employed to generate the unstructured mesh for SFRC materials. The model was validated using existing experimental data. Then, it was used

to study how model thickness affected simulation outcomes of thermal conductivity of models with different fibre lengths, by which an appropriate thickness was determined for the later analyses. The validated and optimised model was applied to study of relationships between thermal conductivity and factors such as fibre content, fibre aspect ratio and different parts of an SFRC block by conducting steady-state heat analyses with the finite element analysis (FEA) software ANSYS. The simulation results reveal that presence of steel fibres has an obvious impact on the distribution of temperature and heat flux vector of the SFRC blocks. Besides, fibre content improves thermal conductivity considerably, while fibre aspect ratio only has an insignificant effect.

Based on the Delaunay triangulation meshing method applied above for thermal analysis, a 3D meso-scale model for mechanical analysis of SFRCs is also successfully developed and verified, which has the potential to more accurately simulate behaviour of SFRCs under elevated temperatures in the future. This approach modelling fibre and concrete separately and linking them with slide line contact has the capability to truly reflect the interfacial behaviour of fibre and mortar, and thus achieve high fidelity of numerical simulations. However, meso-scale modelling usually means tremendous complexity and long computational time. This study proposes a model to achieve relatively high computation efficiency, as well as accuracy. Besides, the model has the ability to deal with small specimens cut from SFRC blocks.

CHAPTER 1

INTRODUCTION

1 INTRODUCTION

1.1 Background

Morden buildings are still vulnerable to fire despite the use of state-of-the-art technology and materials. Most recently, a huge fire engulfing a 24-storey residential complex in London claimed more than 80 lives and damaged the structure severely. It can be even worse when a fire is followed by a blast. In 2015, a 40-minute burning in a warehouse incurred two explosions, killing 165 people and destroying 304 buildings in Tianjin China. These days, terrorist attacks may cause disastrous consequences to the community where there are a growing number of high-rise buildings. In the 911 terrorist attack, the collapse of the two World Trade Centre towers after minutes of burning resulted in severe damage of the surrounding buildings and loss of thousands of lives. Unfortunately, to date the commonly used building materials, i.e. steel and concrete, can still be seriously damaged by fire or the combined effect of fire and impact.

Due to disastrous consequences of fire and terrorism, protective structures against fire and blast are gaining more and more attention from governments and researchers. UHPC is an ideal material for this kind of structures. The Portland Cement Association (PCA) defines UHPC as “a high-strength, ductile material formulated by combining Portland cement, silica fume, quartz flour, fine silica sand, high-range water reducer, water, and steel or organic fibers. The material provides compressive strengths up to 29,000 lb per square inch (psi) and flexural strengths up to 7000 psi”. By contrast, normal strength concrete (NSC) and high performance concrete (HPC) are much inferior in performance such as strength, toughness, ductility and durability. Steel fibre distributed into concrete matrix helps absorb more impact energy and thus reduce spalling and scabbing of the UHPC members under dynamic loading. Today, UHPC is largely used in long-span bridges, anti-explosion structures and high-corrosion occasions.

However, UHPCs could experience severe explosive spalling when being exposed to elevated temperatures. To improve fire resistance of concrete, steel fibre and polypropylene (PP) fibre are usually incorporated into concrete mixtures.

Industrial by-products, such as slag and silica fume, have been widely investigated by researchers as replacement of constituents of concrete to achieve environmental benefit as well as better concrete performance. Steel slag is produced under a high temperature of 1,650 °C so that organic, semi-volatile and volatile compounds are removed. Mainly steel slag consists of calcium silicates, ferrites oxides and compounds of iron, magnesium, manganese and alumina. The physical and chemical analyses showed steel slag aggregate is tough, durable, and of relatively high porosity and density. As an ultra-fine reactive powder, silica fume is primarily used in HPCs or UHPCs to improve their mechanical properties.

A lot of exploration has been done on the behaviours of UHPCs reinforced with fibre either subjected to impulsive loading or high temperatures. In recent years, SHPB has been the predominant test facility to investigate response of concretes under impact loading, together with state-of-the-art computing hardware and finite element packages such as LS-DYNA, enabling one to more profoundly and accurately probe into the response of concretes under dynamic load. Under higher strain rate, concretes including UHPCs usually exhibit higher strength, although with little to do with the modulus of elasticity and even being more brittle.

Residual strength of concrete exposed to fire is critical since it relies on the residual strength to prevent the structure from collapsing and provide enough time for evacuation. Some tests have also been done to study residual properties of UHPCs after exposure to high temperature. High temperatures greatly lower UHPCs' ultimate strength, modulus of elasticity and Poisson's ratio but increase their ductility, making a flatter curve of stress versus strain (Aslani and Samali 2013; Lau and Anson 2006). Also, studies revealed that addition of steel fibre to concrete is beneficial to toughness, resistance of explosive spalling and degradation of strength when the concrete is subjected to high temperatures. Some investigations have been done in terms of microstructure of concrete, disclosing that increasing pore pressure due to water evaporating and inhomogeneous thermal strain are the major reasons for spalling and cracking, and dehydration and decomposition of cementitious constituents contribute to performance decay of concretes under high temperatures.

Combination effect of blast loading and high temperature on UHPCs remains a brand-new area to be explored, though a few such studies have been done on normal strength concrete and structural steel, which highlights the coupling effect of strain rate and high temperature. Previous researches focused on either impact response of UHPC under ambient temperature or residual performances of UHPCs after exposure to high temperatures, but few of them have involved combined effect of impulsive loading and high temperatures to investigate UHPCs' behaviour under such a complex scenario. Studies revealed with higher strain rate UHPCs show higher strength and lower toughness. In contrast, UHPCs usually exhibit lower strength but higher toughness under higher temperatures. Moreover, some tests proved that at an impact velocity, higher temperatures usually contribute to higher strain rate. Thus, the coupling effect of strain rate and temperature needs to be explored for UHPC materials under blast and high-temperature loading.

Knowledge of thermal properties of UHPC is a prerequisite to appropriately understand the response of this kind of material subjected to high temperatures. Though some researches have been done on thermal properties of UHPCs under ambient and high temperatures, mainly they were carried out by experimental testing. It is well known experimental study is a costly approach in comparison with numerical study, and thus numerical simulation can on some occasions be a desirable substitute for tests. However, there are very limited investigations, especially through numerical study, on thermal conductivity of UHPCs in the literature. When the focus is on the effect of steel fibre on thermal conductivity of UHPCs, this kind of investigation can be achieved by meso-scale numerical simulation rather than testing only.

In recent years, with the rapid development of computational technology both in hardware and software, meso-scale modelling has increasingly been an attractive approach for researchers to more deeply and accurately investigate the behaviour of composite materials like UHPC. Instead of a homogeneous material usually considered in many numerical studies, concrete is, in fact, a heterogeneous composite consisting of aggregate, cement paste and void. This heterogeneity is even amplified by the addition of fibres. Meso-scale modelling of UHPC is a method that models UHPC components separately, from which some advantages can be expected. For example, the effect of steel fibre with various parameters such as content, aspect ratio and shape can be studied through meso-scale modelling, which can only be done by experiment otherwise. It also makes it easier to choose material models for UHPCs in commercial software such as LS-DYNA.

1.2 Research objectives and scope

The main objective of this research is to investigate behaviour of a newly developed UHPC with high fire resistance when being subjected to combined elevated temperature and impact loading. Physical and mechanical characteristics are the focuses of the static and dynamic experiments conducted in this study. Besides, effect of steel fibre on thermal conductivity of UHPC is numerically studied using a meso-scale modelling approach. The specific objectives of this research are listed as follows:

- To develop a new UHPC with high fire resistance by adding industrial by-products such as slag and silica fume and hybrid fibre to the concrete mixture. Usage of slag can mitigate the issue of disposing of it and is thus considered environmentally friendly.

- To study physical changes when UHPC is exposed to high temperatures. Compared to NSC, UHPC is much more compact in internal micro-structure and thus vulnerable to explosive spalling. Mass loss and colour change are also important indicators of change of UHPC performance under high temperatures and need to be analysed.

- To investigate behaviour of UHPC under quasi-static compression after exposure to high temperatures. Effect of temperature on mechanical properties of UHPC will be revealed.

- To investigate behaviour of UHPC under dynamic loading after exposure to high temperatures. Coupled effect of temperature and impact loading on mechanical properties of UHPC will be experimentally studied.

- To numerically study effect of steel fibre on thermal conductivity of UHPC under different temperatures. A meso-scale UHPC model is to be developed using a Delaunay triangulation algorism for meshing.

- To numerically study effect of steel fibre on mechanical properties of UHPC. A meso-scale UHPC model is to be developed using a Delaunay triangulation algorism for meshing.

This project is concerned with responses of UHPC under high temperature and impact loading. The scope of this work is limited to the following areas:

- Influence of temperature on physical characteristics of UHPC
- Influence of temperature on static performance of UHPC
- Influence of temperature on dynamic performance of UHPC
- Physico-chemical analyses of UHPC under high temperatures
- Numerical analyses of thermal and mechanical properties of UHPC exposed to high temperatures or under room temperature

1.3 Research methodology

In this project, physical and mechanical characteristics of UHPC are experimentally investigated under static compression or dynamic loading after exposure to elevated temperatures. Besides, meso-scale numerical studies are also conducted to investigate thermal and mechanical properties of UHPC.

1.3.1 Development of UHPC with high fire resistance

This study is to develop a UHPC with high fire resistance. To improve fire resistance of concrete, steel fibre and PP fibre are incorporated into the concrete mixtures. However, so far fire resistance of UHPCs remains a problem of concern even though hybrid fibre is used. In the literature, residual compressive strengths of UHPCs are less than 40% of their room-temperature strength after being exposed to high temperatures even below 1000 °C. In this study, by using steel slag as fine aggregate and incorporating other industrial by-products and hybrid fibre, a UHPC with 69% relative residual strength after subjected to 1000 °C has been successfully developed.

1.3.2 Quasi-static tests of UHPC exposed to high temperatures

Totally there were three types of quasi-static tests involved in this study, i.e. static compressive tests both in cooled-down state and hot state and static splitting tensile tests in hot state. The quasi-static compression tests in cooled-down state were carried out for six target temperatures, i.e. 20, 200, 400, 600, 800 and 1,000 °C, while the compressive and tensile tests in hot state were at five target temperatures, i.e. 20, 200, 400, 600 and 800 °C. Under each target temperature, three specimens were prepared and tested allowing for randomness of explosive spalling. Specimens for compressive tests had a cubic shape with a side length of 50 mm in cooled-down state and 100 mm in hot state respectively, while specimens for splitting tensile tests were cylinders with a size of $\Phi 100 \times 50$ mm.

The specimens were heated in an electric furnace. At a time, three specimens were heated until reaching the target temperatures and then they remained under the constant target temperatures for two hours to achieve uniformly distributed temperature throughout the specimens.

1.3.3 SHPB tests of UHPC under high temperatures

In the compressive and splitting tensile SHPB tests, three cylindrical specimens in size of $\Phi 50 \times 25$ mm were used for each case. The SHPB system consisted of 75-mm-diameter pressure bars made of steel and an in-site explosion-protection electric furnace seated between the incident bar and the transmission bar. The electric furnace was mainly made up of tubular heating chamber, explosion-protection layer, furnace flue and thermal insulating layer. The use of the in-site explosion-protection electric furnace contributed to little temperature drop of the heated specimen. The dynamic tests were done both under high temperatures and after cooling down and comparisons were made between these two scenarios. Based on the tests on this UHPC, mechanic and physical characteristics under the combined effect were studied.

1.3.4 Numerical simulation of thermal conductivity of UHPC

A meso-scale model was developed to investigate the effect of steel fibre on thermal conductivity of UHPC. Delaunay triangulation was employed to generate the unstructured mesh for SFRC materials. The model was validated using existing experimental data. Then, it was used to study how model thickness affected simulation outcomes of thermal conductivity of models with different fibre lengths, by which an appropriate thickness was determined for the later analyses. The validated and optimised model was applied to study of relationships between thermal conductivity and factors such as fibre content, fibre aspect ratio and different parts of a UHPC block applying steady-state heat analyses with FEA software ANSYS.

1.3.5 Numerical simulation of mechanical properties of UHPC

Based on Delaunay triangulation, a 3D meso-scale model is successfully developed and verified. This approach modelling fibre and concrete separately and linking them with slide line contact has the capability to truly reflect the interfacial behaviour of fibre and mortar, and thus achieve high fidelity of numerical simulations. However, meso-scale modelling usually means tremendous complexity and long computational time. This study proposes a model to achieve relatively high computation efficiency, as well as accuracy. Besides, the model has the potential to deal with small specimens cut from UHPC blocks.

1.4 Research significance and contribution to knowledge

Study on properties of UHPCs under a combination of temperatures and impact loading is very limited and coupling effect of these two phenomena on UHPCs needs to be investigated. Outcomes of this study can be applied to design for protective structures built with UHPCs. As a novel approach, meso-scale modelling is employed in this study, which makes it possible to numerically study effect of steel fibre on thermal properties of UHPCs. Overall, the major contributions of this study include:

- So far, fire resistance of UHPCs remains a problem of concern. In the literature, residual compressive strengths of UHPCs are less than 40% of their room-temperature strength after being exposed to high temperatures below 1000 °. In this study, by using steel slag as fine aggregate and incorporating other industrial by-products and hybrid fibre, a UHPC with 69% relative residual strength after subjected to 1000 °C has been successfully developed.
- The newly developed UHPC with excellent fire resistance was experimentally investigated. Firstly, quasi-static compressive and splitting tensile tests were conducted under elevated temperatures up to 1,000 °C. Reinforced with hybrid fibre, this concrete greatly decreased the occurrence of explosive spalling. Then, to reveal its responses to simultaneous impact loading and high temperature, dynamic tests were also carried out

after the specimen was heated up to 800 °C. A self-designed Split Hopkinson Pressure Bar (SHPB) system with heating facility was applied to the tests. Comparison was made between SHPB tests under elevated temperatures and after cooled down. Also, effect of temperature on tensile strength was compared with on compressive strength of the UHPC.

- Meso-scale modelling is developed and adopted in this project. Instead of a homogenous material usually considered in many numerical studies, concrete is a heterogeneous composite consisting of aggregate, cement paste and void. In meso-scale modelling of UHPCs, fibres are explicitly modelled so that their influence on UHPC properties is able to be worked out. Meso-scale modelling models UHPC components separately, by which it is much easier to find an appropriate material model for each component than the integrated composite when conducting numerical analyses. In this study, a new 3D meso-scale model is developed to numerically investigate how steel fibre affects thermal and mechanical properties of UHPC. In some cases, instead of fabricated as a whole, test samples were cut or drilled out from a concrete block, such as specimens for thermal tests and SHPB tests. The numerical model developed in this project has the capability to accurately capture this situation where a simulated UHPC sample is cut from a UHPC block, thereby, ensuring high fidelity. This feature is particularly important and necessary when studying very small specimens where random fibres are unable to be created within the model directly. To model UHPCs appropriately, Delaunay triangulation algorism is employed to mesh the two components, ensuring that the randomly distributed fibres and the concrete matrix connect each other by nodes correctly.

1.5 Layout of the thesis

This thesis consists of seven chapters and their content is as follows:

Chapter 1: This chapter describes background of the project, research objectives and scope, research methodology, research significance and contribution to knowledge.

Chapter 2: This chapter provides a review of literature on behaviour of concrete including UHPC under high temperature or combined effect of high temperature and impact loading.

Besides, it introduces some researches in the literature on meso-scale modelling, heat analyses of concrete and interfacial behaviour between steel fibre and concrete matrix.

Chapter 3: This chapter presents the development of a new UHPC with high fire resistance. Physical characteristics and static mechanical properties of UHPC after exposure to high temperatures are experimentally investigated.

Chapter 4: This chapter provides an experimental study of coupled effect of high temperature and impact loading on compressive strength of the previously developed UHPC either in hot state or cooled-down state. Compressive SHPB tests were carried out using a self-designed SHPB test system which included a heating facility.

Chapter 5: This chapter provides an experimental study of coupled effect of high temperature and impact loading on splitting tensile strength of the previously developed UHPC either in hot state or cooled-down state using the self-designed SHPB test system. Also, static compressive tests and splitting tensile tests were carried out in hot state.

Chapter 6: This chapter presents a numerical study on thermal conductivity of UHPC/SFRC under various temperatures using meso-scale modelling approach. Effect of steel fibre on thermal conductivity has been investigated.

Chapter 7: This chapter carries out a numerical study on mechanical properties of UHPC/SFRC using meso-scale modelling approach. In this study, simulations of uniaxial compression, flexural tension and splitting tension are conducted so that the model is successfully verified. Then, parameter study is carried out on effect of steel fibre on properties of SFRCs.

Chapter 8: This chapter highlights main contributions of this project and recommendations for future research.

Finally, references and appendices are presented at the end of this thesis.

CHAPTER 2

LITERATURE REVIEW

2 LITERATURE REVIEW

2.1 Concretes under impact loading

It is well known that concrete either plain or with fibre is sensitive to strain rate induced by impact loads. Usually, concrete materials are stronger and tougher when subjected to impulsive loading than static loading (Banthia et al. 1996). Grote et al. (2001) carried out an experimental study on dynamic behaviour of concrete under high strain rates using an SHPB test facility, suggesting the load capacity of concrete and mortar was remarkably increased with high strain rates, as seen in Figure 2.1. Figure 2.2 shows clearly that this strain-rate dependence of strength became even more evident when the strain rate was higher than $10^2\ s^{-1}$.

Lots of investigators have found UHPCs reinforced with steel fibre have much better resistance over NSC when suffering dynamic loading. Banthia et al. (1996) and Hrynyk and Vecchio (2014) stated fibre can effectively improve fracture energy absorption under impact loading. Hrynyk and Vecchio (2014) also found that under impact loading the dominant failure model of all the test slabs, which were designed such that they would be governed by flexural failure under static loading, was punching shear failure. The only slab preventing punching contained the largest fibre volume fraction, indicating steel fibre improves tensile strength of concrete noticeably. Under a test of hard projectile impact to concrete plates with dimensions of $40 \times 40 \times 4\ cm^3$, it was observed that specimens with steel fibre suffered reduced damage on both front and rear surfaces compared to those without steel fibre, and at failure steel fibre was pulled out from the concrete matrix instead of being fractured (Dancygier and Yankelevsky 1999). Under projectile impact, several response types of concrete could happen: radial crack, spalling, penetration, scabbing, plugging and perforation (Sovják et al. 2015).

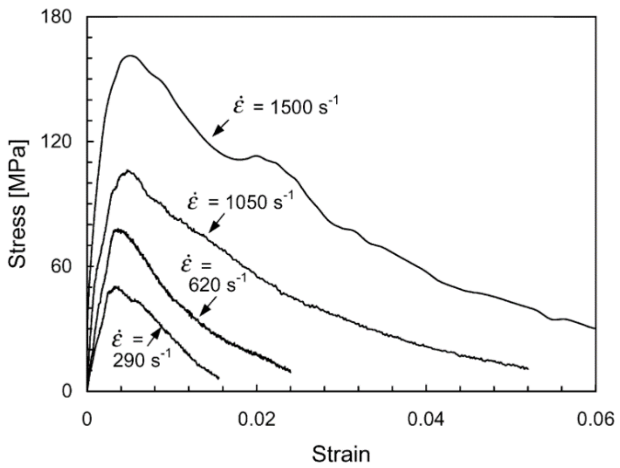

Figure 2.1. stress-strain curves under different strain rate (Grote et al. 2001).

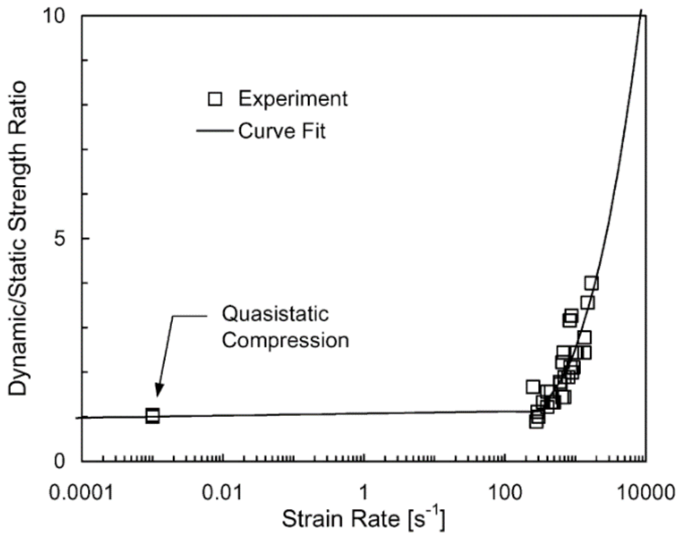

Figure 2.2. strain rate versus normalized compressive strength (Grote et al. 2001).

2.2 Concretes exposed to elevated temperature

Previous studies revealed that mechanical properties of concrete deteriorate severely under elevated temperatures above 400 °C. A series of tests to investigate the static mechanical properties of concrete subjected to elevated temperatures were conducted (Jia 2011). Jia depicted the variation of properties under different temperatures as shown in Figure 2.3, Figure 2.4, Figure 2.5, where f_{cT} , ε_{uT} and E_{0T} are compressive strength, ultimate strain and initial modulus of elasticity of concrete under high temperature, respectively, and f_c, ε_u and E_0 are compressive strength, ultimate strain and initial modulus of elasticity of concrete under ambient temperature. Under elevated temperatures, the stress and strain relationship of concrete is shown in Figure 2.6. Under elevated temperature, compressive behaviour was analysed on HPC with different cementitious constituent and with fibre or without fibre (Poon et al. 2004). The authors found when the temperature reached up to 600 °C and 800 °C, the studied properties of HPCs had the same deteriorating trend with all other studied concretes, but with the quickest loss of modulus of elasticity and the least degradation of toughness. They also observed the ultimate strain was as about 2.3 or 2.9 times as that of the HPCs under ambient temperature when heated to 600 °C and 800 °C, respectively.

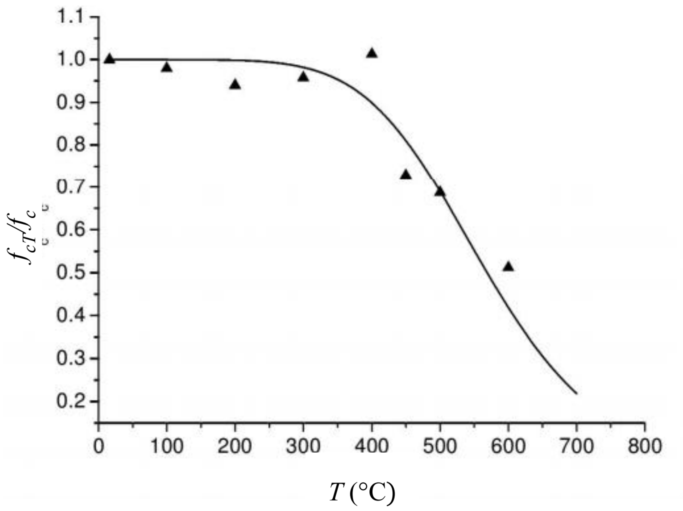

Figure 2.3. Normalized compressive strength vs temperature (Jia 2011).

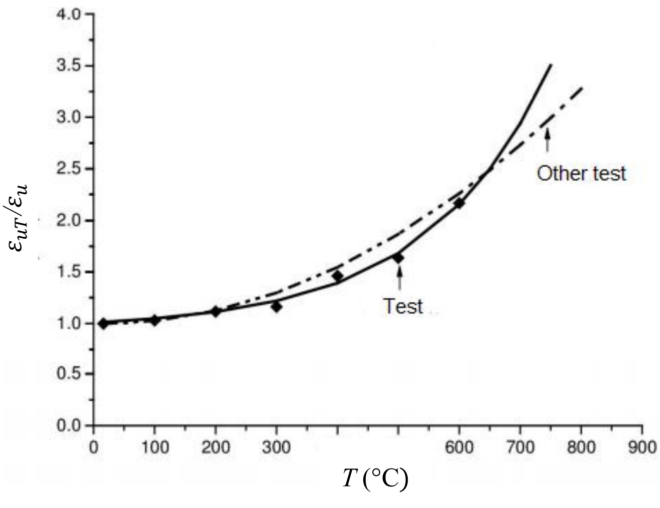

Figure 2.4. Normalized ultimate strain vs temperature (Jia 2011).

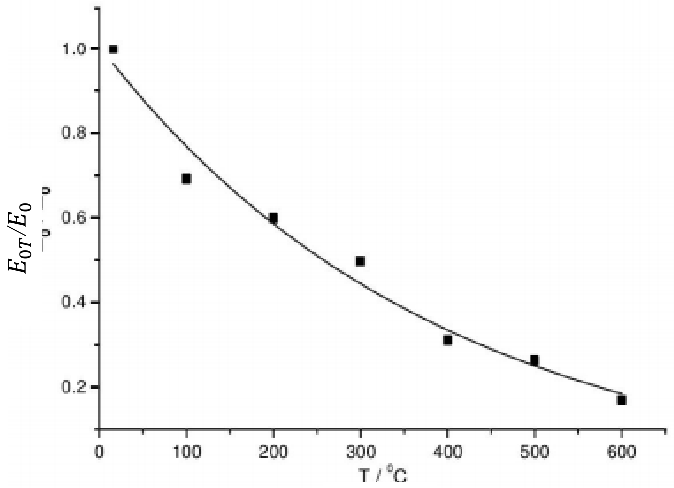

T (°C)

Figure 2.5. Normalized modulus of elasticity vs temperature (Jia 2011).

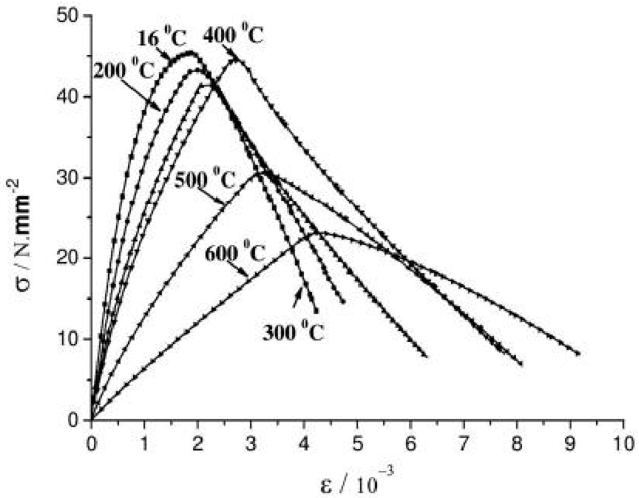

Figure 2.6. Stress-strain curve at various temperatures (Jia 2011).

HPC is usually more compact and higher in compressive strength than NSC. But when exposed to high temperature, compressive strength of HPC degrades more sharply than the latter (Chan et al. 2000). It was found properties of concrete under fire were higher than those heated to the same temperatures but subsequently cooled down to ambient temperature (Hager 2013), as shown in Figure 2.7, suggesting the most appropriate way to capture mechanical properties of concrete at high temperatures is to do that when the specimens are as 'hot' as they are.

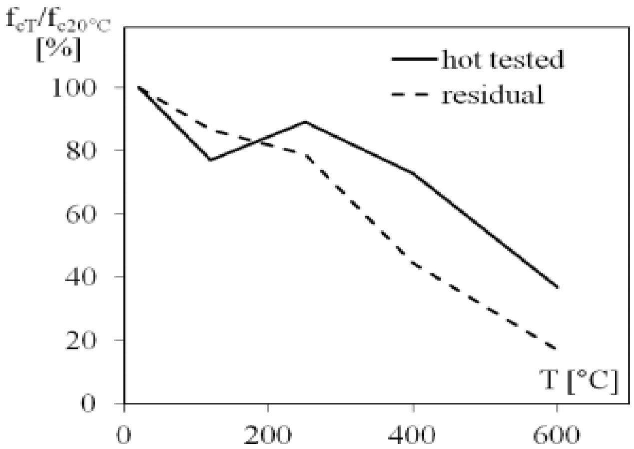

Figure 2.7. Comparison of compressive strength between specimens tested hot and cooled-down (Hager 2013).

A number of researchers studied properties of concrete exposed to elevated temperatures in terms of concrete constituents or microstructure. Pore pressure, thermal strain incompatibility and dehydration were considered as the major contributions to vulnerability of concrete under high temperatures. A comparative experimental study was conducted to investigate porosity and pore size distribution of NSCs and HPCs with steel fibre, PP fibre or without fibre (Chan et al. 2000). The authors found the major difference in cumulative pore volume between NSCs and HPCs under ambient temperature was where the micropores had diameters smaller than 0.4 μm, and the value for NSCs was obviously larger than that of HPCs. After heated to high temperature, pore sizes of both NSCs and HPCs grew larger, with difference of microstructure between NSCs and HPCs becoming even greater. Resorting to relationship curves of $dV / d\log D$ against $\log D$, where V is mercury intrusion volume and D is pore diameter, the authors also noticed that before high temperature NSCs and HPCs had different pore size distribution characteristics, while after high temperature they had similar distribution characteristics. Under high temperature, HPCs with steel fibre exhibited a mild variation of porosity in comparison with NSCs and HPCs with PP fibre or without any fibre. The peak of $dV / d\log D$ for both NSCs and HPCs occurring within 0.1 to 0.15 μm of pore diameter indicated that both NSCs and HPCs were most severely affected by high temperature. It was proposed that initial saturation percentage negatively affected properties of concrete under high temperatures and properties of concrete were severely degraded by high temperatures, though with a little improvement by addition of steel fibre (Lau and Anson 2006).

To investigate explosive spalling and residual mechanical properties of fibre reinforced HPCs under high temperatures, experiments were carried out using concretes integrated with steel fibre, PP fibre or hybrid fibre of the two (Peng et al. 2006). The researchers concluded fibre reinforced concrete, especially with steel fibre, had much higher fracture energy than plain concrete. After heated to above 400°C, residual fracture energy of fibre reinforced concrete increased significantly in comparison with in ambient temperature, although its residual strength decreased greatly. The authors attributed this to fibre pull-out process and aggregate interlocking. Compared to concrete under ambient temperature, concrete under high temperatures especially above 300°C exhibited different damage modes as shown in Figure 2.8, with damage surface usually occurring along the interface of aggregate and paste or within the paste other than through aggregate (Jia 2011). Jia also found explosive spalling damage tended to happen when concrete was heated to a range of 300 °C to 400 °C. However, under higher temperatures, the concrete specimen seemed to be softened and loosened as seen in Figure 2.9.

Figure 2.8. Damage characteristics under ambient (left) and 400°C (right) temperature (Jia 2011).

Figure 2.9. Two types of damage under 400°C (Jia 2011).

2.3 Concretes under combined effect of elevated temperature and impact loading

In recent years, some investigations have been carried out on concretes under combined effect of elevated temperature and impact loading, though few of them specifically on concretes reinforced with steel fibre.

SHPB has been a prevailing testing technique for impact loading tests and has been validated by a lot of researchers (Huo et al. 2013; Huo et al. 2012; Jia 2011; Liu et al. 2011; Su et al. 2014). Stress-strain relationship and energy-absorbing property were investigated after steel fibre reinforced concrete was exposed to high temperatures via SHPB tests (Wang et al. 2014; Yang and Ba 2009). Influence of temperature and addition of fibre to concrete was studied by means of SHPB system (Jin et al. 2013). SHPB test system can also be applied to many other materials such as rocks (Zhu et al. 2012) and alloys (Lee et al. 2011).

An example of SHPB test setup is shown in Figure 2.10, and Figure 2.11 illustrates the components of the SHPB testing system. An SHPB facility consists of an incident (also reflection) bar, a transmission bar and a strike bar, with the test specimen placed between the incident bar and the transmission bar. SHPB is based on propagation theory of one-dimensional elastic wave in a bar, displacement continuity and stress equilibrium at the interface (Huo et al. 2012). During testing an impact loading is produced by the strike bar launched by compressed air, which induces a longitudinal incident pulse ε_i in the incident bar. When the incident wave reaches the interface between the specimen and the bar, a reflected pulse and a transmitted pulse are produced in the incident bar and transmission bar, respectively. A typical incident, reflected and transmitted waves are shown in Figure 2.12. The stress, strain and strain rate can be expressed as follows:

$$\sigma_s(t) = E \cdot A \cdot \varepsilon_t(t) / A_s \tag{2.1}$$

$$\varepsilon_s = -2c_0 (\int_0^t \varepsilon_r \mathrm{d}t) / l_s \tag{2.2}$$

$$\dot{\varepsilon}_s = -2c_0 \cdot \varepsilon_r / l_s \tag{2.3}$$

where E, c_0, and A are the modulus of elasticity, wave velocity and cross-section area of the bars respectively; A_s is the cross-section area and l_s is the length of the specimen; and t is time; σ_s, ε_s, $\dot{\varepsilon}_s$ are the compressive stress, strain and strain rate respectively; ε_t and ε_r are the strains measured on the transmission bar and reflection bar, respectively.

Figure 2.10 SHPB test setup (Huo et al. 2012).

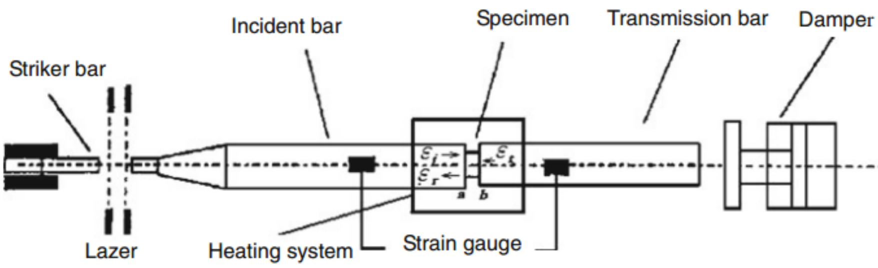

Figure 2.11. SHPB schematic diagram (Huo et al. 2012).

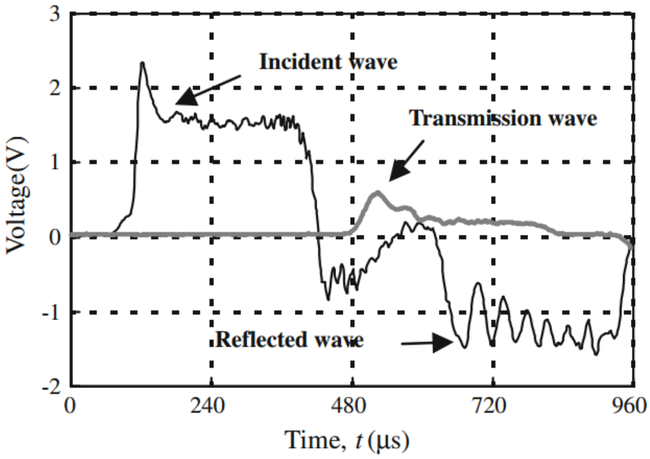

Figure 2.12. Typical incident, reflected and transmission wave (Huo et al. 2012).

As for heating, the most used facility is electrical furnace (Huo et al. 2012) and microwave oven (Jia 2011). To reduce the chances of cracking and spalling of concrete being heated, heating rate needs to be controlled (Liu et al. 2011). Bursting is a risk for concrete heated by a microwave oven. Heat loss needs to be reduced as much as possible during testing to simulate behaviour of concrete under constant temperatures, as showing in Figure 2.13 (Jia 2011).

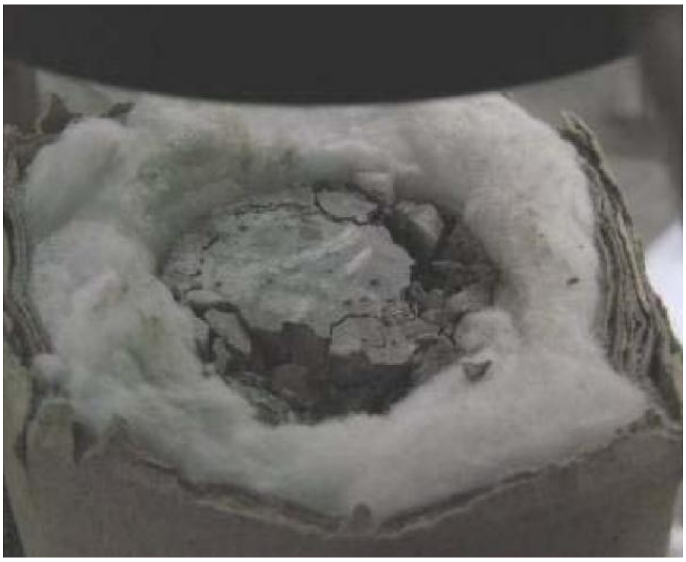

Figure 2.13. Heat insulation (Jia 2011).

Unlike effect of separate loading of either impact loads or high temperature, coupling effect of combined loading of these two phenomena needs to be considered when concrete is subjected to these two loads simultaneously, which was clearly demonstrated by the tests (Su et al. 2014). As can be seen from Figure 2.14, at the same projectile velocity, the induced strain rates are different at different temperatures. High temperature usually leads to deterioration of properties but strain rate can enhance strength of concrete, and effect of high temperatures obviously outweighs that of strain rate (Liu et al. 2011).

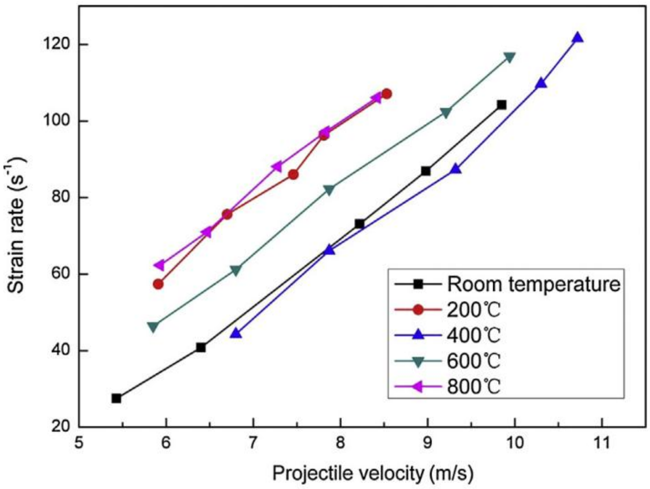

Figure 2.14. Strain rate vs projectile velocity at different temperatures (Su et al. 2014).

It has been found by many researchers that effect of strain rate exists on concrete under whatever degrees of temperatures. With increase of strain rate, concrete exhibits higher strength under certain temperatures. As seen in Figure 2.15, increase ratios (slope) at different temperatures are nearly the same (Su et al. 2014). Regardless of temperature, dynamic compressive strength improves with increase of strain rate, and normalized strength has a linear relation with the logarithm of strain rate (Liu et al. 2011), as seen in Figure 2.16. Test results showed that fire damaged concrete still experienced remarkable strain rate effect and the dynamic stress versus strain relations of fire-damaged concrete were significantly different from those of concrete at room temperature (Huo et al. 2012), as shown in Figure 2.17.

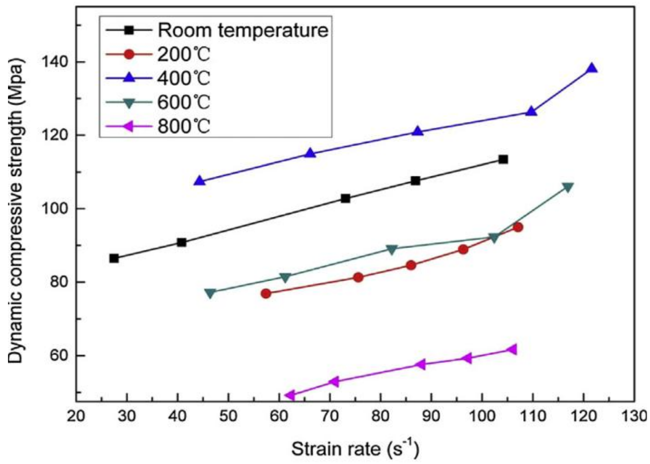

Figure 2.15. Dynamic compressive strength vs strain rate under different temperatures (Su et al. 2014).

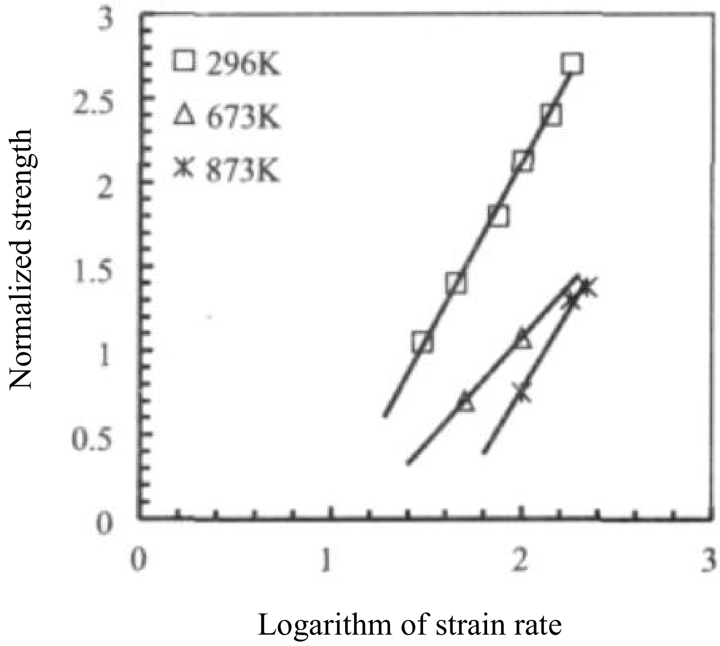

Figure 2.16. Normalized strength vs logarithm of strain rate under different temperatures (Liu et al. 2011).

As mentioned above high temperature has a disadvantage effect on performances of concrete under either static loading or impact loading. Dehydration and degradation due to high temperature result in a reduction of strength and modulus of elasticity, and furthermore, local thermal differential dilatation can lead to cracking and spalling (Kakogiannis et al. 2013). Reduction of elastic modulus due to high temperature is more evident than compressive strength, and with increase in strain rate, the decrease ratios at elevated temperatures descend (Su et al. 2014). Under a certain strain rate, normalized strength of concrete has a linear relation with the logarithm of normalized temperature as shown in Figure 2.18 (Liu et al. 2011). Experimental study (Huo et al. 2012) showed with increase of temperature, the fire damaged concrete experienced a significant loss of strength and modulus of elasticity, while the peak strain had an obvious growth, as shown in Figure 2.19. Under different temperatures and strain rates, the damage forms of concrete are shown in Figure 2.20 (Su et al. 2014).

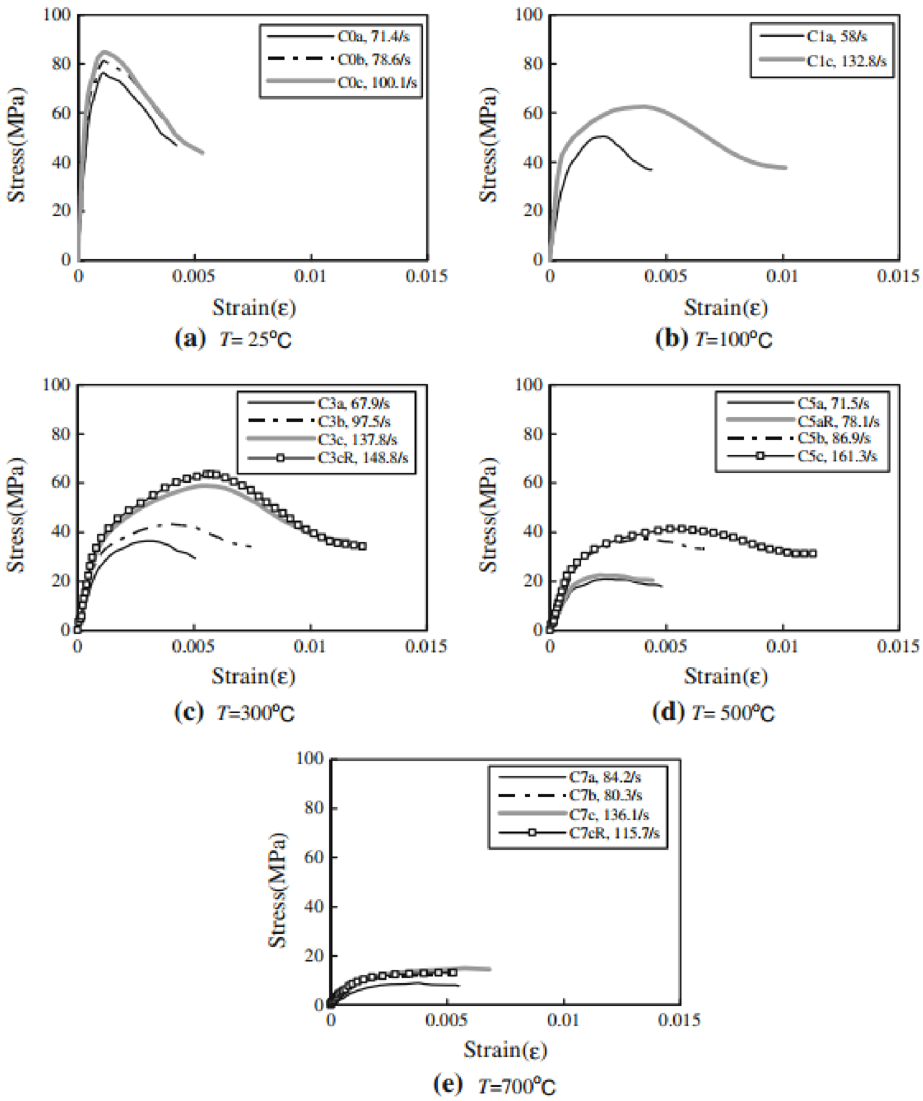

Figure 2.17. Effect of strain rate on stress-strain relation (Huo et al. 2012).

Note: C denotes circular section; and 0, 1, 3, 5 and 7 denote room temperature, 100, 300, 500 and 700 °C respectively; a, b and c denote the specimens of the same impact velocity group; the last letter R denotes a repeated test.

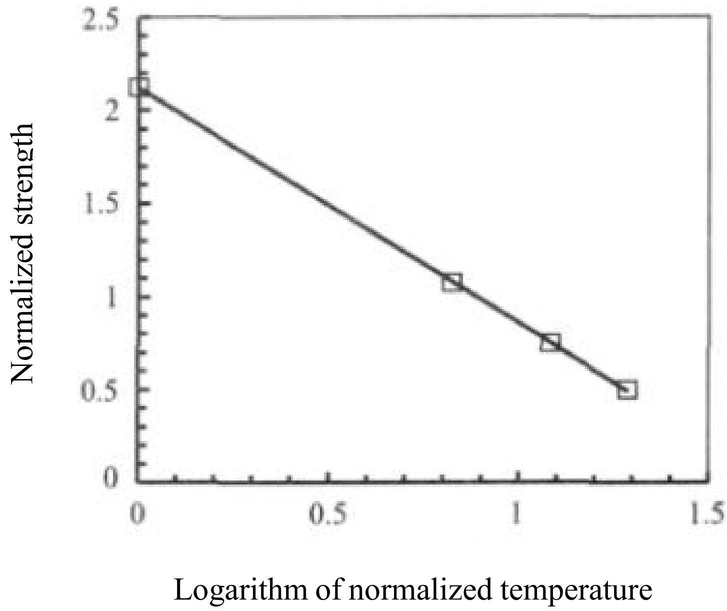

Figure 2.18. Normalized strength vs logarithm of normalized temperature for concrete under strain rate of 100/s (Liu et al. 2011).

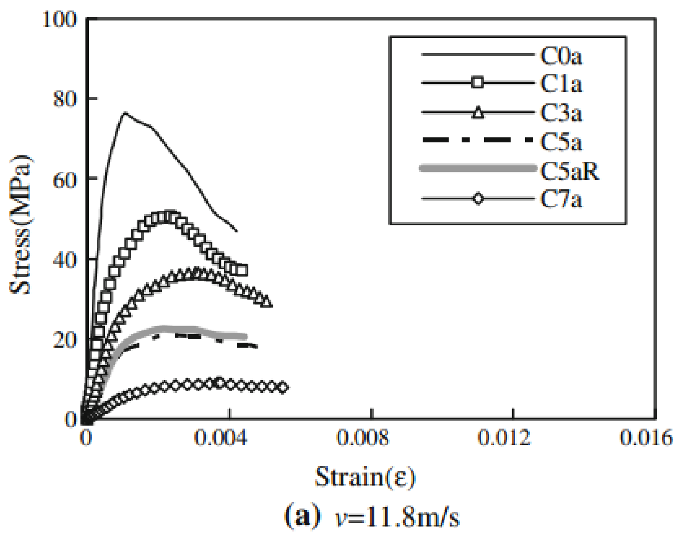

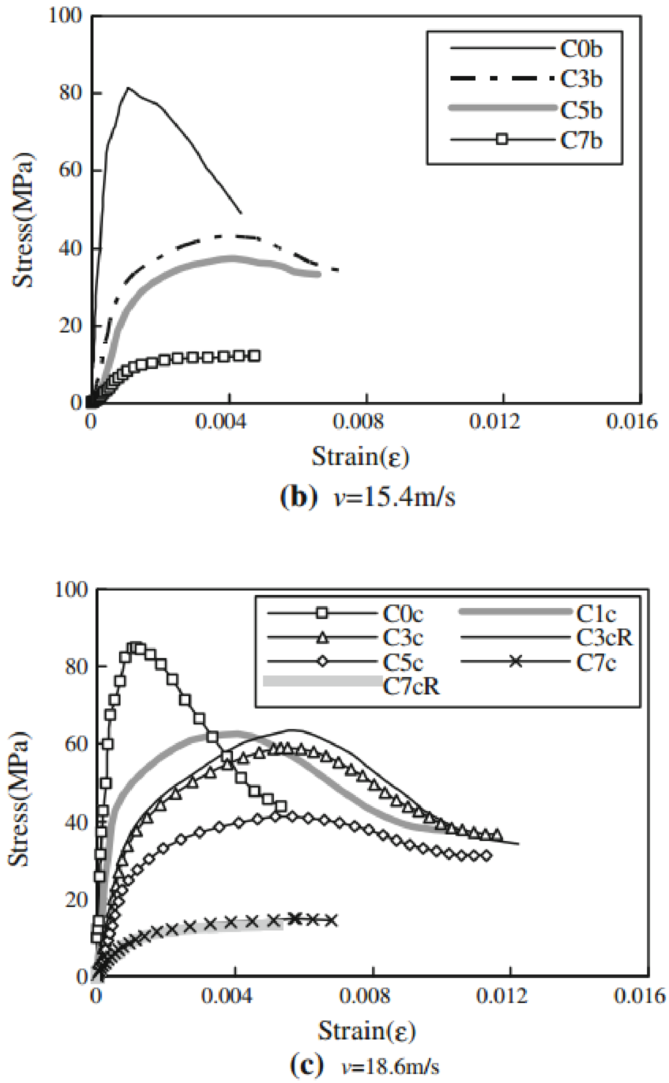

Figure 2.19. Effect of high temperature on stress versus strain relations (Huo et al. 2012).

Note: same as in Figure 2.17

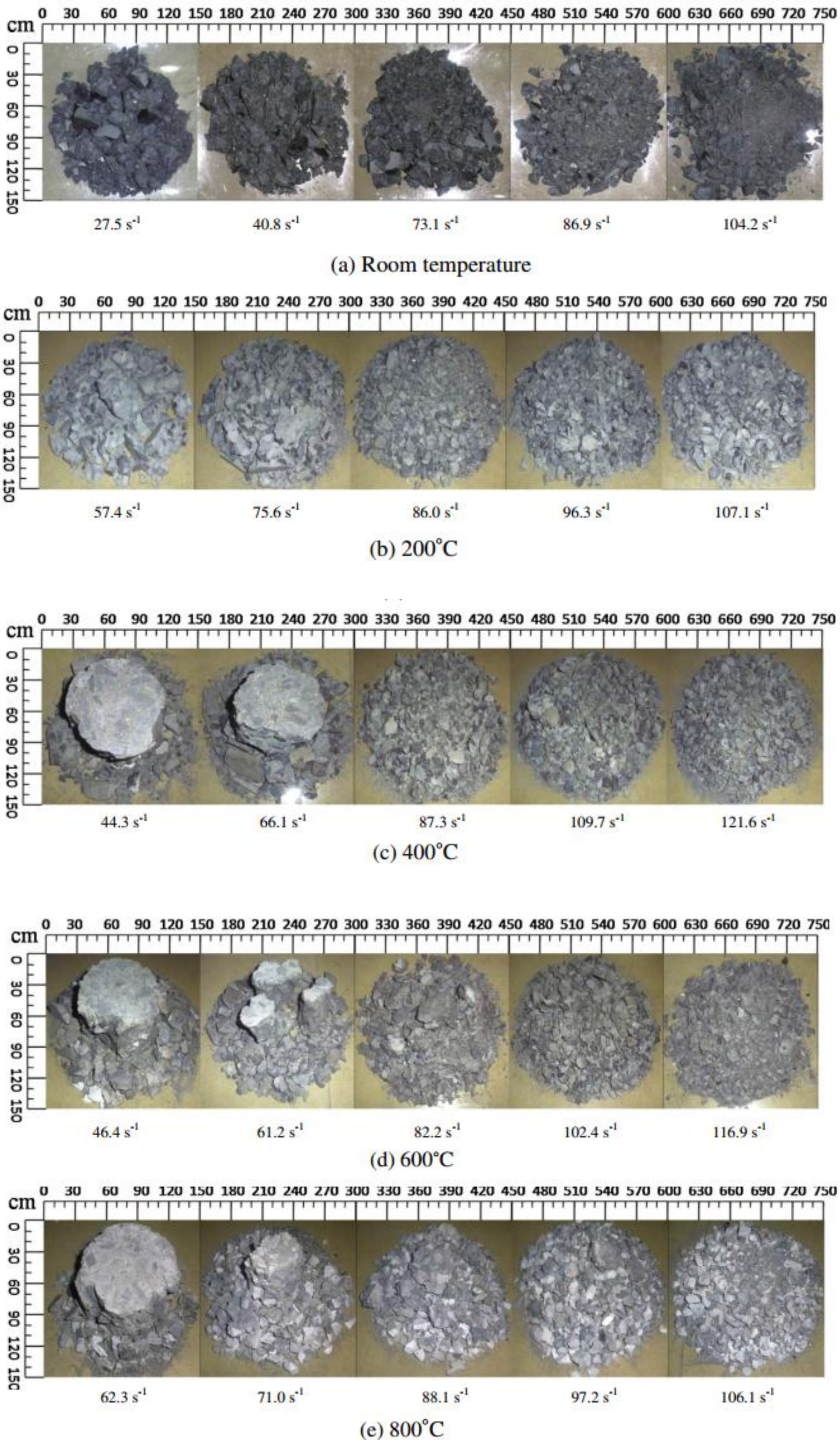

Figure 2.20. Damage forms of concrete under various temperatures and strain rates (Su et al. 2014).

2.4 HPC & UHPC under elevated temperature or combined effect of elevated temperature and impact loading

Due to rampant terrorism, governments and researchers are paying growing attention to protective structures against blast and fire. UHPC is considered as a desirable material for this kind of structures. The Portland Cement Association (PCA) defines UHPC as "a high-strength, ductile material formulated by combining portland cement, silica fume, quartz flour, fine silica sand, high-range water reducer, water, and steel or organic fibers. The material provides compressive strengths up to 29,000 pounds per square inch (psi) (or 200 MPa – the author) and flexural strengths up to 7,000 psi (or 48 MPa – the author)." UHPC has very high compressive strength (usually above 120 MPa) and excellent durability. By contrast, NSC and HPC are much inferior in performance such as strength, toughness, ductility and durability. In the last decades, a lot of effort has been made to improve mechanical properties of UHPC. For example, most recently some nano materials were investigated as a new additive to UHPCs (Su et al. 2016; Su et al. 2017). However, fire or high temperature is still a great threat to all kinds of concretes including UHPCs.

An experimental study was done on the behaviour of HPC subjected to high temperatures up to 800 °C (Chan et al. 2000) and the researchers found the compressive strength of HPCs degraded more sharply than NSCs. Similar findings were obtained by others (Choe et al. 2015; Lee et al. 2015). A comparative study on ultra-high performance fibre-reinforced cementitious composites (UHPFRCC) was carried out before and after heat treatment (Sobia et al. 2015). The test results revealed the residual compressive strength of UHPFRCC after being exposed to 1,000 °C was around 41% of its room-temperature strength. Much severer deterioration was observed by some investigators (Choe et al. 2015; Xiong and Liew 2016; Xiong and Liew 2015). The study (Choe et al. 2015) suggested the relative residual compressive strength of ultra-high-strength concrete being heated to 1,000 °C was only 2%. Another threat a fire can pose to UHPCs is explosive spalling and severe explosive spallings were observed by some researchers (Kahanji et al. 2016; Kahanji et al. 2016). It was proposed that increasing pore pressure due to water evaporating and thermal strain were the major reasons for concrete spalling (Akca and Özyurt Zihnioğlu 2013; Lin et al. 1996). UHPCs usually suffer more serious spalling than

NSCs due to their compact structure and low porosity. Therefore, it is of high significance to develop UHPCs that have better fire resistance.

Industrial by-products, such as slag and silica fume, have been widely investigated by researchers as replacement of constituents of concrete to achieve environmental benefit as well as better concrete performance. Steel slag is produced under a high temperature of 1,650 °C so that organic, semi-volatile and volatile compounds are removed. Mainly steel slag consists of calcium silicates, ferrites oxides and compounds of iron, magnesium, manganese and alumina. The physical and chemical analyses showed steel slag aggregate is tough, durable, and of relatively high porosity and density (Ducman and Mladenovič 2011). An experimental study was conducted to investigate effect of steel slag powder on workability and durability of concrete (Guo et al. 2014). They found compared to addition of ground granulated blast furnace slag (GGBFS) alone to concrete, combined admixture of GGBFS and steel slag could achieve lower dry shrinkage and better abrasion resistance. Especially, when activators such as desulphurization, residue sodium sulphate and desulphurization gypsum were integrated, steel slag significantly improved resistance of the concrete to chloride permeation and water permeation and carbonisation depth. Steel slag was studied as a coarse aggregate in concrete (Netinger et al. 2011) and the authors concluded steel slag could be an acceptable aggregate of concrete for structural use and posed no risk in terms of corrosion of reinforcement. The effect of steel slag was investigated at different replacement ratios of fine aggregate (Qasrawi et al. 2009). The researchers proposed use of steel slag in concrete could greatly enhance strength of concrete, especially tensile strength, if appropriate ratio of steel slag to cement was used. Effect of high temperatures on concrete with inclusion of slag has also been studied by several researchers. It was observed that the residual compressive strength of specimens containing blast-furnace slag or coal bottom ash was lower than the reference concrete that did not contain any slag or coal bottom ash (Yüksel et al. 2011). A study (Netinger et al. 2013) suggested steel slag as coarse aggregate could improve fire resistance of concrete only if it was combined with a binder that was able to better adapt to slag expansion under high temperature or used as a partial replacement for coarse aggregate. Silica fume is an ultra-fine reactive powder and inclusion of it can improve properties of concrete particularly in compressive strength, bond strength and abrasion resistance due to pozzolanic reactions between silica fume and free calcium hydroxide (CH) in the cement paste (Su et al. 2016).

To date, some efforts have been made to investigate influence of incorporation of slag into UHPCs (Ambily et al. 2015; Pyo and Kim 2017) or other types of concretes (Al-Jabri et al. 2011; Biskri et al. 2017; Netinger et al. 2012; Netinger et al. 2013). However, there are currently very limited researches with respect to the effect of slag on the performance of UHPCs subjected to high temperatures. As discussed above, UHPCs could experience severe explosive spalling and suffer dramatic strength loss after being exposed to elevated temperatures. On the other hand, steel slag, as a potential desirable aggregate of refractory concrete, is still dumped as a land-fill material in a significant amount today (Ducman and Mladenovič 2011). This study is to develop a UHPC with high fire resistance. To improve fire resistance of concrete, steel fibre and PP fibre are usually incorporated into concrete mixtures (Akca and Özyurt Zihnioğlu 2013; Chan et al. 2000; Nagy and Szagri 2016; Su et al. 2017; Zheng et al. 2012). PP fibre is broadly considered beneficial to control explosive spalling since it melts at around 160 °C, leaving a network of escaping channels for vapour and thus helping reduce internal vapour pressure (Akca and Özyurt Zihnioğlu 2013; Aslani and Samali 2013; Debicki et al. 2012; Hager 2013; Peng et al. 2006). However, so far fire resistance of UHPCs remains a problem of concern even though hybrid fibre is used. In the literature, residual compressive strengths of UHPCs are less than 40% of their room-temperature strength after being exposed to high temperatures below 1000 °C (Xiong and Liew 2016; Xiong and Liew 2015; Zheng et al. 2012).

There are also quite a few of studies on dynamic behaviour of UHPCs in the literature (Bindiganavile et al. 2002; Li et al. 2015; Rong et al. 2010; Sovják et al. 2015; Su et al. 2016; Su et al. 2016; Wu et al. 2009). However, no investigation has been done to UHPC under coupled effect of high temperature and impact loading.

Apart from compressive strength, tensile strength is another important property of concrete. Tensile strength plays a vital role in determining capacities of tension, shear and punch of structural members, such as columns and beams. For a structure, failure due to lack of these capacities could result in catastrophic consequences since it usually happens abruptly without any omen. Especially, under elevated temperatures, degradation in tensile strength should be carefully evaluated given that tensile strength could be more severely damaged than compressive strength (Faiyadh and AI-Ausi 1989; Israngkura Na Ayudhya 2015). Under combined effect of high temperature and impact loading, such as in a fire followed by a gas explosion, tensile strength of UHPCs is worth studying since it is an important factor affecting resistance of the structure to the shock wave. However, almost no study has been done on either static or dynamic tensile strength of UHPCs under high temperatures, despite a few on other types of concretes (Israngkura Na Ayudhya 2015; Khaliq and Kodur 2011; Tanyildizi and Coskun 2008; Xargay et al. 2018).

To investigate tensile performance of concretes, compared to direct tension test, splitting tension test is usually preferable since it is much easier to carry out and has more reliable test results. Some researchers suggested splitting tensile strength of concretes could be sharply reduced after exposure to high temperatures up to 800 °C (Khaliq and Kodur 2011; Tanyildizi and Coskun 2008). It was even found residual tensile strength of plain concrete decreased to almost zero under high temperatures over 600 °C (Faiyadh and AI-Ausi 1989). A temperature between 300 and 400 °C can be a critical temperature point beyond which loss of tensile strength will be much faster than below it (Gao et al. 2012; Khaliq and Kodur 2011; Khaliq and Kodur 2011). An experimental study (Khaliq and Kodur 2011) investigated properties of high performance self-consolidating concrete at high temperatures and the authors proposed that rapid reduction of splitting tensile strength over 400 °C could be attributed to the excessive cracks induced by thermal stress and component incompatibility. Similar conclusions can be found in other studies (Ma et al. 2015; Novák and Kohoutková 2017; Xargay et al. 2018).

Like compressive strength, splitting tensile strength of concretes is sensitive to strain rate (Zhao et al. 2016). With increase of strain rate, splitting tensile strength tends to rise, sharply after the strain rate exceeds a certain value. Under high temperatures, however, some differences were observed that the dynamic increase factor (DIF) of tensile strength decreased with increase of strain rate after the strain rate was beyond 300 /s (Caverzan et al. 2013). The authors also suggested up to 400 °C DIF could be higher at higher temperatures.

2.5 Effect of steel fibre on thermal conductivity of SFRC/UHPC

Some investigations have been carried out into the performance of fibre reinforced concretes (FRCs) after exposure to high temperatures (Aslani and Samali 2013; Aslani and Samali 2013; Chan et al. 2000; Khaliq and Kodur 2011; Lau and Anson 2006; Peng et al. 2006). When subjected to high temperatures, SFRCs retain relatively high performance in comparison with NSCs without steel fibres (Khaliq and Kodur 2011; Lau and Anson 2006; Poon et al. 2004). However, to appropriately understand how SFRCs respond to fire, it is essential to well know thermal properties such as thermal conductivity of SFRCs under high temperatures. A study (Lin et al. 1996) revealed temperature difference between different parts of a concrete specimen could result in internal cracking due to the developed thermal stress when subjected to rapid heating. This indicates low thermal conductivity of concrete could be a considerable factor for spalling of concrete exposed to fire. As an excellent heat conductor, steel fibre added to concrete may improve the thermal conductivity of the latter and thus reduce its probability of occurrence of cracking or spalling. In some other cases such as where SFRCs are employed as high abrasion-resistant dies in the moulding process of metal and polymer products, it is also important to investigate their capability of heat loss (Corinaldesi and Moriconi 2012). Therefore, it is worth studying how steel fibres affect thermal conductivity of SFRCs.

Earlier researchers (Kodur and Khaliq 2011; Kodur and Sultan 2003) studied the effect of high temperature on thermal properties of high strength concrete (HSC), and they suggested that presence of steel fibre has some effect on thermal conductivity but little on specific heat, while the type of aggregate has a significant influence. They also concluded that temperature notably affects thermal properties of HSCs. With rising temperature, thermal conductivity usually decreases while specific heat fluctuates dramatically at a couple of temperature points. A study (Lie and Kodur 1995) investigated thermal and mechanical properties of SFRCs under high temperatures up to 1000 °C and found steel fibres added into concrete have little impact on thermal properties in comparison with effect on mechanical properties. However, it was proposed that the increase of steel fibres enhances thermal conductivity as well as mechanical performances and thermal conductivity has a positive relationship with the density of the mixture by an experimental study (Gül et al. 2007).

2.6 Meso-scale modelling of SFRC/UHPC on thermal properties

Instead of a homogenous material usually considered in many numerical studies, concrete is a heterogeneous composite consisting of aggregate, cement paste and void. This heterogeneity is even furthered by the addition of fibres. In meso-scale modelling of SFRCs, fibres are explicitly modelled so that their influence on SFRC properties is able to be worked out. Meso-scale modelling models SFRC components separately, by which it is much easier to find an appropriate material model for each component than the integrated composite when conducting numerical analyses. In recent years, some researchers have applied meso-scale modelling to analyses of mechanical properties of SFRCs (Cunha et al. 2012; Fang and Zhang 2013; Gal and Kryvoruk 2011; Häfner et al. 2006; Marfia and Sacco 2003; Oliver et al. 2012; Pros et al. 2012; Su et al. 2017; Wang et al. 1999; Xu et al. 2012). For heat analyses, a meso-scale model was created to iteratively deduce the thermal conductivity of the concrete to agree with the test results, with both steel fibre and concrete modelled as solid elements (Nagy et al. 2015). However, solid element mode for both fibre and concrete led to high modelling complexity. Besides, with all fibres contained within the concrete matrix, their model was unable to represent situations where specimens are cut from an SFRC block or to study properties of different parts of a specimen.

In this study, a new meso-scale model is developed to numerically investigate how steel fibre affects thermal properties of SFRCs, and it is validated against test results from other researchers. In some cases, instead of fabricated as a whole, test samples were sliced from a concrete block for thermal tests (Khaliq and Kodur 2011). The numerical model developed in this study has the capability to accurately capture this situation where a simulated SFRC sample is cut from an SFRC block (see Figure 2.21), thereby ensuring high fidelity. Figure 2.21 illustrates how an edge-section model which has one surface cut and a middle-section model which has two opposite surfaces cut are obtained from an SFRC block. This feature is particularly important and necessary when studying very small specimens where random fibres are unable to be created within the model directly. To model SFRCs appropriately, Delaunay triangulation algorism is employed to mesh the two components, ensuring that the randomly distributed fibres and the concrete matrix connect each other by node correctly. It should be noted as stated by (Miloud 2005; Nagy et al. 2015) adding steel fibres to concrete mixture could result in variations of density and porosity of the concrete, while thermal conductivity of concrete is subject to density (Nagy and Szagri 2016) and porosity (Ganjian 1990). Also, moisture content and thermochemical behaviour under elevated temperatures could affect thermal properties of concrete. These factors are not considered in this thesis since it is difficult to numerically and quantitatively analyse the relationships between fibre ratio and these factors and between thermal properties and these factors.

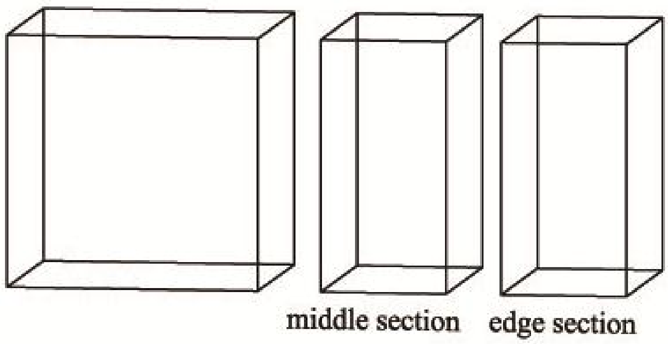

Figure 2.21. Models cut from an SFRC block.

2.7 Meso-scale modelling of SFRC/UHPC on mechanical properties

With excellent mechanical properties, SFRC including UHPC has been widely studied experimentally and numerically in recent decades. In these years, with the rapid development of computational technology both in hardware and software, meso-scale modelling has increasingly been an attractive approach for researchers to more deeply and accurately investigate the behaviour of composite materials like SFRC (Caggiano et al. 2012). Meso-scale modelling of SFRC is a method that models SFRC components separately, from which some advantages can be expected. For example, the effect of steel fibre with various parameters such as content, aspect ratio and shape can be studied through meso-scale modelling, which can only be done by experiment otherwise. To the best knowledge of the authors, there is no material model specially developed for SFRC in commercial software. Most of the previous and current numerical studies take material models of NSC to model SFRC material by adjusting material parameters according to test results. Some researchers (Nyström and Gylltoft 2011) applied the material model developed by Riedel, Hiermayer and Thoma (RHT) model and empirical relations between fracture energy and parameters describing softening curve for SFRCs to conduct a comparative study on the dynamic response of NSCs and SFRCs. Size effects of ultra-high performance steel fibre reinforced concrete (UHPFRC) beams was studied by modelling UHPFRC as a homogeneous material (Mahmud et al. 2013). A study (Xu and Wille 2014) was carried out for calibration of the Karagozian & Case (K&C) concrete model in LS-DYNA to obtain more proper parameters for modelling UHPC. However, it was far from practice since the outcomes came only from a single case of UHPC with the compressive strength of 150 MPa, and without accounting for variation of steel fibre contents. Meso-scale modelling facilitates selection of material models that are readily there in FEM codes such as ANSYS and LS-DYNA.

The point of meso-scale modelling is to establish appropriate interaction mechanisms between reinforcement and concrete. The behaviour of the interface of reinforcement and cementitious matrix has been studied by a lot of researchers. Shannag et al. (Shannag et al. 1997) conducted tests to inspect pull-out behaviour of steel fibres from cement-based composites. Soetens et al. (Soetens et al. 2013) and Tuyan and Yazıcı (Tuyan and Yazıcı 2012) investigated the pull-out behaviour of single hooked-end fibres and found hooked-end fibres have better interfacial bond than smooth or straight fibres. Shi et al. (Shi et al. 2009) and Ganesan et al. (Ganesan et al. 2014) carried out an investigation on bond-slip properties of steel bar and concrete matrix. As reinforcement in concrete, steel fibre has some similar features with the steel bar in terms of reinforcement effect on the concrete matrix, but usually with different damage forms. Upon failure, fibre is usually pulled out from matrix rather than fractured. It was concluded that a complete pull-out process can be divided into three stages: completely bonded state, partially bonded state and completely debonded state (Aslani and Nejadi 2012). Corresponding to different stages, there are different bond stress distributions on the interface. Aslani and Nejadi (Aslani and Nejadi 2012) observed that the bond characteristics of fibre-matrix depend on several factors, including fibre orientation, embedded fibre length, shape of fibres, and strength of matrix. In numerical simulation, to make concrete and fibre work together appropriately, the rule reflecting this interfacial feature needs to be established. Usually, nodes of fibre can be merged or coupled with concrete. Alternatively, slide line contact can be created between a string of nodes of fibre (called slave nodes) and a string of nodes of concrete (called master nodes), which is represented by the keyword *contact_1D in the hydrocode LS-DYNA. Obviously, slide line contact mode is a more realistic and accurate way than merged nodes or perfect bond since it can mimic fibre pull-out process.

Marfia and Sacco (Marfia and Sacco 2003) implemented an analysis of crack propagation in cohesive materials with consideration of fibre debonding and pull-out. Oliver et al. (Oliver et al. 2012) proposed a new formulation to model SFRCs and designed a 2D model. Xu et al. (Xu et al. 2012) produced a 2D axisymmetric meso-scale model modelling coarse aggregate, cementitious mortar and steel fibre separately to study the effect of aggregate distribution, fibre distribution and fibre content on SFRCs under impact loading. The model was able to yield more detailed and realistic internal stress and strain distributions compared with homogeneous models. However, it was limited to 2D and the assumed perfect bond behaviour both between aggregates and mortar and between fibres and mortar is an unrealistic way to represent the interfacial properties. Gal and Kryvoruk (Gal and Kryvoruk 2011) conducted a meso-scale analysis of fibre reinforced concrete (FRC) using a two-step homogenization method. Based on the micromechanical model of fibre bridging proposed by Yang et al. (Yang et al. 2008), Schauffert and Cusatis (Schauffert and Cusatis 2012) integrated fibre effect into their previous lattice discrete particle model (LDPM) to develop a new meso-scale model LDPM-F for FRCs, which was also applicable to SFRCs. The LDPM-F model had similar constitutive laws to the microplane model introduced by Bažant and Caner (Bažant and Caner 2005; Bažant and Caner 2005) and treatment of fibres to that of Bolander et al. (Bolander et al. 2008). Nevertheless, this model simulated fibre pull-out phenomena indirectly and it depended on nine material parameters such as bond fracture energy, bond frictional stress and slip hardening-softening parameter, which made it very difficult to collect sufficient experimental data for accurate calibration of these parameters. Besides, it was not specified whether this model had the ability to deal with specimens that are cut from an FRC block. A finite element model with discretely embedded elements was proposed by Cunha et al. (Cunha et al. 2012) to study properties of SFRCs, which considered SFRCs as a two-phase material consisting of fibre and concrete. However, a fracture plane had to be predefined making their approach unsuitable for general simulations. Su et al. (Su et al. 2017) developed a cylindrical meso-scale model to simulate the dynamic response of ultra-high performance concrete (UHPC) in Split Hopkinson tension tests. UHPC was treated as a two-phase material composed of concrete and fibres. A pull-out test was conducted to obtain parameters for bond slip contact behaviour between concrete and fibres. To avoid the complexity of meshing fibre and concrete conformably, Pros et al. (Pros et al. 2012) proposed a 2D meso-scale model preluding mesh matching between the two materials using immersed boundary method. However, the constitutive model for the fibres in their study has to account for bond slip behaviour between the fibres and the concrete, which depends on angles between the fibre and normal direction of the failure pattern. But it brought about another complexity since the orientation of each fibre has to be worked out. Fang and Zhang (Fang and Zhang 2013) developed a 3D meso-scale model for HSCs reinforced with steel fibres. Delaunay triangulation was adopted by the authors to deal with the meshing of the HSC specimens. Nevertheless, with their Delaunay triangulation strategy, all fibre endpoints have to be contained within the model but not on the surfaces. The shortcoming of their model is that it cannot be used for SFRC specimens prepared by cutting from an SFRC block (see Figure 2.21). Finally in their Delaunay process, initiating a boundary point set may introduce unnecessary points for the Delaunay triangulation, and thus enlarge the already great FE model scale meaninglessly.

2.8 Bond-slip behaviour of steel fibre in UHPC under elevated temperature

It is well acknowledged that inclusion of steel fibres into concrete can greatly improve its mechanical properties, particularly in tensile strength, shear strength and toughness. After exposure to elevated temperatures, concrete with steel fibres usually remains much higher residual strength than concrete without fibres (Chan et al. 2000; Poon et al. 2004). A lot of numerical studies have been done to investigate behaviours of concrete reinforced with steel fibres in the previous decades. There are several available constitutive models for concrete in some hydrocodes such as LS-DYNA. Nevertheless, there is no model specifically developed for concrete with fibres, e.g. UHPCs. Obviously, a more proper and accurate approach is to model concrete and fibre separately, which makes choosing a suitable material model for concrete easier. Fang and Zhang (2013) employed 3D meso-scale modelling that models randomly distributed fibres within a concrete domain to investigate response of high strength concrete subjected to impact loading under room temperature. This novel approach highlights the significance of investigating interfacial behaviour between concrete and fibres, which has been studied by some researchers. It was proposed that bond stress-slip relationship between concrete and steel rebar depends on bar diameter, concrete compressive, tensile strength, cover thickness, geometry of bar deformations (ribs), and steel yield strength (Shi et al. 2009). The bond-slip model they used in their research is called *contact_1D in (LS-DYNA 2013), where the bond-slip relation is considered as a row of springs. They also concluded that the bond-slip behaviour on blast-induced response of reinforced concrete (RC) columns depends more on bond shear modulus than elastic limit slip. As reinforcement in concrete, steel fibre has some similar features with steel bar in terms of interaction mechanism with the matrix, but usually with different damage forms. When it fails, fibre is usually pulled out from the matrix other than broken. Researches indicated that the pull-out process can be divided into three stages: completely bonded state, partially bonded state and completely debonded state (Aslani and Nejadi 2012; Liu et al. 2009), as shown in Figure 2.22. It was stated that stress transfer between fibre and concrete depends on chemical adhesion, friction and mechanical locking (Liu et al. 2009). They also suggested that the higher modulus of elasticity, the larger length and the smaller radius or equivalent radius the fibre has, the more force the fibre can transfer. It was observed the bond characteristics of fibre-matrix depend on several factors, which include fibre orientation, embedded fibre length, shape of the fibres, and strength of the matrix (Aslani and Nejadi 2012).

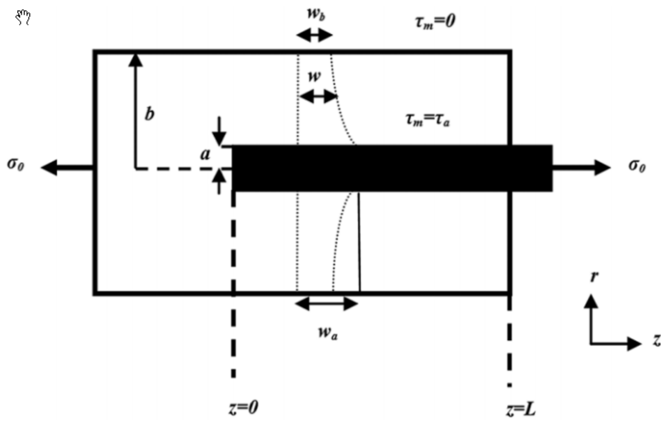

(a) Stage 1: completely bonded

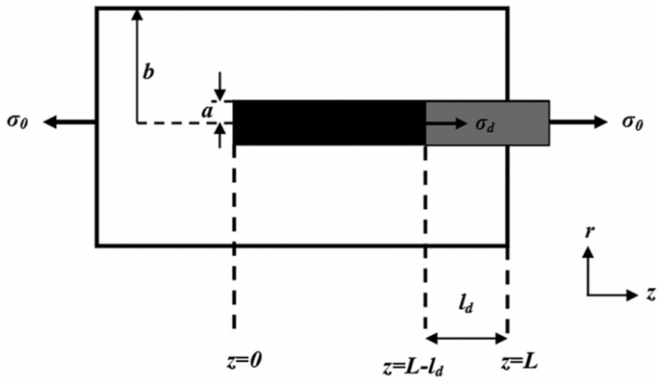

(b) Stage 2: partially bonded

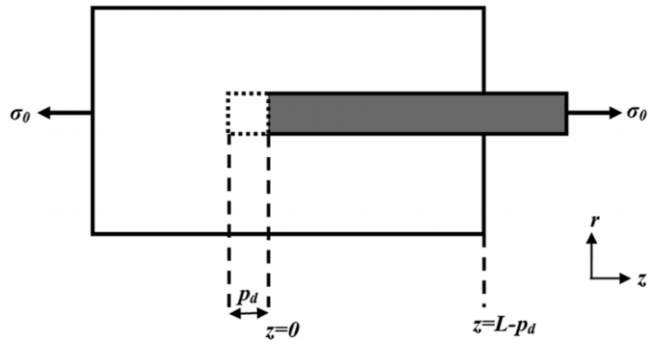

(c) Stage 3: completely debonded

Figure 2.22. The three stages of pull-out process (Aslani and Nejadi 2012).

2.9 Gap in knowledge

The findings from previous work on properties of various concretes were quite useful to understand the behaviour of UHPCs subject to high temperature, impact loading or the combination of them. Also, meso-scale modelling methods found in the literature help expand one's horizon in numerical studies of properties of SFRCs. Nevertheless, fire resistance of UHPCs remains a problem of concern, with UHPCs retaining less than 40% of their original strength after being exposed to high temperatures up to 1000 °C. UHPCs with higher fire resistance need to be developed and further studied. In the meantime, research on properties of UHPCs under a combination of temperatures and impact loading is very limited in the literature. Previous studies were either on UHPCs under high temperatures or under impact loading. Furthermore, there is little available information on differences between responses of UHPCs subject to the combined loading under elevated temperatures and after cooled down. Finally, meso-scale modelling needs to be extended to real 3D application that allows for random fibre distribution, small models cutting from SFRC blocks and appropriate links between fibre and concrete matrix, and other numerical simulations such as study on thermal properties of SFRCs.

CHAPTER 3

DEVELOPMENT OF UHPC WITH HIGH FIRE RESISTANCE

3 DEVELOPMENT OF UHPC WITH HIGH FIRE RESISTANCE

In this chapter, a total of six UHPC mixtures were designed and tested under different temperatures up to 1000 °C. The effects of aggregate type, fibre type and heating rate were investigated. Residual compressive strengths and stress-strain relationships were studied after the UHPC mixtures were exposed to elevated temperatures. Besides, attention was paid to explosive spalling since UHPCs are usually of compact structure and thus more vulnerable to explosive spalling than other concretes. It was found the mixture containing steel slag and hybrid fibre had excellent fire resistance. After being subjected to 1000 °C, this mixture retained a residual compressive strength of 112.8 MPa or a relative value of 69%.

3.1 Materials

The cement used in all mixtures in this study was ordinary Portland cement (42.5 Grade). The silica fume added to the mixtures had a bulk weight of $200\text{-}250\ \text{kg/m}^3$, a specific surface area of $20\text{-}28\ \text{m}^2/\text{g}$, and a particle diameter of $0.1\text{-}0.3\ \mu\text{m}$. Like silica fume, fly ash is a reactive material and has pozzolanic effect in the concrete mixture which helps convert free CH into calcium silicate hydrate (C-S-H) gel, so it was also applied to all specimens. The fly ash had a standard spherical shape, a density of $2.5\times10^3\ \text{kg/m}^3$, a stacking density of $0.7\times10^3\ \text{kg/m}^3$ and a thixotropic index of 8. Sieve analysis was conducted on the two types of fine aggregate, i.e. quartz sand and steel slag, as shown in Figure 3.1. The chemical compositions of cement, silica fume, fly ash and steel slag are listed in Table 3.1. The quartz sand has a density of $2.65\times10^3\ \text{kg/m}^3$, a hardness of 7 and a melting point of 1,650 °C. It needs to be noted no coarse aggregate was used in any specimens, which avoided expansion incompatibility between coarse aggregate and surrounding cement paste under elevated temperatures.

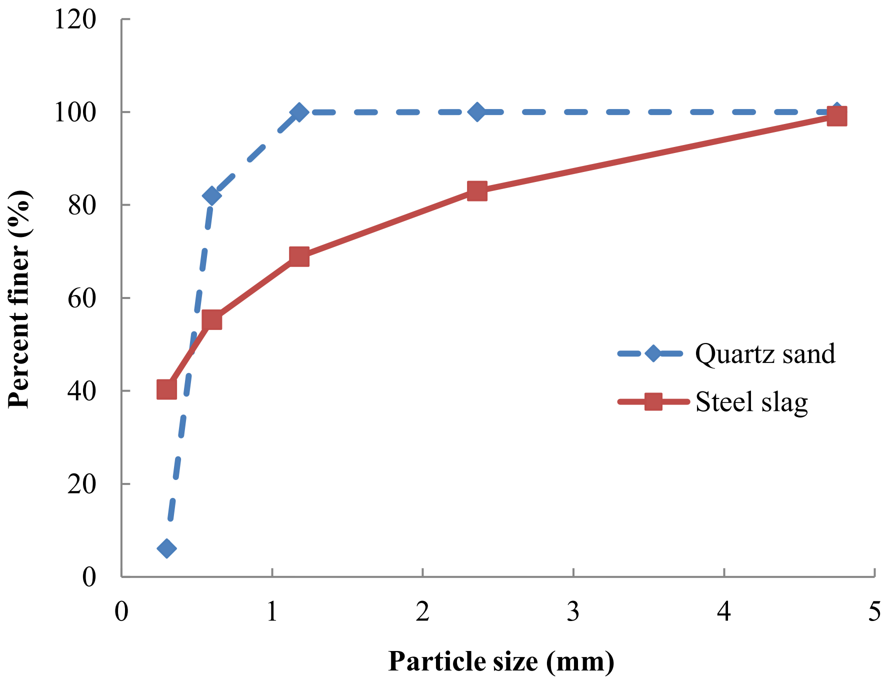

Figure 3.1. Sieve analysis of quartz sand and steel slag.

Table 3.1. Chemical compositions of cement, silica fume, fly ash and steel slag (%)

Materials	SiO_2	Al_2O_3	Fe_2O_3	CaO	MgO	Loss of ignition
Cement	21.86	4.25	2.66	63.59	2.19	1.75
Silica fume	93.95	0.5	0.59	1.95	0.27	1.3
Fly ash	52	22	4	12	0.62	<1
Steel slag	17.03	5.64	22.69	43.38	5.98	1.56

Two types of fibres, i.e. steel fibre and PP fibre, were either or both incorporated into the UHPC mixtures (see Figure 3.2). The steel fibre had a round straight shape and the properties of steel fibre and PP fibre are reported in Table 3.2.

(a) Steel fibre (b) PP fibre

Figure 3.2. Steel fibre and PP fibre.

Table 3.2. Properties of steel fibre and PP fibre

	Length (mm)	Diameter (mm)	Density (g/cm^3)	Modulus of elasticity (GPa)	Tensile strength (MPa)	Melting point (°C)
Steel fibre	10	0.12	7.8	-	> 2500	-
PP fibre	10	0.0031	0.91	≥ 3.5	≥ 400	165

3.2 Mixture proportioning

Totally six mixtures were prepared and they were divided into two series according to different fine aggregates, i.e. quartz sand or steel slag, with details shown in Table 3.3. The series 1 used quartz sand as fine aggregate, while the series 2 used steel slag. Mixtures in series 1 were divided into four categories according to fibre inclusion, i.e. no fibre, 2 vol.% steel fibre, 2 vol.% PP fibre or combination of 1 vol.% steel fibre and 2 vol.% PP fibre. Mixtures in series 2 were divided into two categories according to fibre inclusion, i.e. no fibre or combination of 1 vol.% steel fibre and 2 vol.% PP fibre. For designation of the six mixtures, the letter before the hyphen denotes the type of fine aggregates, i.e.

Q for quartz sand and S for steel slag, while the letter behind the hyphen means the type of fibres, i.e. 0 for no fibre, S for steel fibre, P for PP fibre and SP for hybrid fibre. Water to binder ratio was set at 0.16 and sand to binder ratio at 1.0 for all the mixtures. Unit weight for all the mixtures and slump for the mixtures Q-SP, S-0 and S-SP are listed in Table 3.4. The slump tests were conducted conforming to the Chinese standard GB/T 50080-2016 (equivalent to Australian standard AS 1012). It can be seen the slump of the Q-SP and S-SP concretes was greatly reduced by inclusion of the hybrid fibre.

Table 3.3. Mixture proportions of UHPCs (unit: kg/m^3)

Constituents	Series 1				Series 2	
	Q-0	Q-S	Q-P	Q-SP	S-0	S-SP
42.5 cement	850	850	850	850	850	850
Silica fume	137.5	137.5	137.5	137.5	137.5	137.5
Fly ash	112.5	112.5	112.5	112.5	112.5	112.5
Water	176	176	176	176	176	176
Superplasticizer	8	8	8	8	8	8
Quartz sand	1,100	1,100	1,100	1,100	-	-
Steel slag	-	-	-	-	1,100	1,100
Steel fibre	-	156	-	78	-	78
PP fibre	-	-	18.2	18.2	-	18.2

Table 3.4. Fresh state properties of UHPC mixtures

	Q-0	Q-S	Q-P	Q-SP	S-0	S-SP
Unit weight (kg/m^3)	2,450	2,610	2,250	2,460	2,590	2,700
Slump (mm)	-	-	-	70	295	75

3.3 Specimen preparation and tests

The compression tests were carried out for five target temperatures, i.e. 200, 400, 600, 800 and 1,000 °C. Under each target temperature, four specimens were prepared and tested allowing for randomness of explosive spalling. There were totally 144 specimens and all specimens had a cubic shape. A side length of 50 mm rather than larger was chosen for all the specimens in order to avoid too frequent occurrence of explosive spalling. To prepare the specimens, a forced mixer with 30 L capacity was used. Firstly, the fine aggregate was fed into the mixer and mixed with a small amount of water for two minutes. Then cement, silica fume and fly ash were added and mixed for five minutes before water and superplasticizer were poured. The mixing process continued for another eight minutes. Finally, fibres were added to the mixture and mixed for five more minutes before the mixture was cast in the steel moulds. 24 hours later, the specimens were demoulded and put into a water tank with thermostatic control, where they were submerged by hot water of constant 90 °C for one day in order to accelerate pozzolanic reaction. Then, they were cured under a standard curing condition for 28 days. Before heating, a drying treatment is usually needed to control explosive spalling. A mechanically ventilated oven was used to dry the paste and mortar specimens at 105 ± 1 °C for a duration of 5-6 days (Okpala 1989). However, after a comparative study of different drying temperatures and facilities (Gallé 2001), the author suggested 105 °C could be too high to prevent microstructure of the specimen from being impacted by oven drying treatment. In this study, the specimens were put into an electric furnace for a drying treatment under a temperature of 90 °C for 24 hours, which proved to be an effective means to control explosive spalling. Since all the six UHPC mixtures were prepared with the identical water content, i.e. 176 kg/m^3, and experienced the same procedure of curing and drying, it was supposed they had the similar initial moisture level. Specimens are shown in Table 3.5.

Table 3.5. Specimens

Q-0	Q-S	Q-P	Q-SP	S-0	S-SP
					

The specimens were heated in an electric furnace with a heating capability of 1400 °C. Real fire condition could be simulated as per the heating curve defined in the standards ISO 834 (ISO 1999) which has an exponential relationship between growing temperature and heating time. However, to make the heating process simple, some researchers (Khaliq and Kodur 2011) applied a constant heating rate of 5 °C/min according to the standards ASTM E831 (ASTM 2014). In this study, 4 °C/min was selected as the heating rate according to ASTM E831 (ASTM 2014) and 1 and 8 °C/min heating rates were chosen to make a comparison study in subsection 3.5.1. Compact concrete like UHPC is vulnerable to explosive spalling when being heated. To prevent damage to the furnace and ensure safety, silicon boards were mounted on the chamber inner walls of the furnace. Furthermore, a steel cage was presented inside the furnace to contain specimens being heated. At a time, four specimens were heated at a rate of 4 °C/min until reaching the target temperatures and then they remained subjected to the constant target temperatures for another period of time or called holding time to achieve uniformly distributed temperatures throughout the specimen. The holding time, according to (Chen et al. 2015), has a significant impact on stress-strain behaviour of concretes exposed to high temperatures. To determine an appropriate holding time, a heating simulation with target temperature 1000 °C was conducted using the thermal parameters from the European standard (Eurocode 2004). Figure 3.3 shows the temperature time-history in the furnace chamber and at the centre of the model. It can be seen after 2 hours of holding time (from 245 to 365 min), the temperature at the specimen centre is 999.3 °C, very close to the target temperature. For target temperatures lower than 1000 °C, the temperature gap between the furnace chamber and the centre of the model is smaller, as shown in Figure 3.3. Because concrete has higher thermal conductivity and lower specific heat under lower temperatures, it is no doubt the valid holding time for higher target temperature ensures uniform temperature distribution in case of lower target temperatures. Hence, in this study, the holding time for all specimens was consistently set at 2 hours to ensure uniformly distributed temperatures, at the same time to avoid impact of this factor. Afterwards, the furnace door was opened to let the specimens cool down to room temperature. It should be noted in this study temperatures were measured by the thermocouple mounted on the internal wall of the furnace unless specified otherwise.

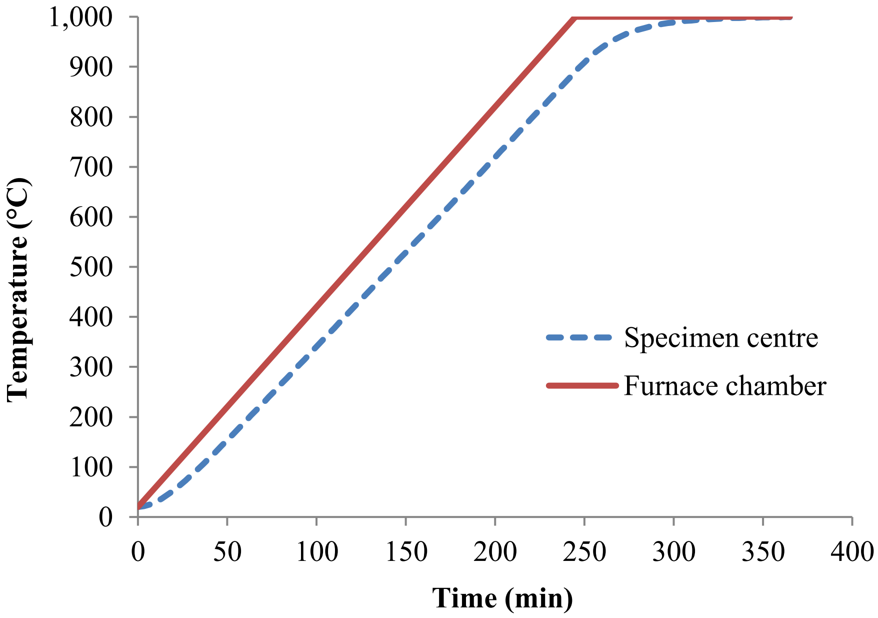

Figure 3.3. Comparison of temperature time-history between furnace chamber and specimen centre under target temperature 1000 °C.

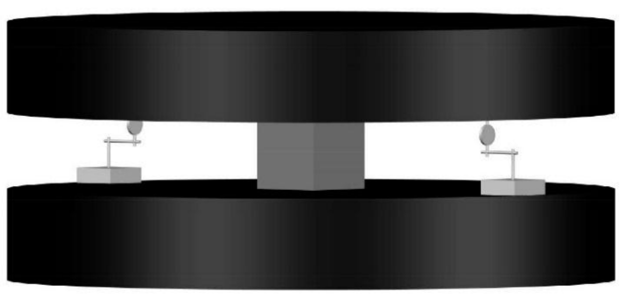

Figure 3.4. Sketch of testing setup.

Compressive tests were implemented on a 1,000 kN capacity electrohydraulic servo pressure testing machine, with the procedure conforming to the Chinese standard JGJ70-2009. The loading rate was controlled at 0.2 mm/min and the loading and displacement data were recorded automatically. To measure the displacement, two displacement gauges were symmetrically mounted on the two sides of the specimen between the loading plates, as illustrated in Figure 3.4. In this study, the compressive strength was calculated as the average value of four specimens.

3.4 Mass loss

In this study, mass loss refers to water evaporation and gas escape from UHPCs being heated. The relationship between mass loss and temperature for all the mixtures is depicted in Figure 3.5. It can be seen all mixtures had a small mass loss below 200 °C, indicating the UHPC specimens had a very compact structure which hindered vapour from escaping. For mixtures without PP fibres, i.e. the Q-0, Q-S and S-0 concretes, data were not recorded above 200 °C due to the severe explosion. Being heated to 200 °C, both the Q-0 and the Q-S specimens experienced an average mass loss of 1 g or 0.34% in percentage, indicating steel fibre had little influence in mass loss of UHPCs exposed to elevated temperatures below 200 °C. The mass loss of the other three mixtures containing PP fibres increased sharply between 200 °C and 400 °C. It was because the PP fibres melting at 165 °C provided a network of escaping channels for the vapour, while a majority of vapour came from the capillary water and bound water between 200 °C and 400 °C. Research (Tsuchiya and Sumi 1969) revealed within temperature range of 360 to 400 °C PP could be decomposed into various volatiles such as Pentane and Propylene, which was another contribution of the mass loss. Then with temperature growing from 400 °C to 1,000 °C, the mass loss rose slightly and peaked at around 8%. It can be seen from Figure 3.5 that the mass loss of the Q-P mixture was a little higher than the Q-SP and the S-SP mixtures. The reason could be the Q-P concrete did not contain steel fibres and thus suffered severer cracking and spalling, which boosted the escaping of vapour and smoke. Another possible reason could be the Q-P concrete as an exception might have more moisture or higher pore volume. The S-SP concrete suffered the smallest mass loss among the three mixtures containing PP fibres, indicating this mixture had more compact structure than the Q-SP concrete, which agreed with the fact that the latter had a lower probability of occurrence of explosive spalling than the former. From 800 °C to 1,000 °C, the mass loss of Q-SP and S-SP concretes decreased because they took in moisture from the air during a one-day cooling.

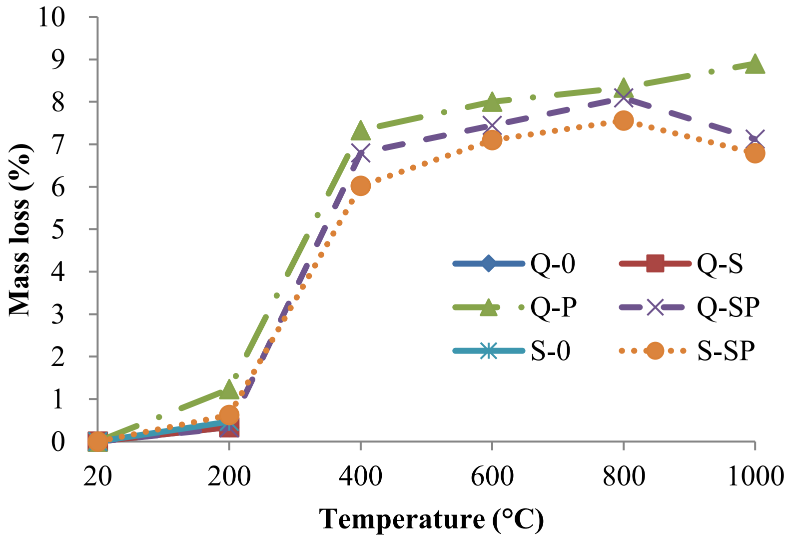

Figure 3.5. Mass loss under different temperatures.

3.5 Control of explosive spalling

3.5.1 Effect of heating rate on explosive spalling

To investigate the effect of heating rate on explosive spalling of heated UHPCs, three heating rates, i.e. 1, 4 and 8 °C/min, were applied to the Q-S concrete. The target temperature under 1 and 4 °C/min heating rates was set at 400 °C, while under 8 °C/min was set at 600 °C.

The spalling details of the Q-S concrete are reported in Table 3.6. It was observed under whatever heating rates all the specimens suffered serious explosive spalling, which suggested the heating rate had nothing to do with the probability of explosive spalling in the case of Q-S concrete that was very dense and without PP fibres. However, with the increase of heating rate, the explosive spalling started and ended earlier, both the spalling starting temperature and the spalling ending temperature became higher, and the smoke escaping temperature range became on a higher level. During the heating, there were several intense explosions happening under whatever heating rates, with big burst sounds being heard. Each intense explosion came with the escape of a large amount of vapour and dust, which could be observed outside the furnace. This phenomenon indicated that the accumulation of internal vapour pressure was a big contribution of the explosive spalling.

Table 3.6. Details of explosive spalling of Q-S concrete at different heating rates

Heating rate (°C/min)	1	4	8
Target temperature (°C)	400	400	600
Probability (%)	100	100	100
Starting time (min)[a]	325	92	35
Ending time (min)[a]	460	113	67
Starting temperature (°C)[b]	323	357	422
Ending temperature (°C)[b]	400	400	563
Smoke escaping temperature range (°C)[c]	350-391	369-400	460-553

[a] Starting time is the time when spalling was first observed, while ending time is the time after which spalling would no longer occur.

[b] Starting temperature is the temperature at which spalling was first observed, while ending temperature is the temperature above which spalling would no longer occur.

[c] Smoke escaping temperature is the temperature range only within which smoke was observed.

Table 3.7 shows the explosive spalling of the Q-S specimens heated under the three heating rates. It can be seen with higher heating rate and higher target temperature the debris of the specimens tended to be smaller, indicating more intense explosive spalling.

Table 3.7. Explosive spalling of Q-S concrete at different heating rates

Heating rate (°C/min)			
1			
4			
8			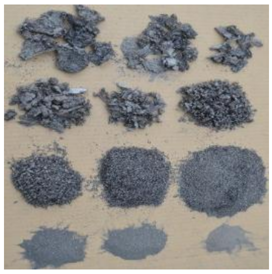

3.5.2 Explosive spalling of specimens without PP fibres

In this subsection, the explosive spalling of the mixtures without PP fibres, i.e. Q-0, Q-S and S-0, were compared under the identical target temperature of 400 °C and heating rate of 4 °C/min. The details of the explosive spalling are listed in Table 3.8 and Table 3.9 and the sieving results of debris are shown in Figure 3.6. All the mixtures suffered explosive spalling when being heated to the target temperature as shown in Table 3.8 and broke into pieces as shown in Table 3.9. Accompanying each explosive spalling, it was observed that some vapour was intensively released. This phenomenon indicated the built-up vapour pressure was an important contribution to the explosive spalling.

Compared with the Q-0 concrete without any fibres, the Q-S concrete reinforced with 2 vol.% steel fibres started exploding at a higher temperature. It was because explosive spalling would not happen until the internal vapour pressure was greater than the tensile strength of the concrete which was considerably increased by the addition of steel fibre. The S-0 concrete which had steel slag as fine aggregate had almost the same spalling starting time but higher starting temperature in comparison with the Q-0 and Q-S concretes which had quartz sand as fine aggregate.

Table 3.8. Details of explosive spalling of mixtures without PP fibres at heating rate of 4 °C/min

Mixture	Q-0	Q-S	S-0
Target temperature (°C)	400	400	400
Probability (%)	100	100	100
Starting time (min)[a]	86	92	92
Ending time (min)[a]	109	113	147
Starting temperature (°C)[b]	338	357	385
Ending temperature (°C)[b]	400	400	400

[a,b] Same as in Table 3.6.

Figure 3.6 exhibits sieving results of debris of the three mixtures without PP fibres, which reflects effect of steel fibre and difference between the two types of aggregate on explosive spalling. Among the three mixtures, the Q-S concrete had the greatest proportion in both large and small debris sizes as shown in Figure 3.6. The steel fibres bridged the gaps when the cracks were growing and thus restrained propagation of the cracks, which helped the Q-S concrete remain more large-size debris than the other two without steel fibres. On the other hand, the constraint effect of the steel fibres caused greater vapour pressure, which resulted in more small-size debris after the specimens exploded. Compared to the Q-0 concrete, the S-0 concrete containing steel slag had a higher percentage of debris with sizes over 4.5 mm. The reason could be the steel slag produced under 1,650 °C had relatively high thermal stability and similar chemical compositions to the cement, which reduced thermal incompatibility between the fine aggregate and the cement paste.

Table 3.9. Explosive spalling of mixtures without PP fibres at heating rate of 4 °C/min

Mixture			
Q-0			
Q-S			
S-0			

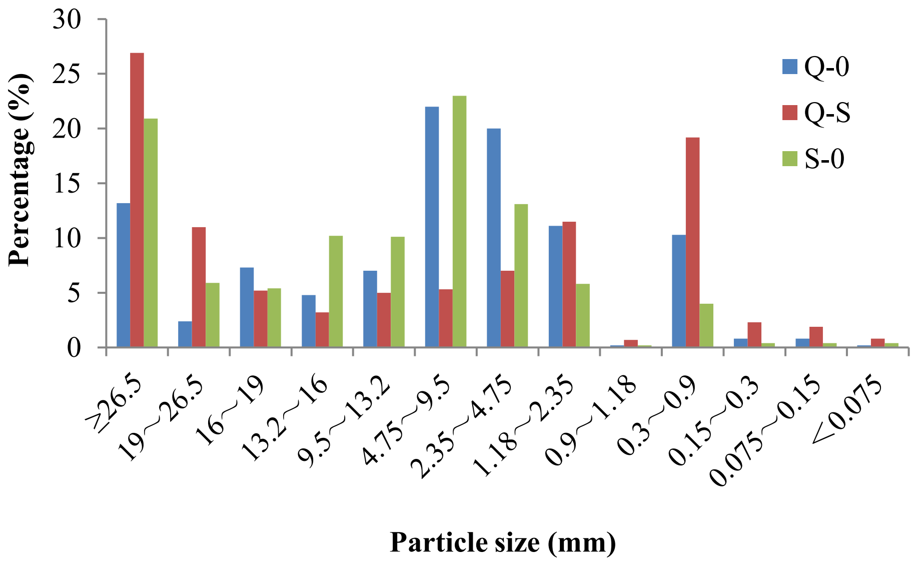

Figure 3.6. Sieving results of debris of mixtures without PP fibres.

3.5.3 Explosive spalling of specimens with PP fibres

Table 3.10. Details of explosive spalling of mixtures with PP fibres under different target temperatures

Target temperature (°C)	Spalling probability (%)			Spalling temperature range (°C)		
	Q-P	Q-SP	S-SP	Q-P	Q-SP	S-SP
200	0	0	0	-	-	-
400	0	0	50	-	-	392-400 [a]
600	75	50	50	404-458	447-464 [a]	467-503 [a]
800	75	0	50	409-472	-	391-440 [a]
1,000	100	50	25	413-463	437-457 [a]	464 [a]

[a] Only slight spalling was observed.

As discussed above, PP fibre, which melts at about 165 °C, helps release vapour pressure and thus reduces the risk of explosive spalling when concrete is exposed to elevated temperatures. In this subsection, three mixtures containing PP fibres, i.e., the Q-P, Q-SP and S-SP concretes, are compared in terms of explosive spalling. The three concretes were heated to five target temperatures, i.e. 200, 400, 600, 800 and 1,000 °C, with explosive spalling details reported in Table 3.10. Spalling damage of these specimens is displayed in Table 3.11, where unheated specimens are also listed in order to make a comparison.

Table 3.11. Explosive spalling of mixtures with PP fibres under different temperatures

Tempera-ture (°C)	Q-P	Q-SP	S-SP
20			
200			
400			
600			
800			
1,000			

From Table 3.10 and Table 3.11, it can be seen all the specimens did not experience explosive spalling at the target temperature of 200 °C. Under the 400 °C target temperature, half of the four S-SP specimens suffered slight spalling but the other two remained intact. With target temperature over 600 °C, all the specimens experienced spalling to some degree, which occurred between 391 °C and 503 °C. However, unlike in the tests of the mixtures without PP fibres, no intensive release of vapour was observed coming with any of the spalling. The spalling could result from thermal stress and incompatibility between the aggregate and the cement paste but not vapour pressure. It can also be seen from Table 3.10 and Table 3.11 that the Q-P concrete which had only PP fibres suffered more frequent and severer spalling than the other two reinforced with hybrid fibres. Steel fibre failed to prevent the occurrence of explosion resulting from built-up vapour pressure as discussed in subsection 3.5.2, but it reduced probability and intensity of spalling resulting from thermal stress and incompatibility between the aggregate and the cement paste. When being heated from 20 °C to 1,000 °C, all the specimens experienced a colour change from grey to grey-white and then amber, as shown in Table 3.11.

3.6 Quasi-static compression tests

Results for all mixtures are reported in Table 3.12, where f_c denotes compressive strength of the specimens which were not exposed to high temperatures (i.e. control specimens), f_{cT} denotes compressive strength of the specimens which were exposed to high temperatures and f_{cT} / f_c means normalised compressive strength. It should be noted while most of the test results were an average of four specimens, some came from three due to explosive spalling. Due to severe explosion, data for the mixtures Q-0, Q-S and S-0 were not recorded above 200 °C.

3.6.1 Specimens without PP fibres

Because of severe explosive spalling when being heated to 400 °C and above, the specimens without PP fibres were tested only at room temperature and 200 °C. For the compressive tests, failure forms of the three mixtures, i.e. Q-0, Q-S and S-0, are displayed in Table 3.13. Without addition of any fibres, both the Q-0 and S-0 concretes suffered brittle damage and were crushed up under either temperature. By contrast, the Q-S concrete reinforced with steel fibres improved a lot in ductility and remained its integrity under the compressive loading. The UHPC mixtures had highly compact structure, leading to reduced relative stiffness to the steel loading plate. The internal energy of the loading plate building up during the loading procedure was released suddenly when the specimen yielded, which resulted in the crush of the specimens without steel fibres due to inadequate tensile strength.

Table 3.12. Compressive strength under various temperatures

Temperature (°C)		Q-0	Q-S	Q-P	Q-SP	S-0	S-SP
20	f_c (MPa)	112.4	187.5	125.5	162.1	90.0	162.8
200	f_{cT} (MPa)	164.7	204.8	132.5	176.2	191.0	182.5
	f_{cT}/f_c	1.47	1.09	1.06	1.09	2.12	1.12
400	f_{cT} (MPa)	-	-	163.5	230.1	-	215.9
	f_{cT}/f_c	-	-	1.30	1.42	-	1.33
600	f_{cT} (MPa)	-	-	112.3	153.8	-	208.3
	f_{cT}/f_c	-	-	0.89	0.95	-	1.28
800	f_{cT} (MPa)	-	-	38.1	40.0	-	147.6
	f_{cT}/f_c	-	-	0.30	0.25	-	0.91
1,000	f_{cT} (MPa)	-	-	37.5	40.4	-	112.8
	f_{cT}/f_c	-	-	0.30	0.25	-	0.69

Table 3.13. Failure forms of mixtures with PP fibres under different temperatures

Tempera-ture (°C)	Q-0	Q-S	S-0
20			
200			

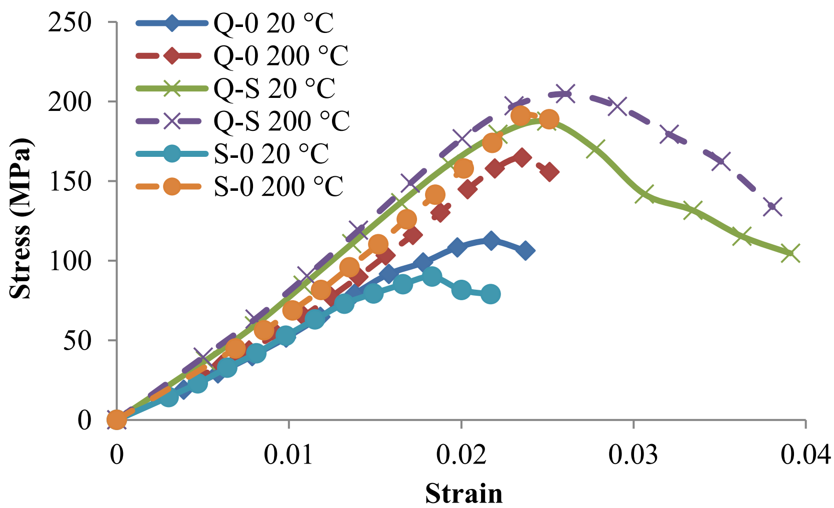

Figure 3.7. Stress versus strain curves.

Stress-strain curves for the three mixtures under room temperature and 200 °C are shown in Figure 3.7. It can be seen that at 200 °C all the three mixtures enjoyed an improvement of compressive strength in comparison with that at room temperature. The reason could be that high-pressure moisture failing to escape due to the tight structure of the UHPC specimen created an enclosed high-temperature and high-pressure curing environment or "internal autoclaving" (Rashad et al. 2012). This curing environment greatly boosted both cement hydration and pozzolanic reactions due to the presence of active SiO_2 from silica fume and fly ash, generating more C-S-H gel. There the C-S-H gel was transformed into xonotlite and tobermorite, which made the internal structure of the specimen even more compact and thus enhanced its compressive strength. As shown in Table 3.12, when being heated to 200 °C the Q-0 concrete had a 47% increase of compressive strength, while it was only 6% for the Q-P concrete in comparison with their respective original room-temperature strength. It was because PP fibre enhanced the room-temperature strength of the Q-P concrete but its melting at 165 °C made this enhancement invalid. On the other hand, the melting of PP fibres left pores in the concrete, which resulted in more cracks when the concrete was under pressure and reduced moisture pressure due to the release of vapour. These weakened the boost effect resulting from the high-temperature and high-pressure curing environment. From Table 3.12, it can also be seen the Q-S concrete had an unimpressive 9% improvement of compressive strength compared to 47% for the Q-0 concrete and 112% for the S-0 concrete when exposed to 200 °C. The reason is the Q-S concrete reinforced with steel fibres had comparatively high compressive strength at room temperature. Figure 3.7 also shows the Q-S concrete had much higher ductility and toughness than the other concretes under either temperature.

3.6.2 Specimens with PP fibres

Table 3.14 shows the failure forms of the three mixtures containing PP fibres exposed to temperatures ranging from 20 °C to 1,000 °C. As can be seen, the Q-P concrete suffered a ductile damage at room temperature, but under temperatures 200, 400 and 600 °C its damage was in a brittle manner. It was because the PP fibres improved the ductility of the Q-P concrete under room temperature. However, when it was heated to 200 °C and above, the melted PP fibres resulted in deterioration of ductility of the concrete. Under 800 °C and 1,000 °C, the Q-P concrete exhibited a ductile failure mode again. This was because the concrete had been loosened and softened. Rashad et al. (Rashad et al. 2012) pointed out coarsening of pore-structure can happen when cement paste is heated to 400 °C and above and C-S-H can be dramatically decomposed at 600 °C and above, which may lead to concrete loosening and softening and cohesiveness deterioration of cement paste. Due to the cohesiveness deterioration of the cement paste, a double pyramid was formed during the compressive test on the Q-P concrete subjected to 800 °C and 1,000 °C, as shown in Table 3.14. Compared to the Q-P concrete, the Q-SP and S-SP concretes experienced ductile damage forms under compression throughout all the target temperatures from 20 °C to 1,000 °C. Not only did the addition of hybrid fibres restrain occurrence of severe explosive spalling, but also it greatly improved the ductility of the concrete exposed to high temperatures. Under 1,000 °C, however, the Q-SP and S-SP concretes had the similar failure form to the Q-P concrete. This could be attributed to the loss of strength of steel fibres under high temperatures. According to (Eurocode 2005), under 800 °C and 1,000 °C steel retains only 11% and 4% of its yield strength respectively.

The relationships between compressive strength and temperature for the three concretes are illustrated in Figure 3.8. With the target temperature ascending from 20 °C to 400 °C, all the three concretes made an improvement in compressive strength. From room temperature to 200 °C, the enhancement mechanism is the same as discussed in subsection 3.6.1. From 200 °C to 400 °C, more C-S-H gel was produced and transformed into xonotlite and tobermorite as pozzolanic reactions continued under the high-temperature and high-pressure environment. In addition, evaporation of bound water made the cement paste more compact and harder. Also, during this stage, PP fibres melted completely, greatly relieving vapour pressure. All these contributed to an enhancement of compressive strength of the three concretes.

In contrast, from 400 °C to 800 °C all the three concretes suffered a strength decrease. It can be seen from Figure 3.8, the strength loss of the Q-SP concrete was a little steeper than that of the Q-P concrete, while the S-SP concrete had a much slower deterioration of strength than the other two. During this stage, decomposition of the CH occurred between approximately 430 °C and 600 °C, while for the C-S-H it started at around 560 °C and then became significant above 600 °C (Rashad et al. 2012). A large amount of C-S-H was transformed into C_3S and β-C_2S and α-SiO_2 was transformed into β-SiO_2, which resulted in increased porosity in the paste (Li et al. 2012). At 800 °C, the C-S-H was completely decomposed and the $CaCO_3$ started to decompose, contributing to decreased compactness of the internal structure and a lot of small cracks on the surfaces of the specimen. Also, at this stage, the mismatching volume expansion between the cement paste and the aggregate played a significant role that worsened the mechanical performance of the concrete (Ducman and Mladenovič 2011; Netinger et al. 2013).

Table 3.14. Compressive failure forms of mixtures with PP fibres under different temperatures

Tempera-ture (°C)	Q-P	Q-SP	S-SP
20			
200			
400			
600			
800			
1,000			

From 800 °C to 1,000 °C, the strength of the Q-P and Q-SP concretes remained almost the same but that of the S-SP concrete kept falling. However, the S-SP concrete retained a relatively high residual strength of 112.8 MPa or normalised residual strength of 69% after being exposed to 1,000 °C, while that for the Q-P and Q-SP concretes was only 40 MPa or below 30%.

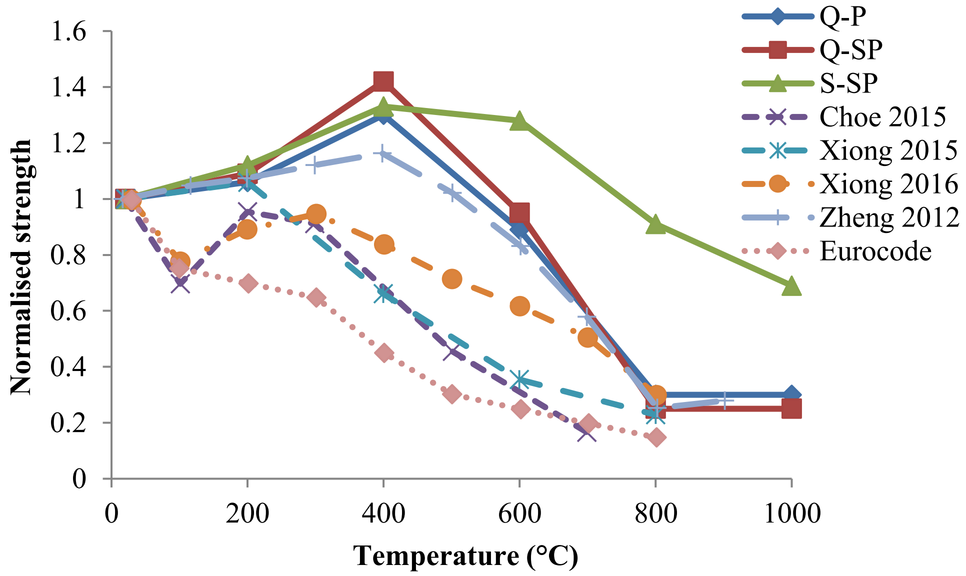

Figure 3.8. Normalised compressive strength versus temperature.

Figure 3.8 also shows the results of UHPCs from other researches (Choe et al. 2015; Xiong and Liew 2016; Xiong and Liew 2015; Zheng et al. 2012) and high strength concrete according to the European standard EN 1992-1-2 (Eurocode 2004). It can be seen over 600 °C the S-SP concrete retained markedly higher normalised strength than the other concretes. The main reason could be, on one hand, adding steel slag to the mixture reduced the amount of CH formed during the hydration, which increased the fire resistance of the mixture exposed to elevated temperatures (Khoury et al. 1985; Mendes et al. 2007). On the other hand, steel slag usually has rough surfaces and thus improves properties of interfacial transition zone (ITZ), which could be critical for concrete under high temperatures. Research conducted by (Jia 2011) revealed NSC exposed to high temperatures above 300 °C exhibited different damage modes under compressive loading. The damage occurred along the ITZ or within the paste other than running through the aggregate which was the case for unheated concretes, indicating high temperature could severely degrade properties of ITZ. It was suggested a major factor contributing to strength loss of concrete using steel slag as aggregate is the expansion of steel slag in contrast to the shrinkage of cement paste after exposed to high temperatures (Ducman and Mladenovič 2011; Netinger et al. 2013). However, in this study steel slag was used as fine aggregate and most of it had a size smaller than 2.5 mm, which could mitigate the negative effect of volume mismatching between the steel slag and the cement paste.

Besides, as discussed in subsection 3.5, steel slag had excellent thermal stability and similar chemical compositions to cement, which reduced thermal incompatibility between the fine aggregate and the cement paste and could improve residual properties. From Figure 3.8, it can also be seen the S-SP concrete was the only one that had its strength under 600 °C higher than its room-temperature strength.

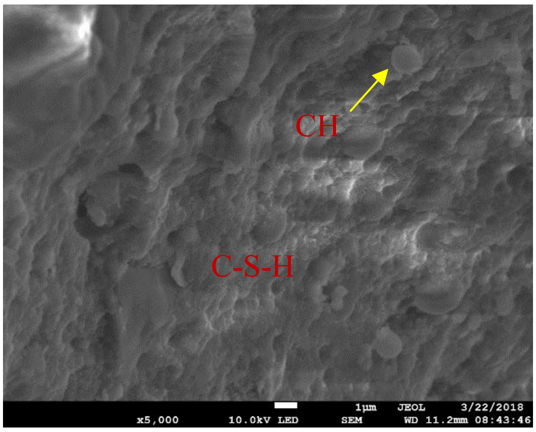

(a) 20 °C

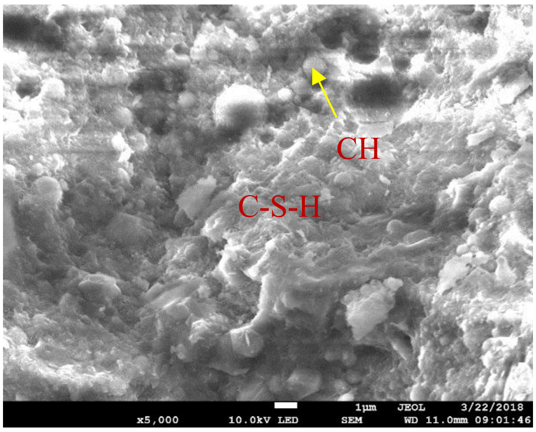

(b) 200 °C

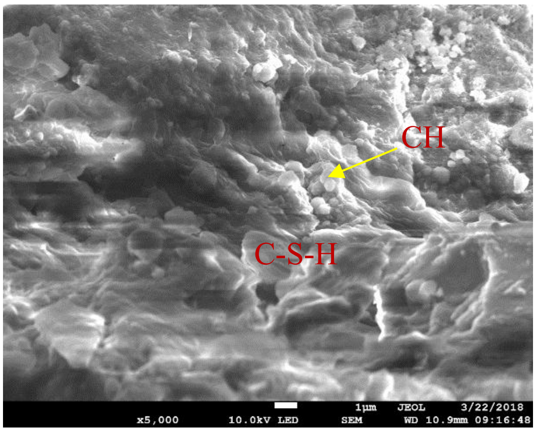

(c) 400 °C

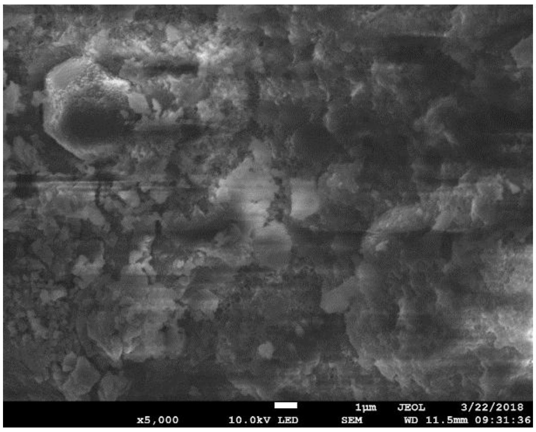

(d) 600 °C

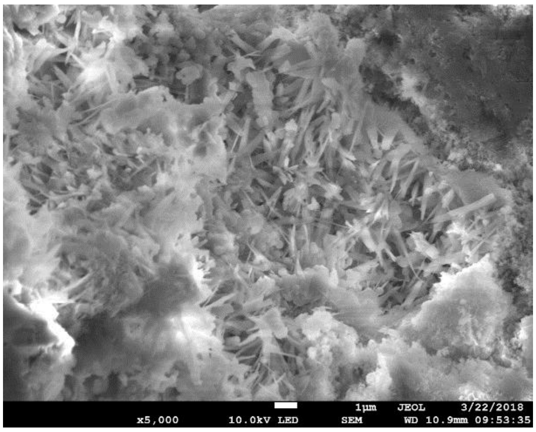

(e) 800 °C

Figure 3.9. SEM analysis of S-SP concrete after exposure to different temperatures.

Figure 3.9 shows the SEM analysis of the S-SP concrete after exposure to temperatures from 20 °C to 800 °C, using a JEOL JSM-7800F SEM. For the S-SP specimen never subjected to an elevated temperature, it had continuous and compact C-S-H phase and scattered CH crystals. After exposed to 200 °C, the C-S-H phase in the concrete remained continuous and became more compact while the CH crystals became fewer and smaller. However, due to melting of PP fibre and cracking resulting from vapour pressure, the matrix presented a rougher surface. After subjected to 400 °C, the C-S-H phase had even more compact structure and better integrity while the CH phase continued to reduce in quantity and size. Suffering 600 °C, the C-S-H phase lost some continuity and integrity due to decomposition and became less compact. At the same time, the CH phase completely decomposed. At 800 °C, the C-S-H phase did not exist any longer and the matrix was honeycombed, resulting in greatly worsened concrete performance.

The stress-strain curves of the three concretes under different temperatures from 20 °C to 1,000 °C are depicted in Figure 3.10, Figure 3.11 and Figure 3.12, respectively. It can be seen the stress-strain curves of the Q-P and the Q-SP concretes had the similar varying pattern under different temperatures. For example, both the concretes suffered a significant drop in strength and modulus elasticity when being heated to 600 °C and above and had a flattened stress-strain curve under 800 °C and 1,000 °C. As discussed above, the concretes were loosened and softened when being heated to higher than 800 °C.

Nevertheless, due to the addition of steel fibres, the Q-SP concrete exhibited greater ductility and toughness than the Q-P concrete under whatever temperatures. From Figure 3.12 it can be seen even under 600 °C the S-SP concrete had strength much higher than its room-temperature strength and relatively high modulus elasticity. Under higher temperatures up to 1,000 °C, the S-SP concrete retained relatively high residual strength and modulus elasticity in comparison with the Q-P and the Q-SP concretes.

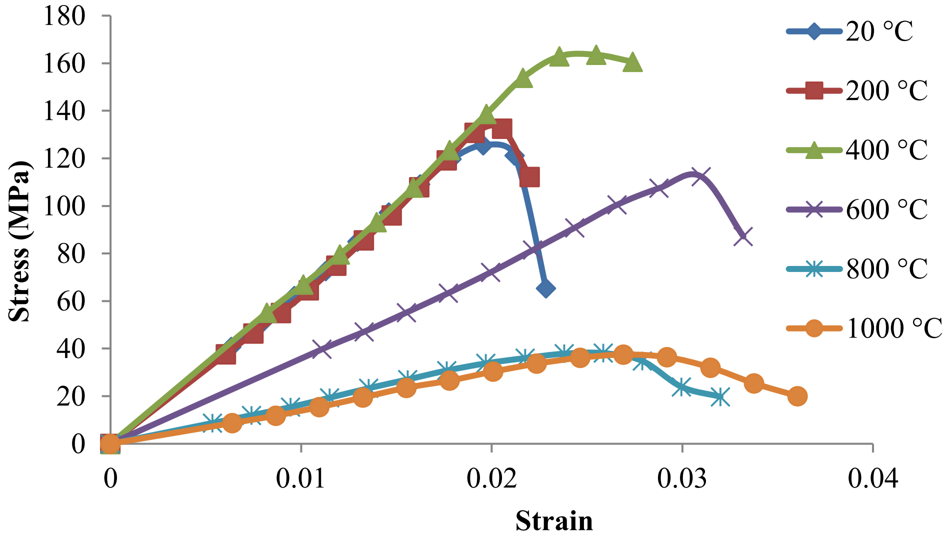

Figure 3.10. Stress versus strain curves of Q-P concrete.

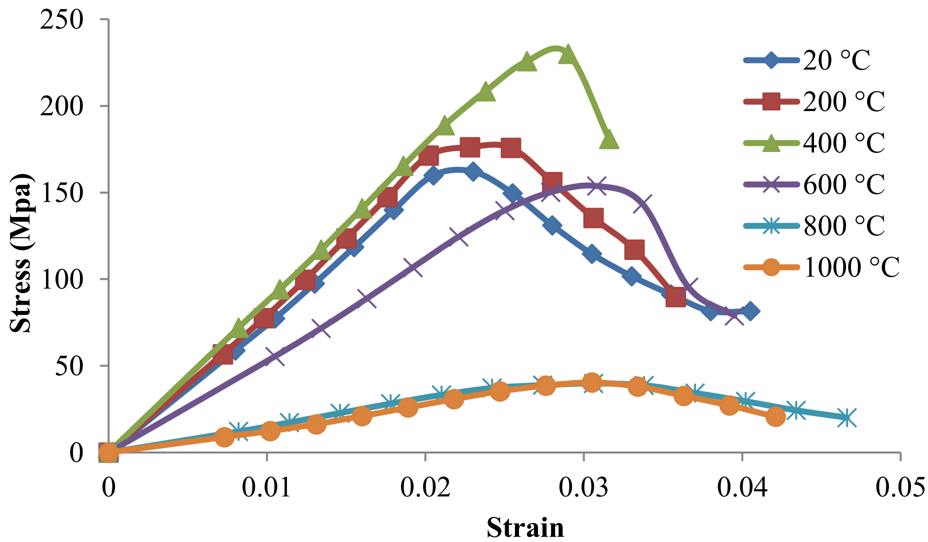

Figure 3.11. Stress versus strain curves of Q-SP concrete.

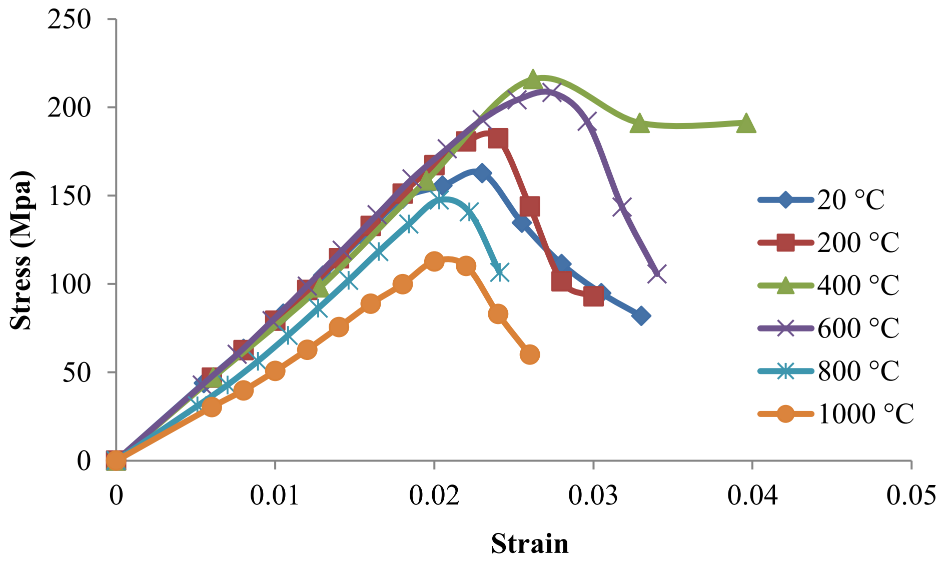

Figure 3.12. Stress versus strain curves of S-SP concrete.

Figure 3.13 shows relationships between normalised modulus of elasticity and temperature of the three UHPC mixtures as well as light weight concrete from the European standard EN 1992-1-2 (Eurocode 2004). It should be noted modulus of elasticity here was calculated as the slope between two points on the ascending portion of stress-strain curves corresponding to 60% and 40% of peak stress respectively, which was also adopted by (Su et al. 2014). The curves for the three UHPCs in Figure 3.13 has a similar pattern to those in Figure 3.8, though increase of modulus of elasticity was much less impressive than that of strength from 20 °C to 600 °C. It can also be seen the degradation of modulus of elasticity of concrete specified in the European standard EN 1992-1-2 (Eurocode 2004) is much severer than the three UHPCs under whatever elevated temperatures.

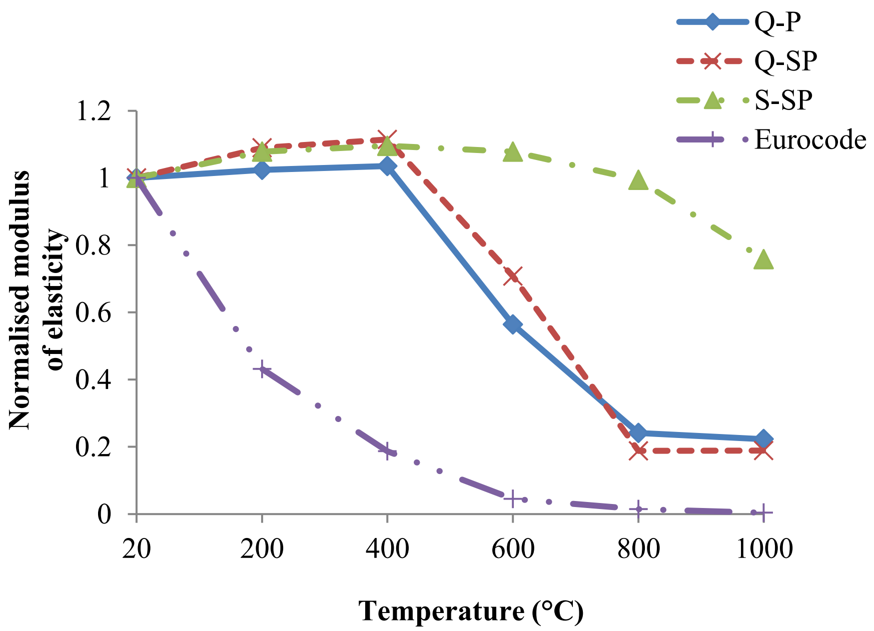

Figure 3.13. Normalised modulus of elasticity versus temperature.

3.7 Summary

To develop a UHPC with excellent fire resistance, a total of six UHPC mixtures were designed using quartz sand or steel slag as fine aggregate, with or without steel fibre, PP fibre or hybrid fibre. Special attention was paid to explosive spalling of UHPCs subjected to elevated temperatures since UHPCs are usually of compact structure and thus vulnerable to explosive spalling. Besides, residual compressive strengths and stress-strain relationships of the UHPC mixtures are discussed after they were heated to elevated temperatures up to 1,000 °C. The following conclusions could be drawn from the test results and the above analysis:

1) Most mass loss of the mixtures with PP fibre happened between 200 °C and 400 °C due to water evaporation and PP volatilisation.
2) Heating rate had little effect on explosive spalling occurrence of the Q-S mixture, which had very dense matrix without PP fibres. However, higher heating rate could result in more intense explosive spalling.
3) Vapour pressure was a significant contribution to explosive spalling. PP fibre was an effective additive to control explosive spalling, though failed to eliminate it completely. Steel fibre could reduce the probability and intensity of spalling resulting from thermal

stress and incompatibility between aggregate and cement paste.

4) A UHPC mixture with excellent fire-resistance properties was successfully developed. After being exposed to 1,000 °C, it retained 69% of its original compressive strength, much higher than the existing concretes. Reinforced with hybrid fibre, this concrete also greatly decreased the occurrence of explosive spalling.
5) Addition of steel slag to UHPC mixtures reduced amount of CH formed during hydration. With rough surface, steel slag could improve ITZ properties of UHPCs exposed to elevated temperatures. Having high thermal stability and similar chemical compositions to cement, steel slag as fine aggregate also relieved thermal incompatibility between aggregate and cement paste. These features of steel slag may significantly improve residual properties of UHPCs using steel slag as fine aggregate.

CHAPTER 4

COMPRESSIVE STRENGTH OF UHPC SUBJECTED TO COMBINED EFFECT OF ELEVATED TEMPERATURE AND IMPACT LOADING

4 COMPRESSIVE STRENGTH OF UHPC SUBJECTED TO COMBINED EFFECT OF ELEVATED TEMPERATURE AND IMPACT LOADING

In this chapter, the UHPC is a newly developed one with excellent fire resistance as described in Chapter 3 and denoted as S-SP mixture there. This UHPC is reinforced with hybrid fibre, i.e. PP fibre and steel fibre, and uses steel slag as fine aggregate. Quasi-static compression tests showed after exposed to 1,000 °C this UHPC retained 69% of its original room-temperature compressive strength. Reinforced with hybrid fibre, this concrete greatly decreased the occurrence of explosive spalling. Here, to reveal its response to simultaneous impact loading and high temperature, dynamic tests were carried out after the specimen was heated up to 800 °C. A self-designed Split Hopkinson Pressure Bar (SHPB) system with heating facility was applied to the tests. Comparison was made between SHPB tests under elevated temperatures and after cooled down.

4.1 Experimental details

4.1.1 Specimen preparation

Figure 4.1. Specimens for SHPB tests.

In the SHPB tests, three cylindrical specimens in size of $\Phi 50\times 25$ mm were used for each case. Cylindrical specimens were sliced from cylinders in size of $\Phi 50\times 100$ mm, which were drilled out of blocks in size of $100\times 100\times 400$ mm. Then the two end planes of each cylindrical specimen were ground even and parallel to each other with a tolerance of 0.02 mm. Specimens are shown in Figure 4.1. Owing to difference between diameters of specimens and pressure bars, to align axes of specimens with that of pressure bars a cushion made of pot clay was used for each test, as shown in Figure 4.2. These cushions, with a depth less than that of the specimens, had high fire resistance but very low compressive strength.

Figure 4.2. Pot clay cushions.

4.1.2 Experimental setup and methodology

The SHPB setup is shown in Figure 4.3. The system consisted of 75-mm-diameter pressure bars made of steel and an in-site explosion-protection electric furnace seated between the incident bar and the transmission bar. Figure 4.4 displays the details of the electric furnace, which is mainly made up of tubular heating chamber, explosion-protection layer, furnace flue and thermal insulating layer. There are holes on the explosion-protection layer so that heat is able to be passed onto the heating chamber. These holes are small enough to protect the furnace flue from being damaged by specimen explosion. To start the test, a specimen is placed in the centre of the heating chamber and then the two chamber doors are closed. During heating, temperature is monitored by using a thermocouple inserted into the heating chamber through the observation hole. Once the target temperature is achieved throughout the specimen, the two chamber doors are lifted and pressure bars are quickly positioned, followed by an immediate launch of the striker bar. The use of the in-site explosion-protection electric furnace contributes to little temperature drop of the heated specimen.

Figure 4.3. SHPB setup.

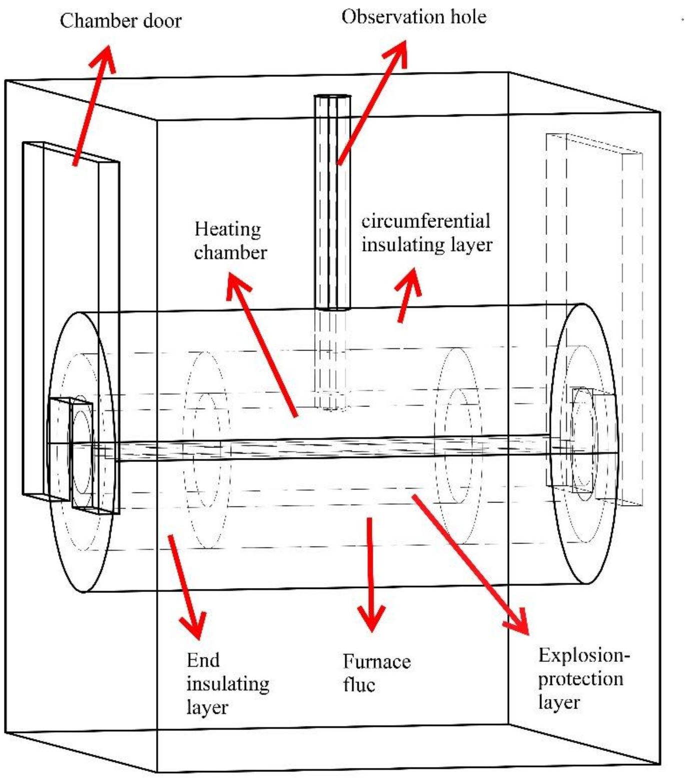

Figure 4.4. Schematic diagram of electric furnace.

It was known that the UHPC was sensitive to heating rate in terms of explosive spalling. To make the heating process more efficient but at the same time avoid explosive spalling, preliminary heating tests (as shown in Figure 4.5) were implemented under each target temperature, i.e. 200, 400, 600, 800 °C. Besides, after target temperature in the heating chamber was reached, a hold time needed to be obtained in order to achieve even temperature distribution within the specimen, which was assumed true when the temperature of the specimen centre reached the target temperature. Thereby, a minimum total heating time was determined for each of the target temperatures as 45, 65, 100, 145 minutes respectively, as shown in Figure 4.6. The results of quasi-static compression tests and SHPB tests are listed in Table 4.1.

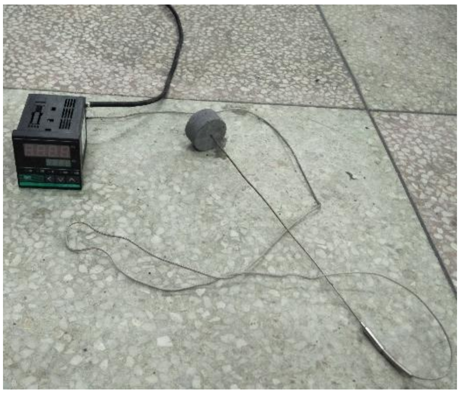

(a) Specimen with thermocouple installed

(b) Test setup

Figure 4.5. Heating test.

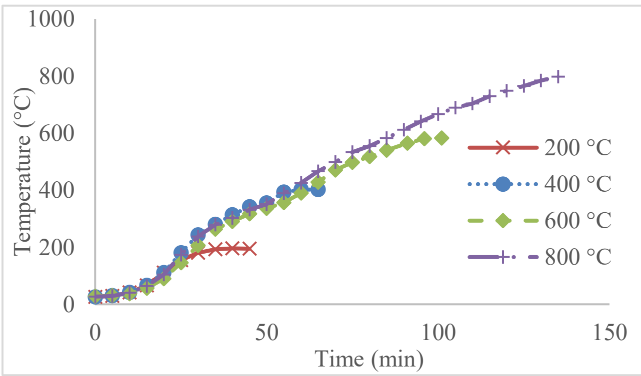

Figure 4.6. Temperature time-history curves of specimen centre under different target temperatures.

Table 4.1. Test results

Tempera-ture (°C)	Static strength (MPa)	Gas pressure[a] (MPa)	Projectile velocity (m/s)	Strain rate (s^{-1})	Dynamic strength (MPa)	Modulus of elasticity[b] (GPa)
20	162.8	0.25	7.3	98.1	198.3	22.7
		0.30	8.9	147.0	228.7	23.3
		0.35	10.2	206.0	231.7	20.4
		0.40	11.2	258.0	260.0	27.8
		0.45	12.3	308.3	264.3	27.8
200	182.5	0.25	7.2	140.0	173.5	17.2
		0.30	8.9	213.7	167.0	13.3
		0.35	10.1	267.0	180.3	12.7
		0.40	11.1	300.3	196.0	12.2
		0.45	12.3	375.0	198.0	11.5
400	215.9	0.25	7.2	112.0	224.5	25.0
		0.30	8.7	164.3	238.0	19.6
		0.35	10.1	203.3	241.0	15.4
		0.40	11.1	249.0	250.5	17.2
		0.45	12.2	282.3	287.3	20.0
600	208.3	0.25	7.1	112.0	234.3	22.2
		0.30	8.7	135.7	259.0	17.5
		0.35	10.2	192.5	266.5	16.9
		0.40	11.2	231.0	254.0	16.9
		0.45	12.2	245.5	295.0	17.5
800	147.6	0.25	7.3	151.7	163.3	10.3
		0.30	8.7	192.7	169.0	12.8
		0.35	10.0	243.3	180.0	8.5
		0.40	11.2	292.0	194.3	9.8
		0.45	12.1	347.0	158.3	7.6

Note:

[a] Gas pressure in the gas cannon controls projectile velocity of the striker bar.

[b] Modulus of elasticity is calculated as slope between two points on ascending portion of stress-strain curves, corresponding to 60% and 40% of peak stress respectively.

4.2 Results and discussion

4.2.1 Explosive spalling and colour changes

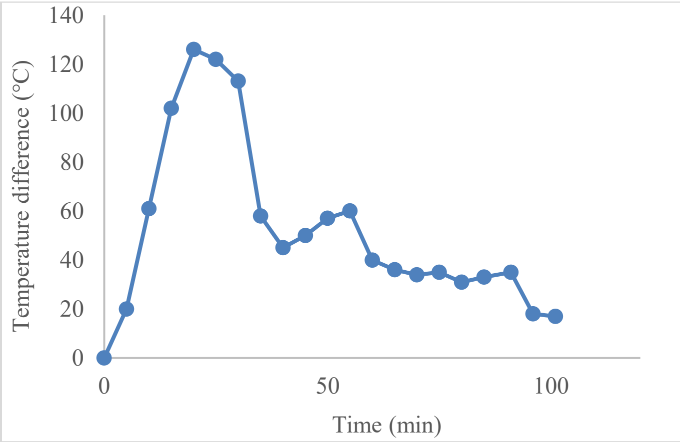

Figure 4.7. Time history of temperature difference between chamber and specimen centre

The preliminary heating tests revealed the UHPC specimen was heating rate dependent in terms of explosive spalling and most spalling occurred when temperature of the heating chamber was between 320 and 380 °C (Hereinafter, temperatures were measured in the heating chamber if not specified). PP fibres melting at around 160 °C helps release vapour and thus reduce vapour pressure in concrete. However, the melting of PP fibres was far from even because of temperature gradient throughout the specimen during the heating process. Figure 4.7 shows the temperature difference between the heating chamber and the specimen centre varied with heating time under target temperature of 600 °C. It can be seen the difference went up to 126 °C at 20 minute and then decreased to 17 °C at 100 minute. This also led to temperature gradient and thus thermal stress within the specimen. Research conducted by Tsuchiya and Sumi (Tsuchiya and Sumi 1969) revealed between temperature range of 360 to 400 °C PP could be decomposed into various volatiles such as Pentane and Propylene, which could aggravate internal vapour pressure. In the tests, obvious smoke was observed across the temperature range of 280 to 480 °C. Since release of vapour was slow due to compactness of the UHPC, too great heating rate was likely to give rise to explosive spalling between 320 and 380 °C. Therefore, from 300 to 500 °C the heating rate was set at 5 °C/min, which was smaller than under other temperatures. Nevertheless, there was still a 10% spalling chance, all happening in the temperature range of 320 to 380 °C. Figure 4.8 shows the debris of a specimen suffering explosive spalling at 370 °C and the broken cushion due to impact from the explosive spalling.

Figure 4.8. Debris of specimen suffering explosive spalling at 370 °C.

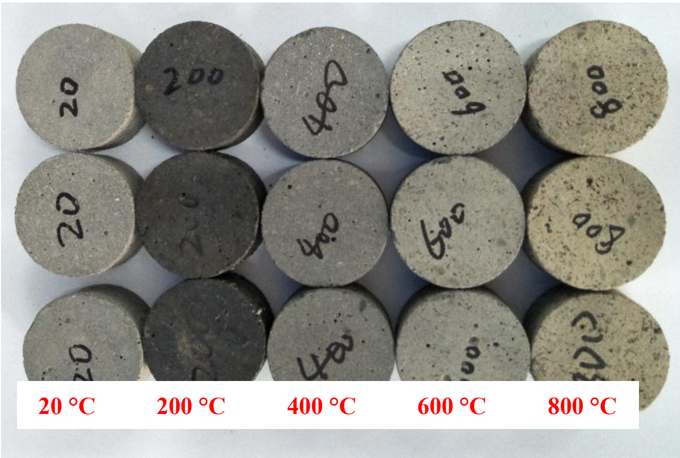

Figure 4.9. Colour changes after exposure to different temperatures.

Colour changes of UHPC specimens after exposure to different elevated temperatures are displayed in Figure 4.9. It can be seen the specimen experienced 200 °C had the darkest colour among all the samples. As analysed above, at 200 °C PP fibres melted but did not decompose and some melted PP permeated through the surfaces of the specimen, darkening its colour. After exposure to 400 °C, the colour was much lighter than 200 °C but a litter darker than 20 °C. It was attributed to that most of the melted PP but not all decompose at 400 °C. Smoke could be still seen even when the temperature was up to 480 °C during the heating process. After being heated to 600 °C, the specimen turned to whitish gray, with a vague texture on its surfaces. The colour became pale brown and surface texture was vaguer after the specimen was subjected to 800 °C.

4.2.2 SHPB tests under high temperatures

4.2.2.1 Effect of temperature on strain rate

In the SHPB tests, projectile velocity of the striker bar was controlled by gas pressure in the gas cannon. Totally five different gas pressures, i.e. 0.25, 0.3, 0.35, 0.4, 0.45 MPa, were used and they corresponded to five projectile velocities, i.e. 7.2, 8.8, 10.1, 11.2, 12.2 m/s respectively. The principle of choosing the projectile velocities is under the lower bound the ultimate stress of the specimen should be obtained in the test and the upper bound is determined based on the capacity of the SHPB facility. Under each projectile velocity, the relationship between strain rate and temperature is depicted in Figure 4.10. It can be seen with increase of projectile velocity the strain rate rose under whatever temperature from 20 to 800 °C. Under whatever striking speed, the strain rate grew with temperature increased from 20 to 200 °C, and then declined when the specimen was heated up to 600 °C, and grew again between 600 and 800 °C. Except under 7.2 m/s projectile velocity, the strain rate under 200 °C was the highest among all the target temperatures and was close to the one obtained under 800 °C. The specimen exposed to 200 °C seemed weakened or softened compared to under 20, 400 and 600 °C and similar results were observed by Su et al. (Su et al. 2014). The reason could be under 200 °C the vapour building up in the specimen was far less than released, as discussed above, caused internal cracks and huge tensile stress distributed throughout the specimen. The accumulated cracks and tensile stress made the specimen considerably vulnerable to the impact loading from the pressure bars.

Figure 4.11 shows under different elevated temperatures the relationship between strain rate and projectile velocity. It reveals strain rate went up with increase of projectile velocity under whatever temperatures. The specimen had the highest strain rate under 200 °C and the lowest strain rate under 600 °C under all but the lowest projectile velocity at around 7.2 m/s. The strain rates under 400 and 600 °C were higher than that under room temperature when the projectile velocity was low, but with increase of velocity the situation was reversed. Also, the slope of the five curves indicates the strain rates under

400 and 600 °C were a little less sensitive to projectile velocity than under the other three temperatures.

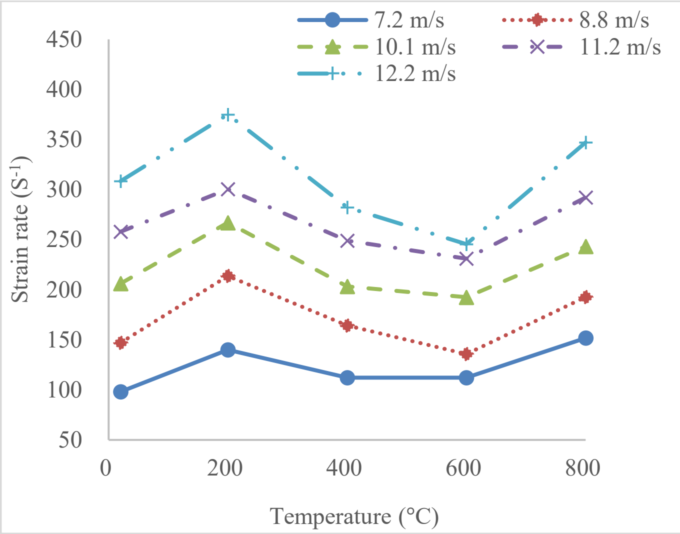

Figure 4.10. Relationship between strain rate and temperature under different projectile velocity.

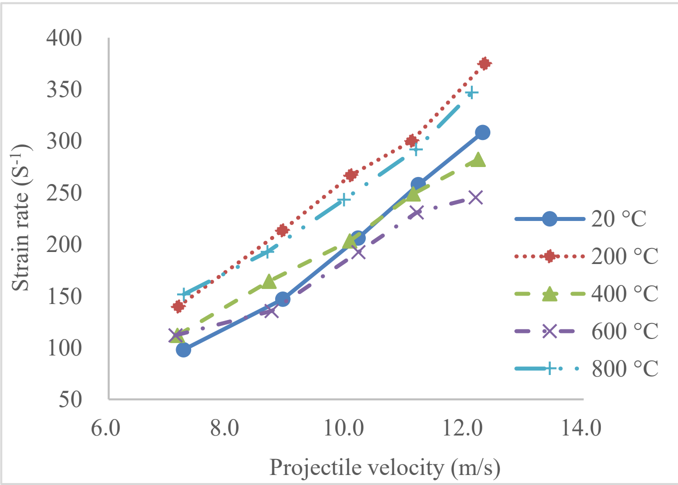

Figure 4.11. Relationship between strain rate and projectile velocity under different temperatures.

Figure 4.12 shows the comparison of relationship between strain rate and temperature between under high temperatures and exposed to the same temperatures but then cooled down under impact of 10.1 m/s projectile velocity. It can be seen the specimen under high temperatures, especially 200 and 400 °C, was much softer than the specimen cooled down to room temperature. As discussed above, the hot specimens under 200 and 400 °C suffered considerable internal vapour pressure which weakened the specimens, while the cooled-down specimens did not. However, under 600 and 800 °C, vapour fully escaping from the hot specimen made the strain rate close to that of the cooled-down specimen.

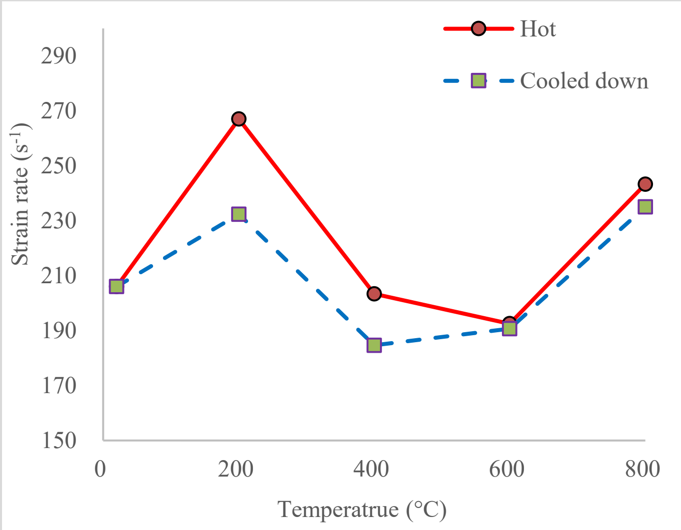

Figure 4.12. Comparison between tested hot and cooled down under 10.1 m/s projectile velocity.

4.2.2.2 Damage appearances of specimens subjected to combined loading

Under the combined loading of high temperature and impact, the damage appearances of the specimens are displayed in Table 4.2. At room temperature, the specimen remained integrity under whatever projectile velocities, benefiting from the presence of hybrid fibres. Only slight damage occurred when the projectile velocity was 7.2 m/s. Under 200 °C, the specimen was crushed under striking of almost all projectile velocities except 7.2 m/s, which resulted from its huge internal vapour pressure. As discussed in Chapter 3, after exposed to 400 °C the specimen made a considerable improvement in its quasi-static compressive strength measured after cooled down in comparison with those under room temperature. However, in hot conditions the specimen was crushed under high projectile velocities because vapour pressure was not completely released. Under 600 °C, the specimen retained more integrity under low projectile velocity than under 400 °C due to complete release of vapour. However, due to decrease of strength of steel fibre and bond strength between steel fibre and concrete matrix, the specimen under 600 °C suffered crushed damage when subjected to high projectile velocity, the debris was larger than under 400 °C though. Softened and loosened under 800 °C, the specimen exhibited ductile damage mode when subjected to low projectile velocities. With increase of projectile velocity, the specimen under 800 °C was completely crushed to small particles as steel fibre lost almost all its strength (Eurocode 2005).

Table 4.2. Damage appearances

Temperature (°C)	Projectile velocity (m/s)				
	7.2	8.8	10.1	11.2	12.2
20					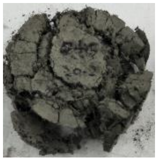
200			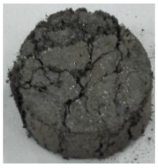		
400			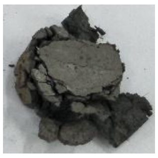		
600					
800					

4.2.2.3 Dynamic compressive strength under combined loading

SHPB test results are listed in Table 4.1. Under simultaneous loading of elevated temperature and impact, relationships between stress and strain are displayed in Figure 4.13 and Figure 4.14. Figure 4.13 shows stress-strain curves under different strain rates when exposed to 400 °C. It can be seen with higher strain rate, the peak stress became greater and the stress-strain curve became broader, indicating absorbing more impact energy. The critical strain corresponding to the peak stress also tended to increase with growing strain rate. Figure 4.14 shows stress-strain curves under different temperatures when projectile velocity was 10.1 m/s. Compared to room temperature, the specimen under 200 °C was softened and weakened due to great internal vapour pressure, with distinctly lower modulus of elasticity and strength. Its stress-strain curve had the flattest descending portion among all the curves. The curve of 400 °C had a similar shape to that of room temperature, but showed a little deterioration due to undischarged vapour pressure. Exposed to 600 °C, the UHPC had the highest strength and the narrowest stress-strain curve. Under 800 °C, the UHPC was mostly softened and its strength was close to that under 200 °C.

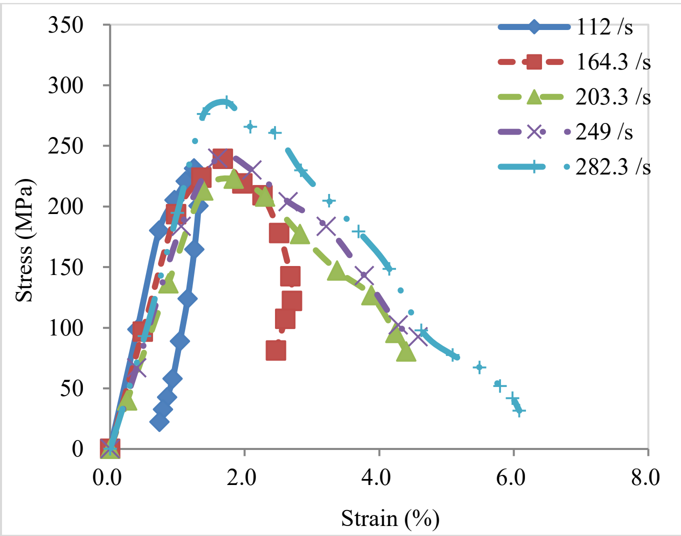

Figure 4.13. Stress versus strain curves with different strain rates under 400 °C.

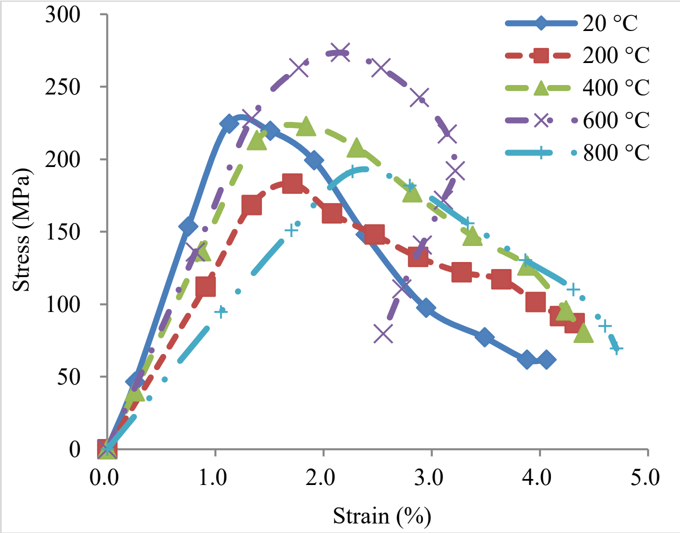

Figure 4.14. Stress versus strain curves with different temperatures under projectile velocity of 10.1 m/s.

Relationships between dynamic peak stress and strain rate are shown in Figure 4.15. It can be seen that with increase of strain rate, peak stress tended to rise for all temperatures, especially 20, 400 and 600 °C. When heated to 400 °C, improvement mechnism of strength was discussed in Chapter 3. However, inside the UHPC specimen there was still some undischarged vapour, limiting the increase of dynamic strength. The specimen had the highest dynamic peak stress under 600 °C due to complete release of vapour, despite decomposition of CH and C-S-H. With higher strain rate, the peak stress increased steeper under 400 and 600 °C. The reason could be that with quick deformation micro cracks within the specimen did not have enough time to develop and propagate before peak stress was reached. It is worth noting the specimens under 200 and 800 °C had relatively large strain rate but low strength and flat curves of stress versus strain rate. With relatively high strain rate of 350 /s under 800 °C, little strain rate effect was observed due to softening of the specimen, as can be seen from Figure 4.15. Compared to dynamic strength under room temperature, strength increase ratio versus strain rate curves under various temperatures are depicted in Figure 4.16. With increase of strain rate, the strength increase ratio under 400 and 600 °C went down slightly first but then went up sharply to 10% and 17% respectively. In contrast, the strength increase ratio under 200 and 800 °C almost remained level at around -25% across strain rate range from 150 to 300 /s.

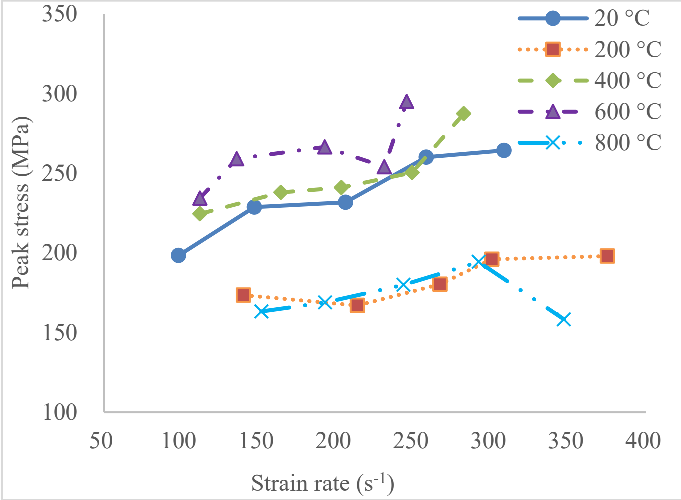

Figure 4.15. Relationship between peak stress and strain rate under different temperatures.

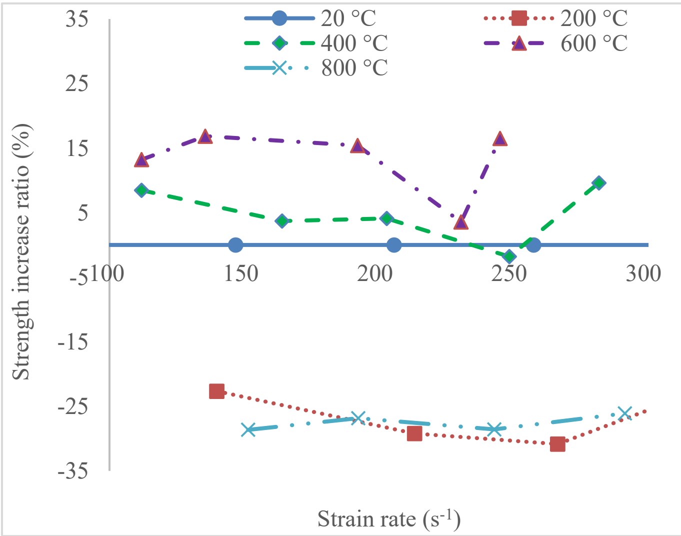

Figure 4.16. Dynamic compressive strength increase ratio versus strain rate under different temperatures.

A comparison of strength under different temperatures between tests under high temperature and tests after cooled down is displayed in Figure 4.17. Peak stress obtained at high temperatures 200 and 400 °C were well below that measured after cooled down, which proved the assumption made above that there were damaging vapour pressure inside the specimen especially at 200 °C. At 600 °C, the 'hot' strength was around 5% higher than the 'cooled-down' strength. It could be attributed to that extra damage occurred to the specimen during its cooling while there was no vapour pressure inside the specimen even though it was in hot state (Hager 2013). Strength after cooled down from 800 °C was again apparently greater than that under high temperature. Under 800 °C, increased porosity and cracks made the specimen softened and weakened. However, after cooling down and being placed in the air for some time, rehydration could take place and help restore some strength.

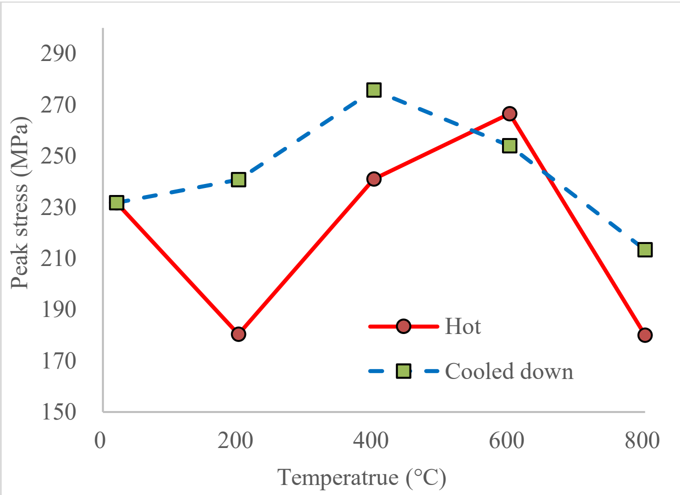

Figure 4.17. Comparison of strength versus temperature curves between tested hot and cooled down under projectile velocity of 10.1 m/s.

4.2.2.4 Modulus of elasticity under combined loading

In this study, modulus of elasticity is defined as slope between two points on ascending portion of stress-strain curves corresponding to 60% and 40% of peak stress respectively, which was also adopted by Su et al. (Su et al. 2014). Under different temperatures, relationships between modulus of elasticity and strain rate are illustrated in Figure 4.18. It can be seen with increase of strain rate, modulus of elasticity under room temperature had a growing trend, while for high temperatures from 200 to 800 °C it tended to fall. Under high temperatures, the UHPC was softened due to presence of cracks and vapour pressure, which resulted in negative effect of strain rate on its rigidity. From Figure 4.19 which shows relationships between modulus of elasticity increase ratio and strain rate under different temperatures, it can be known the maximum degradation of modulus of elasticity reached up to 67% when the specimen was heated to 800 °C and impacted with a strain rate of 243 /s.

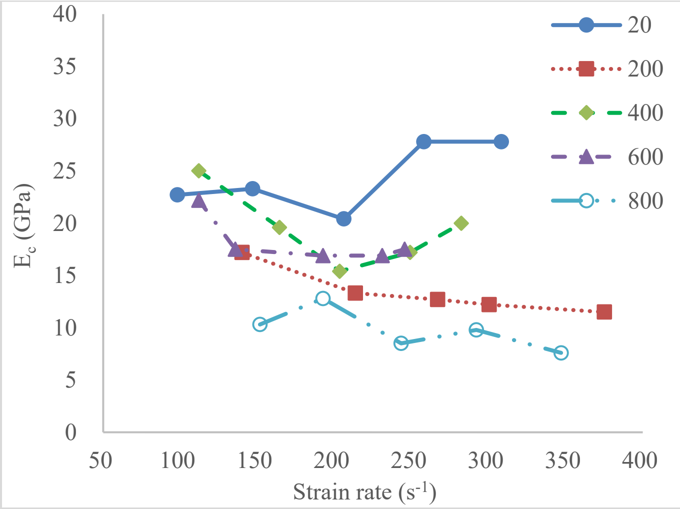

Figure 4.18. Relationship between modulus of elasticity and strain rate under different temperatures.

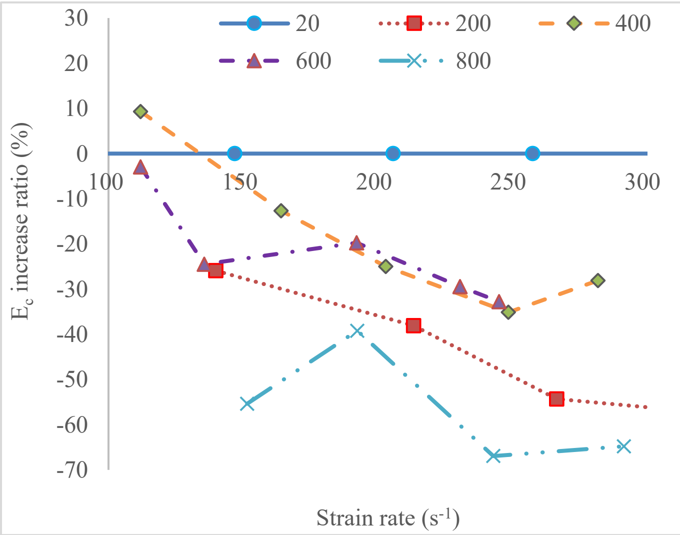

Figure 4.19. Modulus of elasticity increase ratio versus strain rate under different temperatures.

Figure 4.20 shows the difference of modulus of elasticity between the specimen under high temperatures and the cooled-down specimen after exposed to the same high temperatures when the projectile velocity was 10.1 m/s. It can be seen with increase of temperature, modulus of elasticity tended to go down in both states. Also, when temperature rose from 200 to 400 °C, modulus of elasticity increased in the two situations. The reason could be that over this temperature range more and more C-S-H gel was produced, making the internal structure of the UHPC more compact. From 400 to 600 °C, modulus of elasticity of the cooled-down specimen decreased because extra damage occurred during the cooling process. Under whatever high temperatures, modulus of elasticity in hot state was lower than that in cooled state, especially at 200, 400 and 800 °C. It is easy to understand since high temperature usually accelerate molecular movement of matter and extend its range, softening the matter.

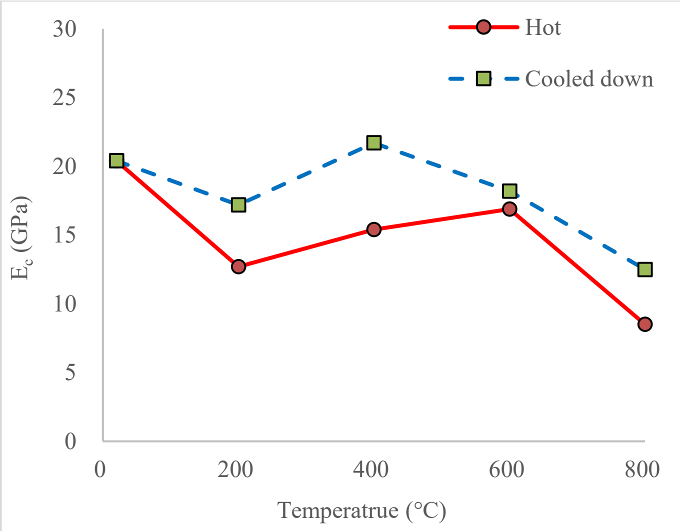

Figure 4.20. Comparison of modulus of elasticity versus temperature curves between tested hot and cooled down under projectile velocity of 10.1 m/s.

4.3 Summary

A newly developed UHPC was investigated with both quasi-static compression tests and dynamic tests. The quasi-static compression tests were conducted after the specimen was exposed to high temperatures up to 1000 °C and then cooled down to room temperature, while the dynamic tests were carried out under combined high temperatures up to 800 °C and impact loading using an electricity-furnace-integrated SHPB system. The dynamic tests were done both under high temperatures and after cooling down and comparisons were made between these two scenarios. Based on the tests, the following conclusions may be drawn:

1) The UHPC had relatively high static and dynamic residual compressive strength after exposed to elevated temperatures.
2) The highest compressive strength of the UHPC under simultaneous thermal and impact

loading occurred at 600 °C, while after cooling down to room temperature the UHPC achieved its maximum strength at 400 °C both in static and dynamic compression cases.

3) Tested in hot state, the UHPC suffered severe degradation in strength and rigidity at 200 °C due to great internal vapour pressure. Much less such degradation happened to the UHPC at 400 °C and no such degradation was observed above 600 °C.
4) PP fibre melting at around 160 °C helped release vapour pressure and reduce explosive spalling possibility. However, PP decomposed into various volatiles within temperature range of 360 to 400 °C, increasing internal vapour pressure. In this study, most explosive spalling happened under around 370 °C. Heating rate needed to be strictly limited to prevent explosive spalling especially between 320 and 380 °C.
5) The UHPC at high temperatures was softer and had lower dynamic compressive strength than the one cooled down to room temperature after being heated to the same temperatures as the former.
6) Strain rate effect was observed on both compressive strength and modulus of elasticity of the UHPC. With increase of strain rate, strength tended to rise while modulus of elasticity had a trend of decrease at high temperatures from 200 to 800 °C.

CHAPTER 5

TENSILE STRENGTH OF UHPC SUBJECTED TO COMBINED EFFECT OF ELEVATED TEMPERATURE AND IMPACT LOADING

5 TENSILE STRENGTH OF UHPC SUBJECTED TO COMBINED EFFECT OF ELEVATED TEMPERATURE AND IMPACT LOADING

In the current work, splitting tensile tests were conducted on a UHPC that was newly developed by Liang et al. (Liang et al. 2018) and had the exclusively high residual compressive strength after exposure to elevated temperatures up to 1000 °C. The specimens were tested both in static and dynamic conditions at temperatures of 20, 200, 400, 600 and 800 °C such that coupled effect of high temperature and impact loading on this UHPC was revealed. Besides, static and dynamic compressive tests were also carried out in order to make a comparison between residual compressive strength and splitting tensile strength. The dynamic tests were implemented using a self-designed Split Hopkinson Pressure Bar (SHPB) system including a heating facility.

5.1 Experimental details

For each test, three specimens were prepared. Specimens for static splitting tensile tests and SHPB tests were sliced from UHPC cylinders, which were drilled out from UHPC blocks in size of $100\times100\times400$ mm after 28 days curing. The specimens used in SHPB tests were ground on their two end faces to ensure parallel to each other with a tolerance of 0.02 mm. 100 mm cubic specimens were used for static compression tests. The specimen sizes are listed in Table 5.1. To know the size effect of splitting tensile strength, a comparative test was conducted under room temperature using specimens with sizes of $\Phi50\times25$ mm and $\Phi100\times50$ mm. The results showed the size effect on splitting tensile strength of the UHPC was negligible. For each of the SHPB tests, a mat made of pot clay was used to align the specimen with the pressure bars due to diameter difference between them, as shown in Figure 5.1.

Table 5.1. Specimen sizes (unit: mm)

Static tension	Dynamic tension	Static compression	Dynamic compression
$\Phi100\times50$	$\Phi50\times25$	$100\times100\times100$	$\Phi50\times25$

Figure 5.1. A specimen with a mat for dynamic splitting tensile tests.

Figure 5.2. Setup of static splitting tensile tests.

The static tests conformed to the Chinese standard GB/T 50081-2002. Firstly, the specimen was heated in an electric furnace at a rate of 4 °C/min until the target temperature was reached and remained subjected to the constant temperature for 2 hours.

Then, it was moved out and placed on the test stand as shown in Figure 5.2 for a splitting tensile test. The loading rate was controlled at 0.05 MPa/s for splitting tensile tests and 0.9 MPa/s for compressive tests.

For the dynamic splitting tensile tests, the self-designed SHPB system as discussed in Section 4 was used. With the specimen in hot state, the dynamic splitting tensile tests were implemented under 3 different projectile velocities, i.e. 0.15, 0.20 and 0.25 m/s. Only one projectile velocity was applied to cooled-down tensile tests, i.e. 0.2.

5.2 Results and discussion

Results for splitting tensile tests are reported in Table 5.2. The splitting tensile strength f_{st} is calculated using the following equation:

$$f_{st} = \frac{F}{\pi DH} \tag{5.1}$$

where F is the force symmetrically acting on the specimen along its diameter; D and H are the diameter and the thickness of the specimen respectively. In the case of dynamic loading in the SHPB tests, F can be obtained from the following (Wu et al. 2008):

$$F = \sigma_t(t)A_b \tag{5.2}$$

where $\sigma_t(t)$ is the stress calculated from the strain on the transmission bar; A_b is the cross-section area of the pressure bars.

It should be noted the static strength is for the tests carried out in hot state only, while the dynamic strength is for both in hot and cooled-down states. The DIFs were derived only for splitting tensile tests conducted in hot state.

Table 5.2. Results of splitting tensile tests

Tempera-ture (°C)	Static strength (MPa)	Gas pressure (MPa)	Projectile velocity (m/s)	Dynamic strength (MPa)		DIF (Hot)
				Hot[a]	Cooled down[b]	
20	13.0	0.15	3.3	14.6		1.12
		0.20	5.4	19.2		1.47
		0.25	7.2	22.6		1.74
200	11.0	0.15	3.7	11.4		1.03
		0.20	5.4	18.3	20.1	1.67
		0.25	7.3	21.0		1.91
400	12.9	0.15	3.2	14.5		1.12
		0.20	5.4	19.9	21.1	1.54
		0.25	7.2	22.4		1.74
600	9.9	0.15	3.3	14.1		1.42
		0.20	5.6	13.7	16.8	1.39
		0.25	7.2	18.2		1.83
800	5.3	0.15	3.2	7.9		1.49
		0.20	5.5	9.2	12.5	1.73
		0.25	7.2	15.8		2.98

[a] 'Hot' denotes the test was done when the specimen was nearly as hot as the target temperature.

[b] 'Cooled down' denotes the test was done after the specimen was cooled down to room temperature.

5.2.1 Static splitting tensile tests at high temperatures

5.2.1.1 Failure appearances under static tests

Under static splitting tensile tests, failure appearances of the UHPC specimens at the five target temperatures are listed in Table 5.3. With increase of temperature from 20 to 800 °C, colour of the specimen changed from grey to whitish grey and then pale brown. Heated from room temperature to 600 °C, the specimen suffered wider major cracks at higher temperature, which could be attributed to deterioration of mechanical properties of UHPC matrix and steel fibre and degradation of interfacial performance between steel fibre and the matrix. According to the Eurocode En 1992-1-2 (Eurocode 2004), for cold worked steel reinforcement, when it is heated to 200 °C it maintains its full original strength and 87% of its original modulus of elasticity. However, strength and modulus of elasticity of the reinforcement fall to 94 % and 56% respectively at 400 °C, and only 40% and 24 % respectively at 600 °C. From Table 5.3, it can be seen failure appearance at 800 °C was distinct from the others. Rather than parallel to the first crack, the second crack was nearly perpendicular to it and the cracks had a width between at 400 and 600 °C. The reason could be, under 800 °C, the UHPC was loosened and softened (Liang et al. 2018).

Table 5.3. Failure appearances under static tests

Temperature (°C)				
20	200	400	600	800
				

5.2.1.2 Static splitting tensile strength

From Table 5.2, it can be seen at higher temperatures the static splitting tensile strength tended to drop. At 200 °C, despite melting of PP fibre, built-up pore pressure was far less than fully released. In the tests, smoke could be observed from 280 to 480 °C and most explosive spalling happened between 320 and 380 °C. Therefore, the specimen was weakened by pore pressure, cracks and great distributed tensile stress, resulting in a sharp drop in strength at 200 °C. Heated to 400 °C, the UHPC became more compact and harder due to pozzolanic reactions and pore pressure had been almost released, which contributed to improvement in compressive strength (Liang et al. 2018). However, degradation of steel fibre, to which tensile strength is usually more sensitive than compressive strength, could restrain the improvement in tensile strength. With exposure temperature growing from 400 to 800 °C, the splitting tensile strength kept falling sharply to only 5.3 MPa. Calcium hydroxide (CH) decomposed between 430 and 600 °C and calcium silicate hydrate (C-S-H) started to decompose at 560 °C (Rashad et al. 2012), which undermined mechanical properties of the UHPC matrix and bond performance between the matrix and steel fibre. Together with substantially worsened properties of steel fibre, all these resulted in the loss of splitting tensile strength at 600 and 800 °C.

Figure 5.3 shows the normalized relationships between temperature and splitting tensile strength of the UHPC along with high strength concretes (HPCs) from other researchers (Behnood and Ghandehari 2009; Khaliq and Kodur 2011) and concrete from the Eurocode En 1992-1-2 (Eurocode 2004). Compared to other concretes, the UHPC exhibited excellent fire resistance in terms of residual tensile strength. Exposed to elevated temperatures up to 800 °C, it retained 41% of its original tensile strength, well above the others.

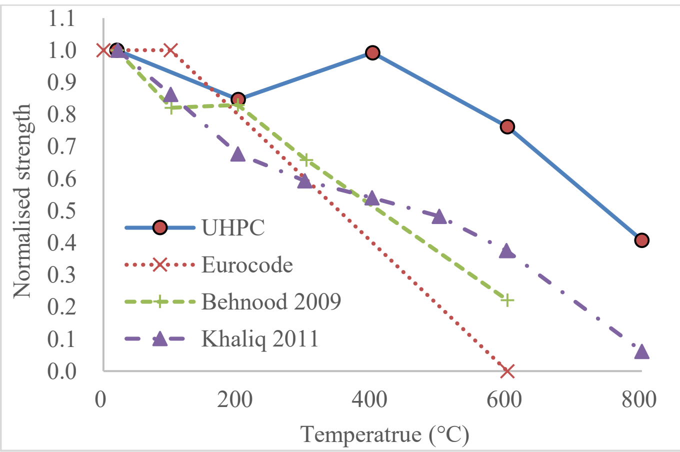

Figure 5.3. Normalised splitting tensile strength versus temperature.

5.2.1.3 Comparison between static tensile strength and compressive strength at high temperatures

Comparison between normalised static tensile strength and normalised static compressive strength is made in Figure 5.4Figure 5.4. At 200 °C, there is a much bigger fall for compressive strength than tensile strength. The reason could be, as discussed above, there was great built-up pore pressure not yet released in the UHPC matrix due to its compactness, which could severely affect strengths of the UHPC. Under splitting tensile tests, fast cracking initiated along the loading axis contributed to release of vapour and thus helped reduce loss of tensile strength. By contrast, under compression vapour was hard to escape and pore pressure was even aggravated with increase of loading at the early stage of the test. Eventually, the specimen failed under combined pore pressure and compressive loading, seeing a greatly lowered compressive strength. Another big gap between tensile strength and compressive strength is at 600 °C, as shown in Figure 5.4. On the one hand, drastic performance degradation of steel fibre greatly impaired the tensile strength of the UHPC exposed to 600 °C. On the other hand, pozzolanic reaction making the UHPC matrix more compact and harder improved compressive strength in comparison with the room-temperature strength even though degradation of steel fibre and decomposition of CH and C-S-H had negative effects on the compressive strength.

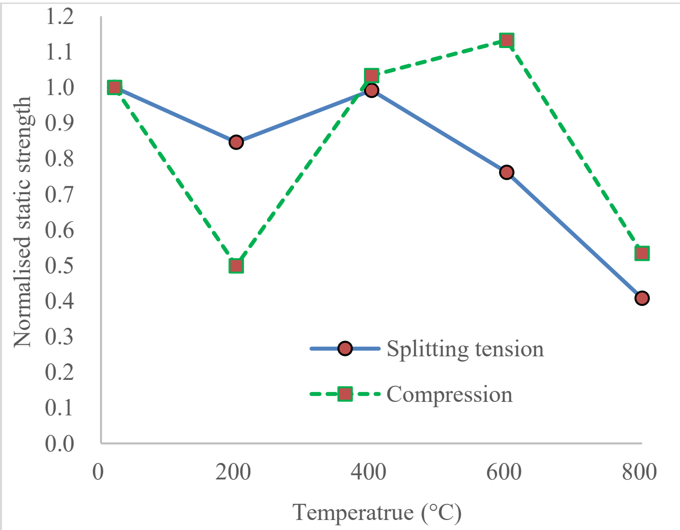

Figure 5.4. Comparison of normalized static strength between splitting tension and compression.

5.2.2 Dynamic splitting tensile tests at high temperatures

5.2.2.1 Failure appearances under dynamic tests

Table 5.4. Failure appearances under dynamic tests

Temperature (°C)	Projectile velocity[a] (m/s)			
	Hot			Cooled down
	3.3	5.5	7.2	5.5
20				
200				
400				
600				
800				

[a] 'Projectile velocity' is the speed of the striker bar in the SHPB test at the time striking the incident bar.

Table 5.4 shows the failure appearances of the specimens subjected to coupled effect of high temperature and dynamic loading, both in hot and cooled-down states. Similar to the static tests, with rise of temperature, severity of damage was increased, especially under higher projectile velocity. At room temperature or under low projectile velocity of 3.3 m/s, no debris was observed. However, when temperature was above 400 °C and projectile velocity was larger than 5.5 m/s, debris was observed for all the specimens except the one tested cooled-down after heated to 400 °C. Especially, under 800 °C and 7.2 m/s impact loading, the specimen was completely crushed. As a comparison, damage of the specimens tested after cooled down was less severe than those tested hot under 5.5 m/s impact loading.

5.2.2.2 Dynamic splitting tensile strength under combined loading

The relationships between splitting tensile strength and temperature under different projectile velocities up to 7.2 m/s are plotted in Figure 5.5. It can be seen the tensile strength tended to fall with increase of temperature under whatever projectile velocity and the curves under dynamic loading were similar to that under static loading, for which the mechanism of strength degradation has been explained in Subsection 5.2.1.2. Particularly, the tensile strength experienced a fast drop after temperature was beyond 400 °C.

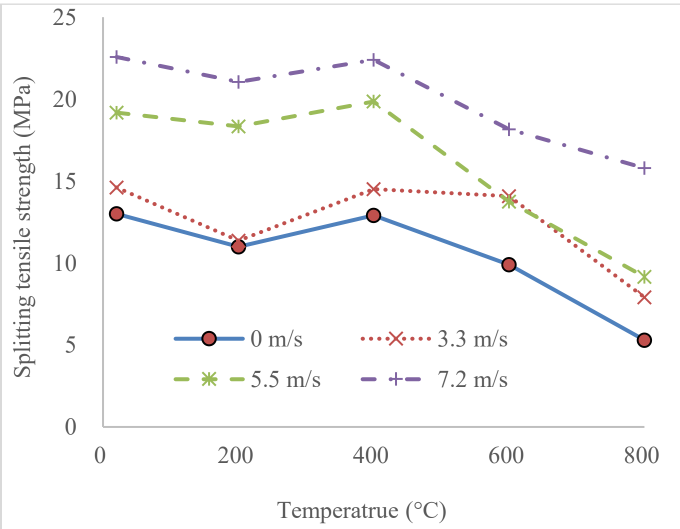

Figure 5.5. Relationships between peak tensile stress and temperature under different projectile velocities.

Figure 5.6 displays the curves of DIF versus projectile velocity at the five target temperatures. As expected, the DIF had a trend of going up with rise of projectile velocity due to the so-called effect of strain rate, which was also observed in the splitting tensile tests on concretes by other researchers (Caverzan et al. 2013; Zhao et al. 2016). Under each projectile velocity, the specimen had relatively close DIF values at all temperatures except 800 °C. At 800 °C, the DIF increased sharply to 2.98 under impact speed of 7.2 m/s, to which similar result was obtained by Caverzan et al. (2013), who observed the high performance concrete (HPC) achieved the maximum DIF at 600 °C. This abnormity could be attributed to the fact that at a very high temperature such as 800 °C the UHPC was loosened and softened so that under relatively high impact loading its failure could be induced by crush instead of splitting tension due to lack of time for the cracks to propagate. In fact, from Table 5.4, it can be seen the specimen at 800 °C was completely crushed under the projectile velocity of 7.2 m/s.

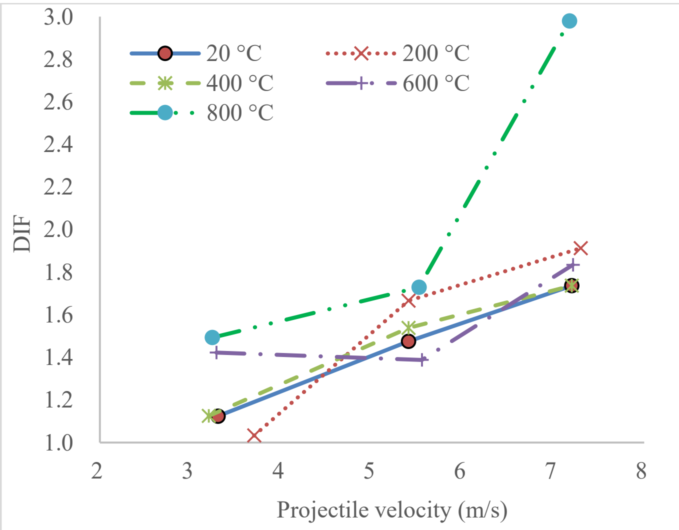

Figure 5.6. Relationships between DIF and projectile velocity at different temperatures.

Compared with strengths under various projectile velocities at room temperature, tensile and compressive strength increase ratios at different elevated temperatures are depicted in Figure 5.7. It should be noted that the projectile velocity for the dynamic splitting tensile tests were in a different bracket with for dynamic compressive tests. From Figure 5.7(a) it can be seen, except at 400 °C and under 5.5 m/s impact speed, dynamic tensile strength at all elevated temperatures suffered a degree of loss compared to room temperature. At 200 and 400 °C, the tensile strength ratio went up first but then down with increase of projectile velocity, while at 600 and 800 °C it followed an opposite trend. By contrast, under whatever projectile velocity, dynamic compressive strength at 400 and 600 °C enjoyed an improvement compared to room temperature, while at 200 and 800 °C it suffered a great loss, as can be known from Figure 5.7(b).

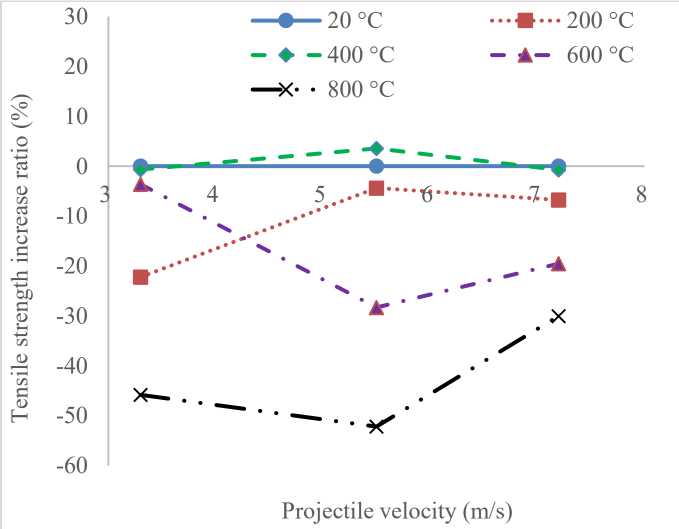

(a) Dynamic splitting tensile strength increase ratio

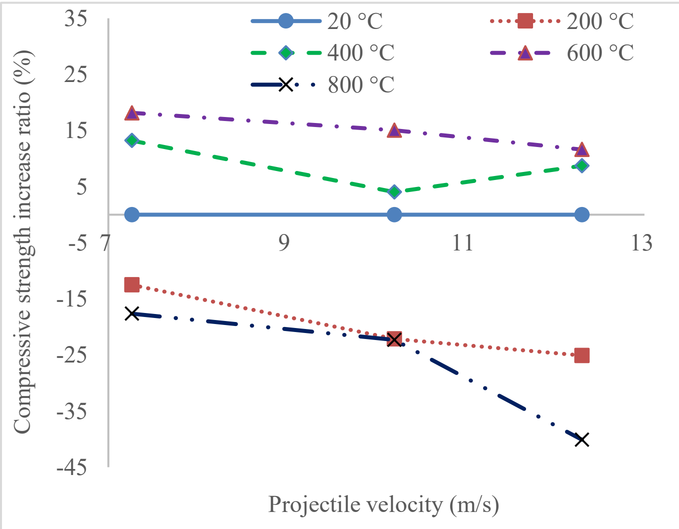

(b) Dynamic compressive strength increase ratio

Figure 5.7. Dynamic strength increase ratio versus projectile velocity under different temperatures.

5.2.2.3 Comparison between tensile strength and compressive strength under

combined loading

Under impact speed of 7.2 m/s, relationships between normalised strength (both tensile and compressive strength) and temperature are plotted in Figure 5.8. The curves have a similar pattern to those of static loading as shown in Figure 5.4. However, at 200 and 400 °C, the normalised dynamic compressive strength had a noticeable enhancement comparted to under static loading, while the normalised dynamic tensile strength remained almost unchanged. The reason could be that cracks, which is caused by built-up pore pressure and is the main factor weakening the UHPC exposed to these temperatures, exerted a less negative effect on compressive strength under dynamic loading than static loading due to lack of time to fully propagate within the matrix.

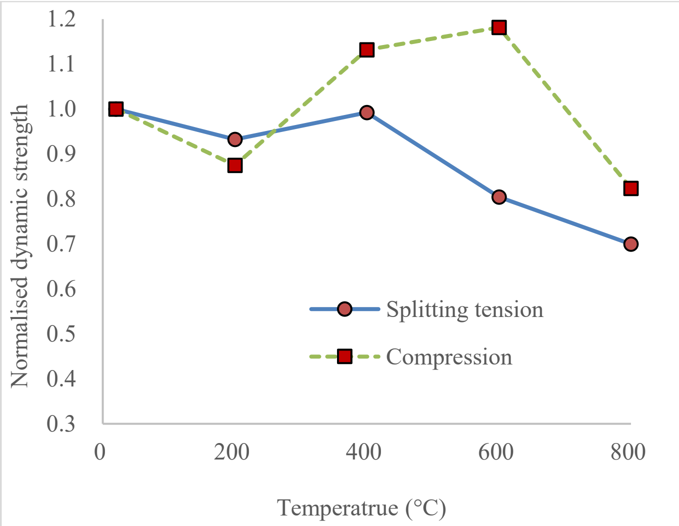

Figure 5.8. Comparison of normalised dynamic strength between splitting tension and compression under projectile velocity of 7.2 m/s.

Figure 5.9 exhibits the ratio of compressive strength to tensile strength at high temperatures under two loading scenarios, i.e. static loading and 7.2 m/s impact loading. It can be seen this ratio fluctuated wildly with variation of temperature. With temperature growing from 20 to 200 °C, the ratio dropped to 5.4 for static loading and 8.3 for dynamic loading respectively. From 200 to 600 °C, it increased to 13.3 at 400 °C but then decreased to 12.4 at 600 °C for static strength and grew up to 12.9 for dynamic strength. It then fell from 600 to 800 °C under both loading scenarios. The fluctuation of the ratio under dynamic loading was smaller than static loading across the temperature range from 20 to

800 °C.

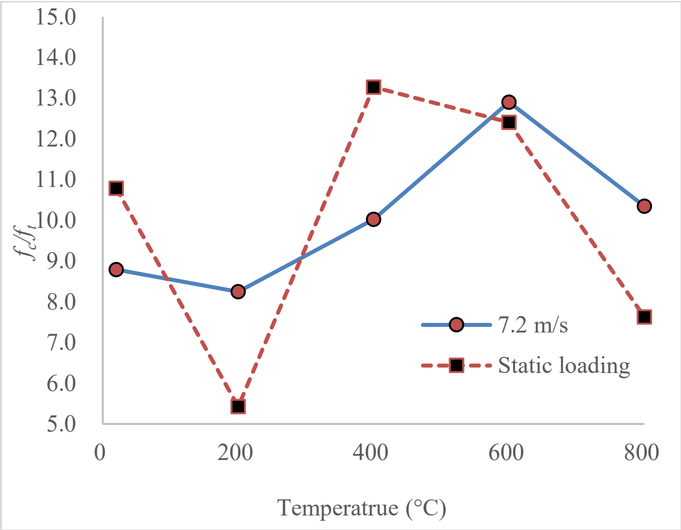

Figure 5.9. Ratio of compressive strength to splitting tensile strength under static loading and projectile velocity of 7.2 m/s.

5.2.2.4 Comparison between strengths obtained in hot state and cooled down state

Figure 5.10 shows comparison between dynamic strengths in hot state and cooled-down state after exposure to the same temperature as the former. The tensile strength was obtained under projectile velocity of 5.5 m/s while the compressive strength was achieved under 10.1 m/s at various temperatures from 20 to 800 °C. It can be seen from Figure 5.10, generally, strength in hot state was lower than in cooled-down state, both true for tensile strength and compressive strength. The reason could be there was pore pressure and cracks in the hot UHPC matrix exposed to elevated temperatures from 200 to 400 °C, which exerted a negative effect on its strengths. At 600 °C, properties of steel fibre were substantially worsened by the high temperature but were restored after cooling down, leading to higher cooled tensile strength than hot tensile strength. However, at 600 °C the hot compressive strength was a little higher than the cooled one because of extra damage during the specimen's cooling (Hager 2013). Cooled down from 800 °C, the residual tensile and compressive strength were both higher than when the specimen remained in hot state, which could be attributed to restoring of steel fibre properties after cooled down and rehydration. Overall, the strength difference between the two thermal states ranged from 6% to 26% for tensile strength and from 5% to 25% for compressive strength under the respective impact loading.

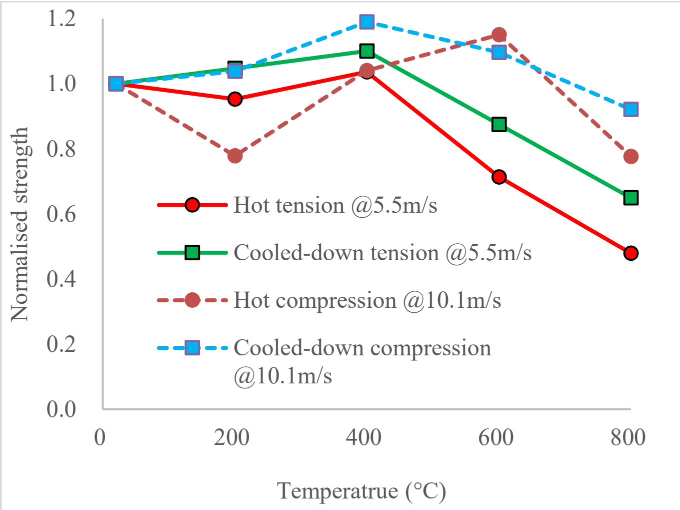

Figure 5.10. Comparison of normalised dynamic strength between hot state and cooled-down state.

5.3 Summary

This Section is aimed at investigating the coupled effect of temperature and impact loading on tensile strength of the UHPC with high fire resistance and the relationship between tensile strength and compressive strength at elevated temperatures. The static tests were carried out when the specimen remained in hot state after being heated to the target temperatures from 20 to 800 °C, while the dynamic tests were implemented both in hot state and cooled-down state. The test results and above analysis allow to reach the following conclusions:

1) Under static loading, the UHPC suffered wider major cracks at higher temperatures due to degradation of UHPC matrix, steel fibre and interfacial performance between steel fibre and matrix.

2) Under both static and dynamic loading, splitting tensile strength fluctuated from room temperature to 400 °C and then dropped sharply beyond 400 °C. Specifically, the static splitting tensile strength fell to 41% of its original strength, but still well above other concretes.

3) Effect of strain rate on splitting tensile strength was observed for all the target temperatures.
4) In splitting tensile tests, failure of the UHPC heated to 800 °C could be induced by crush instead of splitting tension, indicating splitting tensile tests may be inappropriate for concretes at very high temperatures.
5) The ratio of compressive strength to splitting tensile strength fluctuated wildly with variation of temperature, which means taking compressive strength as the representative of the mechanical properties of a concrete at elevated temperatures is no longer acceptable. The fluctuation of the ratio under dynamic loading was smaller than static loading across the temperature range from 20 to 800 °C.
6) The mechanism of damage induced by elevated temperature to tensile strength was different with compressive strength of the UHPC. While degradation of steel fibre weighed heavily on loss of tensile strength above 600 °C, built-up pore pressure and cracks played an important role in deterioration of compressive strength especially from 200 to 400 °C.
7) Damage to specimens tested after cooled down was less severe than tested hot under impact loading. Both tensile strength and compressive strength in hot state were lower than in cooled-down state. This difference for tensile strength and compressive strength was similar.

CHAPTER 6

NUMERICAL STUDY OF THERMAL PROPERTIES OF SFRC/UHPC USING MESO-SCALE MODELLING

6 NUMERICAL STUDY OF THERMAL PROPERTIES OF SFRC/UHPC USING MESO-SCALE MODELLING

A meso-scale model is developed to investigate effect of steel fibre on thermal conductivity of SFRC. Delaunay triangulation is employed to generate the unstructured mesh for SFRC materials. The model is validated using existing experimental data. Then, it is used to study how model thickness affects simulation outcomes of thermal conductivity of models with different fibre lengths, by which an appropriate thickness is determined for the later analyses. The validated and optimised model is applied to study of relationships between thermal conductivity and factors such as fibre content, fibre aspect ratio and different parts of an SFRC block applying steady-state heat analyses with FEA software ANSYS. The simulation results reveal that presence of steel fibres has an obvious impact on the distribution of temperature and heat flux vector of the SFRC blocks. Besides, fibre content improves thermal conductivity considerably, while fibre aspect ratio only has an insignificant effect.

6.1 Model preparation

6.1.1 Generation of geometric model

In this study, SFRC is considered as a composite of steel fibre and concrete where steel fibre is the main concern. It should be noted that geometry of steel fibres is not considered, though they usually have different shapes. In other words, herein only round straight fibres are used. For heat analyses of SFRCs, no deformation or fibre sliding happens, so shared-node or perfect-bond mode is applied to the linkage of these two materials. The interfacial zone between the fibre and the matrix could have negative effects on thermal transfer between them. Interfacial zone effect is subject to concrete constitution, fibre properties and moisture variation under elevated temperatures. However, lack of such data in the literature makes it difficult to integrate this effect into the numerical model. Nevertheless, the focus of this study is on how fibre parameters, such as content, diameter and length, affect thermal conductivity of SFRCs under room temperature. Random fibres are generated in the numerical computing environment MATLAB using the Rand function. Firstly, a model with cuboid shape is defined. Then one endpoint of a fibre is randomly created within the model. The other endpoint of the fibre keeping a distance of fibre length is randomly determined if it is contained by the model boundaries. After intended number of fibres is reached, the fibre generation process is finished. A meso-scale geometric model of SFRCs is shown in Figure 6.1.

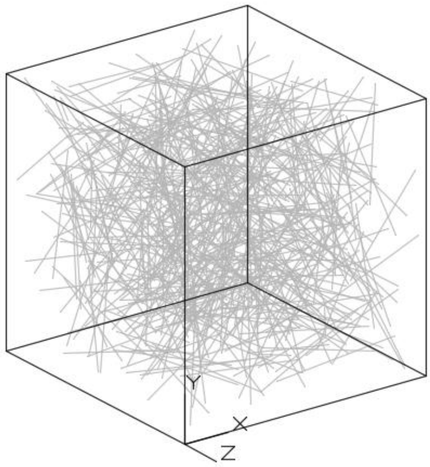

Figure 6.1. A meso-scale model of SFRCs.

6.1.2 Mesh generation with Delaunay triangulation

A Delaunay triangulation is a geometric dual of a Voronoi diagram (Borouchaki and Lo 1995; Watson 1981; Yang 2005). For a given point set on a two-dimensional plane, a Delaunay triangulation of this set ensures the optimal minimum angle in all possible triangulations. This feature can be extended to n-dimension spaces including 3D space, which makes Delaunay triangulation a desirable tool for mesh generation of FEA in case structured mesh is impractical. Incremental algorism of Delaunay triangulation, also referred to as cavity algorism or point-adding algorism, was proposed (Bowyer 1981; Watson 1981) and has been the most popular Delaunay triangulation algorism. Sometimes in practice, there is a given point set, segment set and facet set that need to be contained in a Delaunay triangulation, and this kind of triangulation is called Constrained Delaunay triangulation. In this study, for example, the constraining point set (CPS) consists of model vertices, fibre endpoints and fibre divisional points. The model boundaries including the surfaces and the edges are treated as constraining conditions. As shown in Figure 6.2, the six surfaces of the model are contained by the six constraining facets respectively which constitute the initial constraining facet set (CFS) and the 12 edges make up the initial constraining segment set (CSS). Whenever a new point is inserted to the triangulation, it will be checked if any boundaries of the model, i.e. constraining elements, are encroached by the point. As long as all constraining elements exist in the final Delaunay triangulation, the boundaries of the model will be maintained. Figure 6.2 also shows a containing box that contains all constraining elements and it is used to create the initial Delaunay tetrahedron set (DTeS).

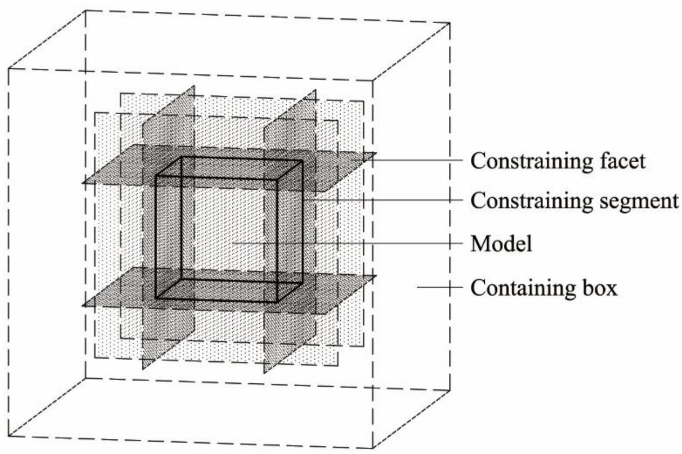

Figure 6.2. Illustration of constraining facets and segments.

In this study, Boundary Face Subdivide (BFS) algorism (Yang 2005) is adopted to process the triangulation and it can be divided into the following steps:

1) Insert each point P in CPS to DTeS one by one, and if any point in CPS lies on a triangle of the Delaunay triangle set of constraining facets (DTS(CF)) then add it to DTS(CF);

2) Segment Subdivide Iterative (SSI) process: check if every segment in the CSS has an empty min-circumsphere. If not, add a divisional point M in a certain region of its midpoint to CPS, CSS and DTeS. The segment is divided into two new segments and replaced by the latter in CSS. If M lies on any triangle of DTS(CF), add it to DTS(CF);

3) Facet Subdivide Iterative (FSI) process: check if every triangle in DTS(CF) has an empty min-circumsphere. If not, calculate its circumcentre and check if the circumcentre encroaches any segment in CSS. If yes, add a divisional point M in a certain region of the encroached segment to the triangulation, otherwise, add the circumcentre. Once a new point is added, the SSI process in step b needs to be carried out.

To help understand the above BFS process, a flowchart is shown in Figure 6.3.

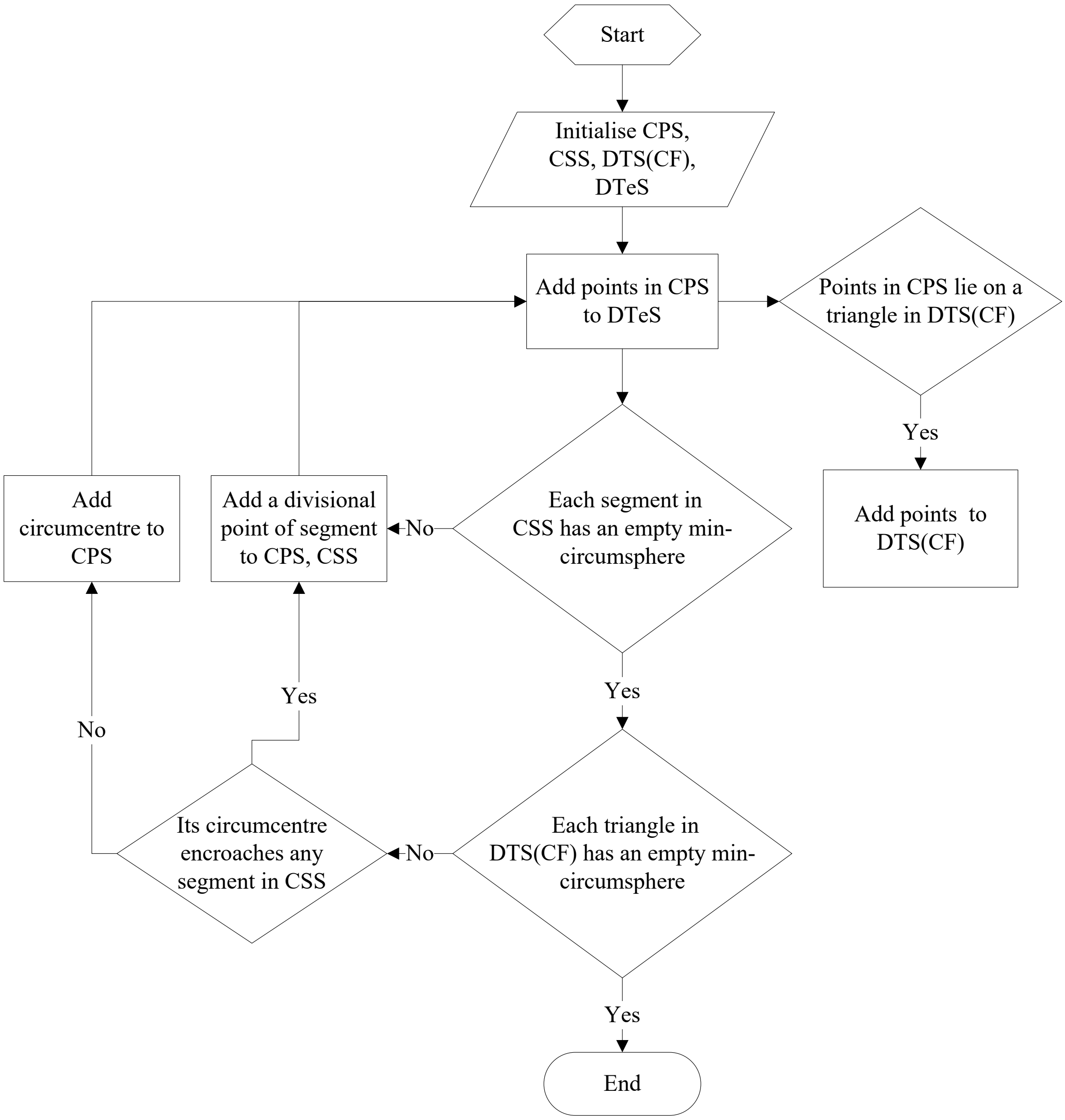

Figure 6.3. Flowchart of BFS process

To meet the requirement of FEA, an optimisation process is needed after the above Delaunay triangulation. Poor quality tetrahedra, such as spear, spike and sliver, have to be removed from the DTeS. Herein a combination of two criteria, radius-edge ratio and min-dihedral-angle, are introduced to eliminate poor quality tetrahedra. Radius-edge ratio is a ratio of circumradius to min-edge of a tetrahedron, and min-dihedral-angle is the minimum dihedral angle of six dihedral angles of a tetrahedron. An optimisation strategy was proposed (Li 2001) to ensure boundaries not to be encroached by adding extra points and it is adopted in this study. As an example to be seen clearly, a Delaunay triangulation of a model with only five fibres is shown in Figure 6.4. It can be seen the developed Delaunay triangulation program has such capability that mesh becomes denser where fibres present. It should be noted for mesh with Delaunay triangulation, one point tetrahedron is used for element formulation of concrete in this study. Prior to the determination, various lengths of average fibre element were attempted to obtain a converged result. In this study, the average fibre element length is set at around 1.4 mm.

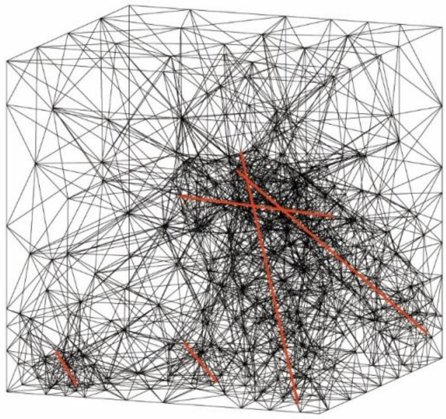

Figure 6.4. Demonstration of Delaunay triangulation of SFRC models.

6.2 Thermal parameters and material models

Heat analysis in the finite element analysis (FEA) software ANSYS is based on the first law of thermodynamics, or principle of conversion of energy. For a closed system without mass change, change of the sum of internal energy, kinetic energy and potential energy is equal to the sum of work and heat contributed by outside as the following:

$$\Delta U + \Delta KE + \Delta PE = Q + W \tag{6.1}$$

where ΔU is the change of system internal energy; ΔKE is the change of system kinetic energy; ΔPE is the change of system potential energy; Q and W are the heat and the work from the outside respectively. For most engineering problems, change of kinetic energy and potential energy can be ignored, and if outside work is taken to zero, then the above equation can be simplified as:

$$\Delta U = Q \tag{6.2}$$

For heat analysis in ANSYS, there are two modules: transient and steady-state. In a transient heat system, internal energy U is changing with time t and the derivative of internal energy to time is the rate of heat transfer from outside q, expressed as the following:

$$q = \mathrm{d}U / \mathrm{d}t \tag{6.3}$$

where q is the rate of heat transfer. For a steady-state heat system, heat input into the system is equal to heat output to outside.

There are three types of heat transfer methods: heat conduction, heat convection and heat radiation. For example, for an SFRC block heated in an electric furnace, usually heat convection and heat radiation need to be considered. Heat convection can further be divided into natural heat convection and forced heat convection. Convection heat can be expressed as:

$$Q = h(T_s - T_b)A \tag{6.4}$$

where h is the convection or film coefficient; T_s is the temperature of solid surface; T_b is the temperature of contacting fluid; A is the contacting area. Under natural convective condition, the convection coefficient h for concrete surface can be taken as 4.74 $\mathrm{W/(m^2 \cdot K)}$ (Zhang et al. 2007).

Thermal conductivity λ can be calculated according to the law of heat conduction or Fourier's law:

$$\lambda = -\phi_q \cdot \mathrm{d}x / \mathrm{d}T \tag{6.5}$$

where ϕ_q is the heat flux (unit: $\mathrm{W/m^2}$); $\mathrm{d}x$ is the distance between the two heat transfer surfaces as shown in Figure 6.5; $\mathrm{d}T$ is the temperature difference between these two surfaces; the negative sign indicates heat moves from higher temperature part to lower temperature part. In this study, the heat flux ϕ_q is calculated as total heat flow divided by the area of the heat transfer surface, the temperature difference $\mathrm{d}T$ is set at 40 °C and the distance $\mathrm{d}x$ is equal to the thickness of the model. This equation is used to calculate the thermal conductivity of the composite material consisting of concrete and steel fibre in this study.

For plain concrete and steel fibre, thermal conductivity and specific heat can be determined according to relevant European Standards. It should be noted thermal properties of concrete may vary depending on density, moisture content, aggregate type, etc. However, since the concrete type is not the main concern in this study, only normal weight dry concrete is considered herein. The thermal conductivity λ_c of plain concrete is determined between the lower and upper limit values as the following (Eurocode 2004):

Upper limit:

$$\lambda_c(T) = 2 - 0.2451(T/100) + 0.0107(T/100)^2 \qquad 20\ ^\circ\mathrm{C} \le T \le 1200\ ^\circ\mathrm{C} \tag{6.6}$$

Lower limit:

$$\lambda_c(T) = 1.36 - 0.136(T/100) + 0.0057(T/100)^2 \qquad 20\ ^\circ\mathrm{C} \le T \le 1200\ ^\circ\mathrm{C} \tag{6.7}$$

where T is the concrete temperature. It is suggested the thermal conductivity of high strength concrete may be higher than that of normal strength concrete and the specific heat c_c of plain concrete is determined from the following (Eurocode 2004):

$$c_c = \begin{cases} 900 & 20\ ^\circ\mathrm{C} \le T \le 100\ ^\circ\mathrm{C} \\ 900 + (T - 100) & 100\ ^\circ\mathrm{C} \le T \le 200\ ^\circ\mathrm{C} \\ 1000 + 0.5 \times (T - 200) & 200\ ^\circ\mathrm{C} \le T \le 400\ ^\circ\mathrm{C} \\ 1100 & 400\ ^\circ\mathrm{C} \le T \le 1200\ ^\circ\mathrm{C} \end{cases} \tag{6.8}$$

For steel fibre, the thermal conductivity λ_s and the specific heat c_s are here taken as the same as common steel and can be calculated as a function of temperature T as the following (Eurocode 2005):

$$\lambda_s(T) = \begin{cases} 54 - 3.33\times10^{-2}\cdot T & 20\ ^\circ\mathrm{C} \le T \le 800\ ^\circ\mathrm{C} \\ 27.3 & 800\ ^\circ\mathrm{C} \le T \le 1200\ ^\circ\mathrm{C} \end{cases} \tag{6.9}$$

$$c_s(T) = \begin{cases} 425 + 7.73\times10^{-1}\cdot T - 1.69\times10^{-3}\cdot T^2 + 2.22\times10^{-6}\cdot T^3 \\ 666 + 13002/(738 - T) \\ 545 + 17820/(T - 731) \\ 650 \end{cases}$$

$$\begin{matrix} 20\ ^\circ\mathrm{C} \le T \le 600\ ^\circ\mathrm{C} \\ 600\ ^\circ\mathrm{C} \le T \le 735\ ^\circ\mathrm{C} \\ 735\ ^\circ\mathrm{C} \le T \le 900\ ^\circ\mathrm{C} \\ 900\ ^\circ\mathrm{C} \le T \le 1200\ ^\circ\mathrm{C} \end{matrix} \tag{6.10}$$

The unit for thermal conductivity is $\mathrm{W/(mK)}$ and for specific heat is $\mathrm{J/(kgK)}$.

In ANSYS, there are several solid element types for thermal analysis such as Solid5, Solid69, Solid70 and Solid87. Solid 70 is an 8-node hexahedral element with one temperature degree of freedom (DOF) on each node and is used for plain concrete, while Solid87 is a 10-node tetrahedral element with one temperature DOF on each node and is selected for SFRC concrete in this study. For fibres, Link33 2-node 3D line element is used. Link33 element has one temperature DOF on each node and has the ability to transfer heat through the shared nodes with concrete elements.

6.3 Model validation

Loading and boundary conditions for calculating thermal conductivity through steady-state heat analysis with ANSYS are exhibited in Figure 6.5. It shows a constant temperature load *T* is acted on the upper surface of the SFRC model, while a convection load with constant air temperature is imposed on its bottom surface. The four side surfaces of the model are applied an insulation boundary condition to prevent heat from moving through these surfaces. When the air temperature is lower than the temperature loaded on the top surface, a steady flow of heat will constantly go into the model from the top surface and go out from the bottom surface. The total amount of the heat flow per unit time reflects the thermal conductivity of the specimen. This method was also adopted by other researchers (Qiu and Liang 2009).

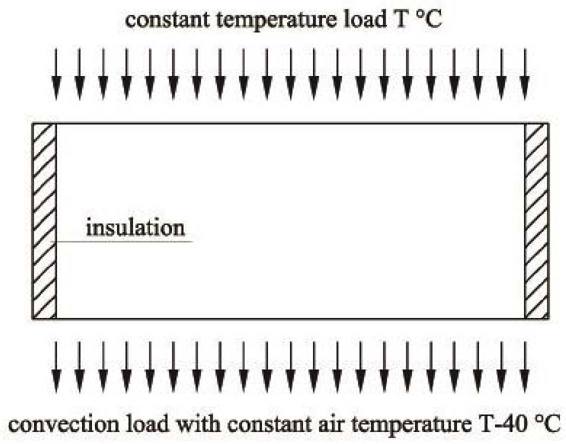

Figure 6.5. Model for calculating thermal conductivity.

An experimental study was conducted on thermal properties of fibre reinforced high-performance self-consolidating concrete (SCC) at elevated temperatures (Khaliq and Kodur 2011). The test setup the authors used to measure thermal conductivity is shown in Figure 6.6. They made comparisons among plain SCC, steel fibre reinforced SCC (SCC-S) and other types of fibre reinforced SCCs. The SCC-S specimen had a size of $60 \times 60 \times 25$ mm and was reinforced with 0.54% steel fibres by volume. The steel fibres were 1.14 mm in equivalent diameter and 38 mm in length. In this simulation for validation, data such as specimen specific heat and thermal conductivity for the plain concrete are chosen from their tests, except that the thermal properties of steel fibres are calculated using the above Eqs. (6.9) and (6.10). The geometric and analytic models for simulation are shown in Figure 6.7.

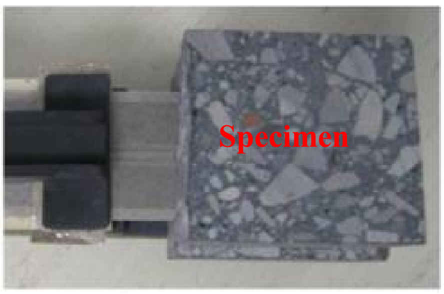

Figure 6.6. Test setup for measuring thermal conductivity (Khaliq and Kodur 2011).

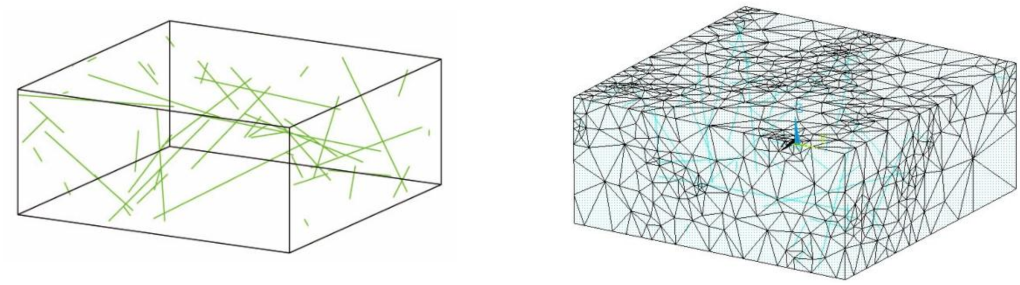

(a) Geometric model (b) Analytic model

Figure 6.7. Geometric and analytic models.

The simulations for calculation of thermal conductivity of the specimen are done under a series of temperature points ranging from 20 °C to 800 °C, which are loaded on the top surface of the model. In each case, air temperature is 40 °C lower than the top surface load as shown in Figure 6.5. It should be noted this temperature difference has little effect on simulation results (Qiu and Liang 2009). Thermal conductivity is an intrinsic property of matter and thus has nothing to do with boundary or loading conditions. Figure 6.8 displays the temperature distribution when the top face load is 800 °C. It can be seen with the presence of steel fibres the fringe line between any two adjacent colour areas becomes irregular, meaning an uneven distribution of thermal gradients. Distribution of heat flux vector at 800 °C is plotted in Figure 6.9. It shows the flux vector becomes denser around the steel fibres, which means the steel fibres have higher thermal conductivity than the concrete. It can also be found where fibres present some flux vectors do not have the direction perpendicular to the two loading surfaces, which indicates the steel fibres locally affect the direction of heat flow. Comparison of thermal conductivity between the test results and the simulation are shown in Figure 6.10 and the values are listed in Table 6.1. It can be seen the simulation results agree well with the test results except at 800 °C. At 800 °C, the abnormity of thermal conductivity of the SCC-S, which is much smaller than that of the SCC, could result from its greater thermal expansion. The tests (Khaliq and Kodur 2011) showed the SCC-S experienced a slightly bigger thermal expansion than the SCC between 20 °C and 600 °C, but the expansion difference increased sharply from 600 °C to 800 °C. The decreased density of the SCC-S led to a great drop of its thermal conductivity. The situation of thermal expansion is unable to be captured in the current model, leading to the discrepancy of thermal conductivity between the tested SCC-S and the simulated SCC-S at 800 °C. Nevertheless, the numerical simulation does reflect two important features of the effect of steel fibres on thermal properties of SFRCs. One is that with the increase of temperature, the thermal conductivity of SFRCs declines. The other is that addition of steel fibres helps enhance the thermal conductivity of the concrete at all temperatures up to 700 °C. At 20 °C the discrepancy between test result and simulation is only 2.3%. Therefore, the model is acceptable when the major concern is the effect of steel fibres but not thermo-chemical change, and the calculated thermal conductivity at room temperature is accurate enough.

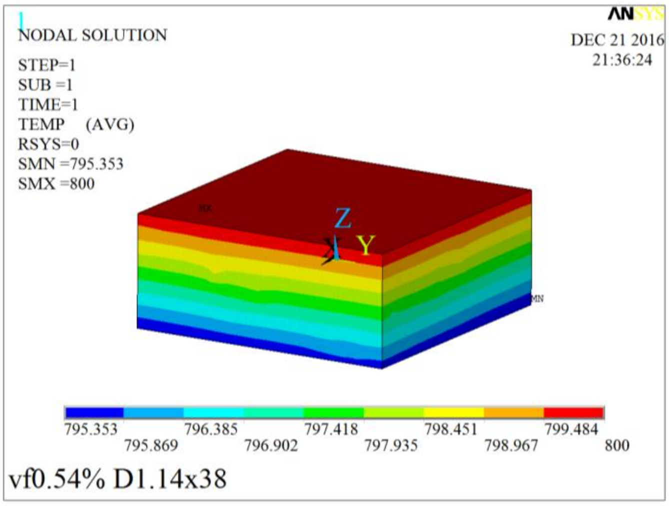

Figure 6.8. Temperature distribution at 800 °C.

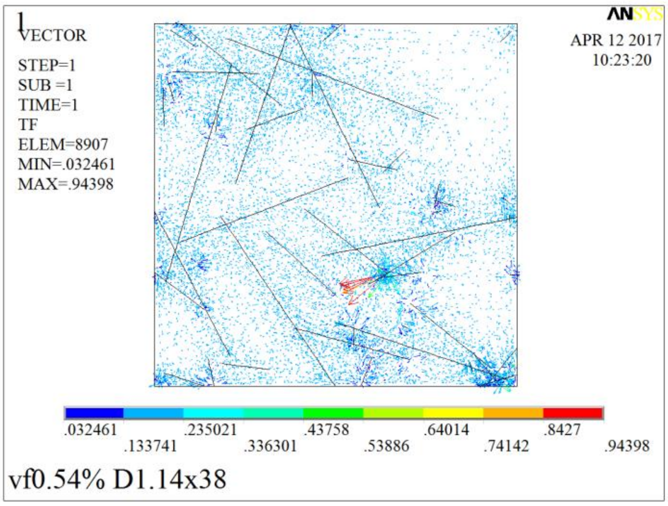

Figure 6.9. Distribution of heat flux vector at 800 °C (bottom view).

Table 6.1. Thermal conductivity under various temperatures (unit: W/(mK))

	Temperature (°C)				
	20	200	400	600	800
SCC	3.288	2.110	1.476	1.476	0.880
SCC-S	3.508	2.356	1.528	1.566	0.608
SCC-S simulation	3.427	2.222	1.568	1.554	0.940
Simulation error (%)	2.3	5.7	2.6	0.8	55.0

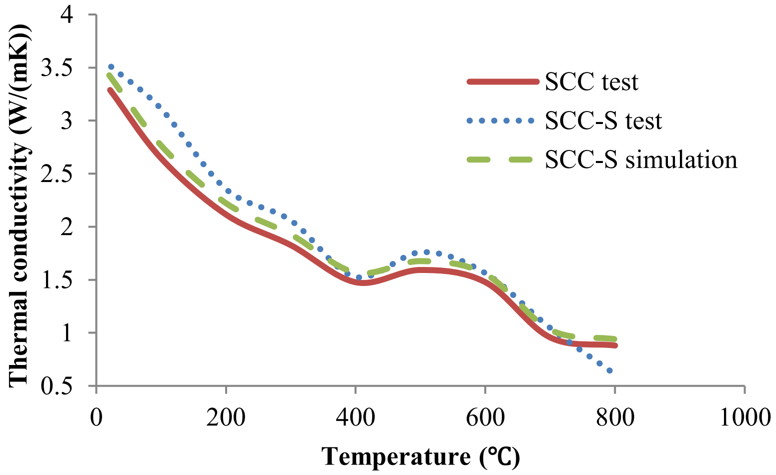

Figure 6.10. Comparison of thermal conductivity between test and simulation.

6.4 Simulation results and discussion

Firstly, the effect of model thickness on simulation outcomes of thermal conductivity is studied in this section. Usually, the thickness should not make difference to outcomes from either tests or simulations when determining the thermal conductivity of a homogeneous material. However, SFRCs are a heterogeneous material and can contain steel fibres with various lengths, which could lead to different results when using different thicknesses. By this, an appropriate thickness is determined for models used for the later simulations. Then, the effect of steel fibre on thermal conductivity of SFRCs under room temperature is numerically investigated. There are two factors to be taken into accounted, i.e. fibre content and fibre diameter. Thermal properties such as thermal conductivity and specific heat for plain concrete and steel fibres at 20 °C and 100 °C are calculated using the above Eqs. (6.6) - (6.10). The European standard (Eurocode 2004) suggests the lower limit of thermal conductivity gives more realistic temperatures for plain concrete structures than the upper limit, which has been derived from tests for steel and concrete composite structures. Therefore, the lower limit of thermal conductivity is used for plain concrete herein. For calculation of thermal conductivity of SFRCs, steady-state heat analyses are implemented in FEA software ANSYS.

6.4.1 Effect of model thicknesses on simulation outcomes of thermal conductivity

In this subsection, nine models with three thicknesses, i.e. 25, 37.5 and 50 mm, and 3 different fibre lengths, i.e. 25, 40 and 55 mm, are simulated. Fibre diameter is 0.7 mm and fibre content is 1% by volume in all models. It should be noted all models are 'cut' from the middle of SFRC blocks. In other words, the two heat-transfer surfaces of the models are not the original surfaces of the matrix block. Loading and boundary conditions for all the models are the same as shown in Figure 6.5. To achieve an almost equal average temperature within models, the constant temperature load for models with thickness 25 mm and 37.5 mm is 25 °C while for that with thickness 50 mm is 26 °C.

The simulation results are plotted in Figure 6.11 and listed in Table 6.2. With increase of model thickness, the fluctuation of all the three curves representing three different fibre lengths is small and each curve tends to level off. It can also be known from Table 6.2, the maximum gap between the models with different thicknesses is 1.54% where the two models have a thickness of 25 mm and 37.5 mm respectively and have fibres in length of 25 mm. The minimum gap is only 0.18% between the two models having a thickness of 37.5 mm and 50 mm respectively and containing fibres in length of 55 mm. In addition, with the increase of thickness the difference of thermal conductivity between the models with different fibre lengths decreases and the maximum gap is 1.69%, 0.52% and 0.08% at the thickness of 25 mm, 37.5 mm and 50 mm respectively. This also indicates fibre length makes little impact on thermal conductivity of SFRCs. Since the difference of simulation results between the models with the thickness of 37.5 mm and 50 mm is less than 0.4% (see Table 6.2), 37.5 mm is adopted as the thickness for all later models which contain fibres in length ranging from 25 mm to 55 mm.

Table 6.2. Thermal conductivity under different model thicknesses and fibre lengths (unit: W/(mK))

Fibre length (mm)	Model thickness (mm)			Gap between 25 and 37.5 mm (%)	Gap between 37.5 and 50 mm (%)
	25	37.5	50		
25	1.508	1.485	1.489	1.54	0.33
40	1.503	1.492	1.488	0.68	0.27
55	1.482	1.491	1.488	0.57	0.18
Maximum gap (%)	1.69	0.52	0.08		

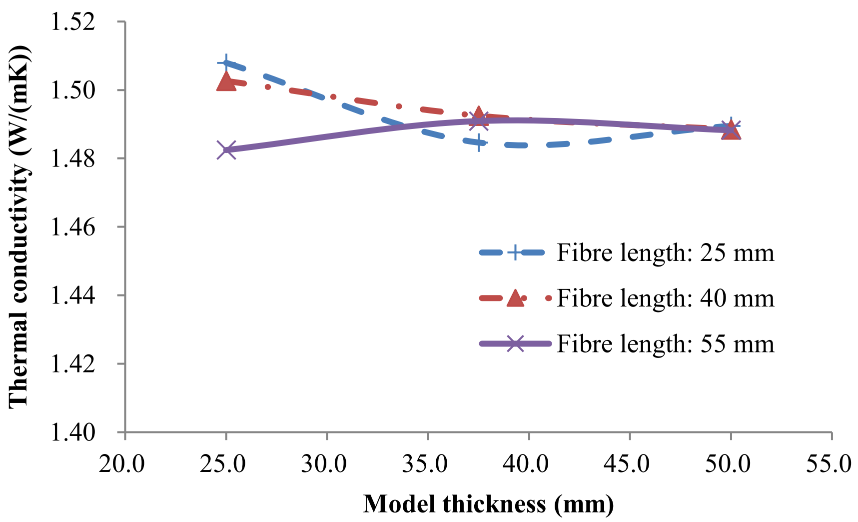

Figure 6.11. Curves of thermal conductivity versus model thickness.

6.4.2 Effect of fibre content on thermal conductivity

Totally four models are prepared with different fibre contents, i.e. plain, 0.5%, 1% and 2% by volume, and they all have a size of $50 \times 50 \times 37.5$ mm. All fibres are 0.9 mm in diameter and 40 mm in length. For the model with 2% steel fibres by volume, there are 34,578 solid elements for the concrete and 2,126 line elements for the fibres. Loading and boundary conditions for all the models are as the same as shown in Figure 6.5 with *T* being 25 °C.

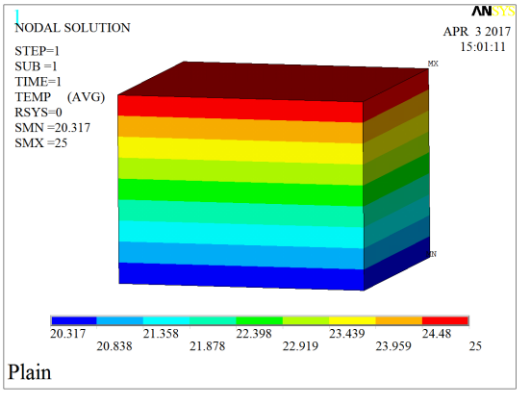

(a) Plain

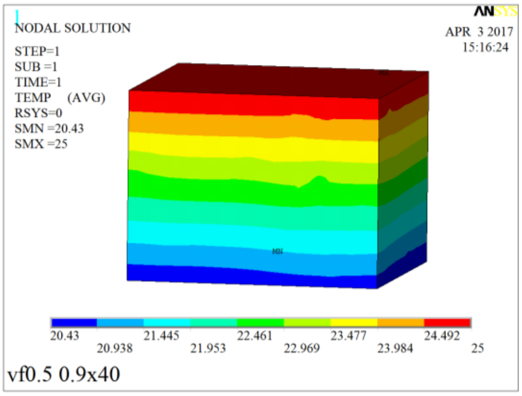

(b) 0.5% steel fibre

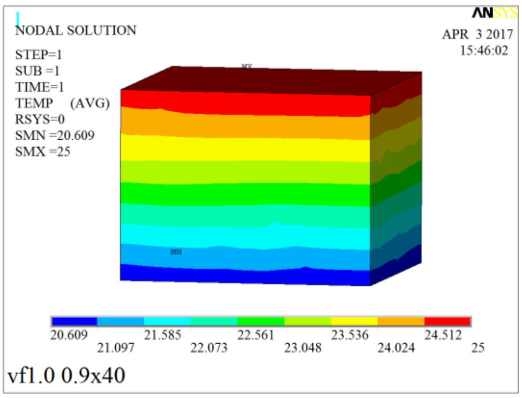

(c) 1% steel fibre

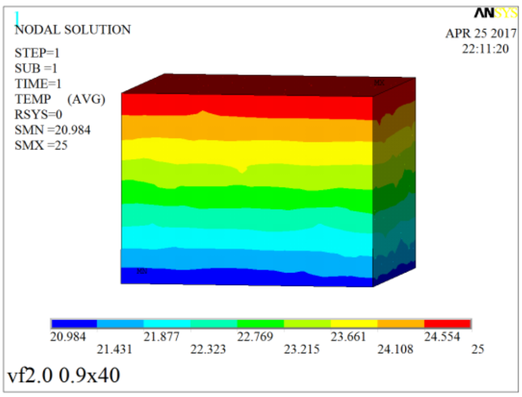

(d) 2% steel fibre

Figure 6.12. Temperature distribution of models with different fibre contents.

Temperature distribution for the four models with different fibre contents is displayed in Figure 6.12. It can be seen with the increase of fibre content, the minimum temperature which is on the bottom surfaces increases. Usually, higher minimum temperature on the heat-output surfaces means smaller temperature difference between the two heat-transfer surfaces and higher thermal conductivity. The irregular temperature distribution on the surfaces indicates ends of steel fibres present there.

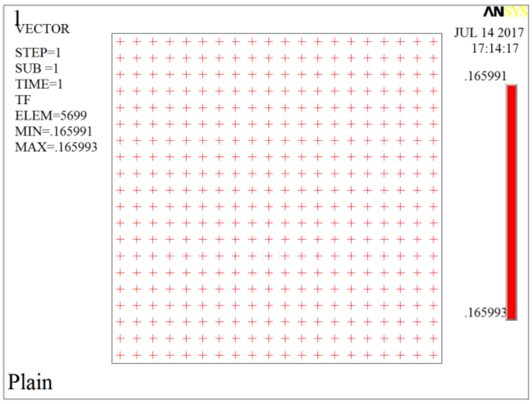

(a) Plain

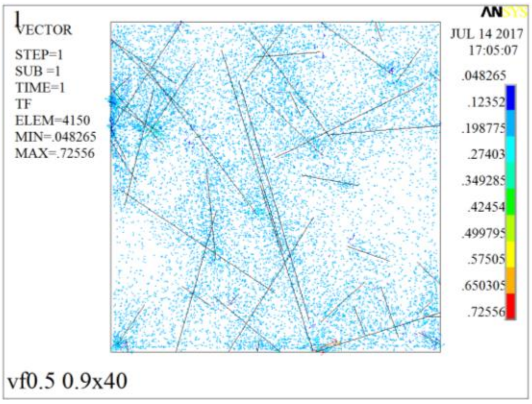

(b) 0.5% steel fibre

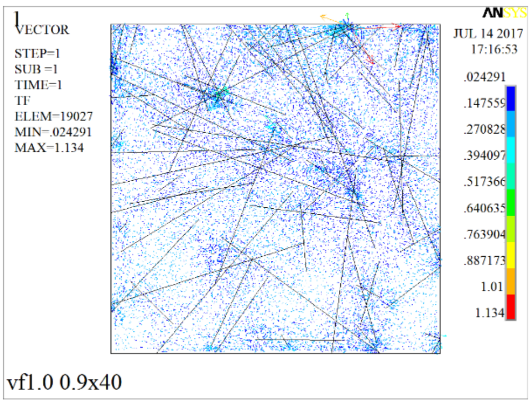

(c) 1% steel fibre

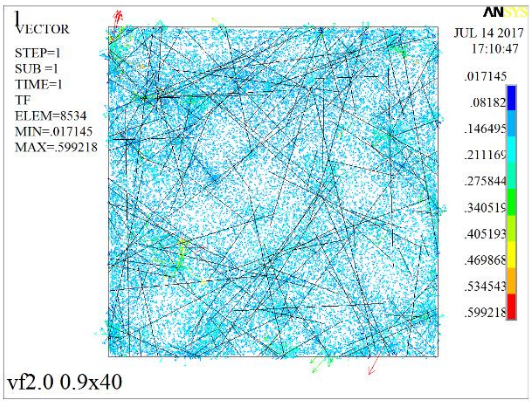

(d) 2% steel fibre

Figure 6.13. Heat flux vector distribution of models with different fibre contents (bottom view).

Figure 6.13 illustrates heat flux vector distribution of the four models (viewed from the bottom). The plain model has an almost completely even flux distribution. It can be seen the highest flux vector for each SFRC case presents close to the heat-isolation side surfaces where a few fibres gather. Steel fibres have much higher thermal conductivity than concrete and with greater fibre content more fibres likely gather, which usually leads to higher local heat flux. However, the model with 1% rather than 2% fibres by volume has the maximum highest flux vector due to the uneven fibre distribution as displayed in Figure 6.13(c), where much more fibres are located in the upper half section than in the lower half section. Figure 6.13 also shows with increase of fibre content, the minimum lowest flux vector decreases. This could be attributed to the fact that all the models have the identical loading and boundary conditions, and therefore for the model with more fibres more heat is transferred around the fibres but less through plain concrete areas from the heat-input surface to the heat-output surface.

Figure 6.14 shows the relationship between thermal conductivity and fibre content. It can be seen the thermal conductivity grows almost linearly with the rise of the fibre content. Compared to the plain concrete, the 2% steel fibres reinforced concrete increases by 26% in thermal conductivity. The relationship between thermal conductivity and fibre content can be expressed as the following equation:

$$\lambda = \lambda_0 + 17.2V_f \qquad (6.11)$$

where λ_0 is the thermal conductivity of the plain concrete; V_f is the fibre content by volume.

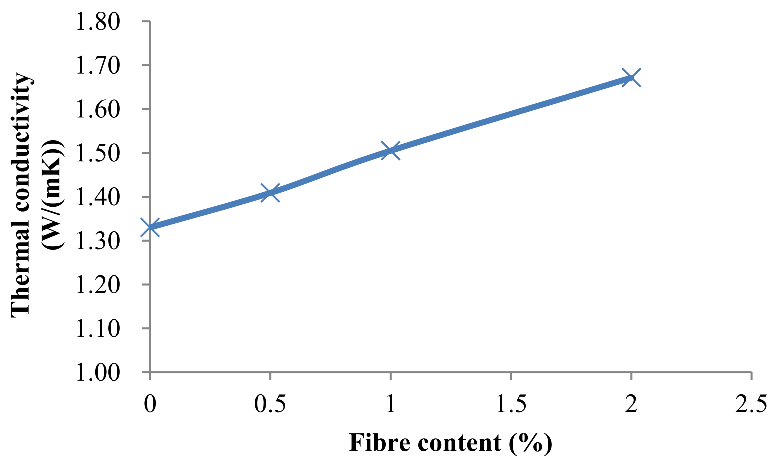

Figure 6.14. Thermal conductivity versus fibre content.

6.4.3 Effect of fibre diameter on thermal conductivity

As discussed above, fibre length has little effect on thermal conductivity especially when the model thickness is great enough, e.g. 37.5 mm. In this subsection, the effect of fibre diameter is investigated. Totally four models are prepared with different fibre diameters, i.e. 0.5, 0.7, 0.9 and 1.1 mm, and they have a size of $50 \times 50 \times 37.5$ mm. All models are 'cut' from the middle of SFRC blocks that have a fibre content of 1% by volume and fibres have a length of 40 mm. For the model with 0.5 mm fibres, there are 48,398 solid elements for concrete and 3,411 line elements for fibres. Loading and boundary conditions for all the models are shown in Figure 6.5 with *T* being 25 °C.

For the four models with fibre diameters of 0.5, 0.7, 0.9 and 1.1 mm, the average temperature on their bottom surfaces is calculated as 20.77, 20.78, 20.81 and 20.71 °C respectively. Usually the higher this average temperature, the greater the thermal conductivity. The temperature distribution of the four models is shown in Figure 6.15. It can be seen all models almost experience the same lowest temperature. That the lowest temperature of the model with 0.5 mm fibres is a little higher than the other models indicates this model has the evenest temperature distribution on its bottom surface. All the four models experience almost the same irregularity of temperature distribution on their side surfaces.

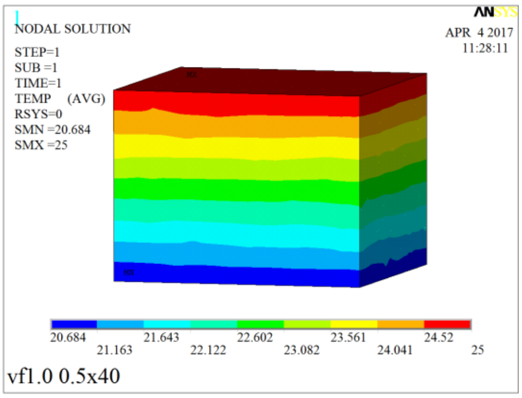

(a) 0.5 mm

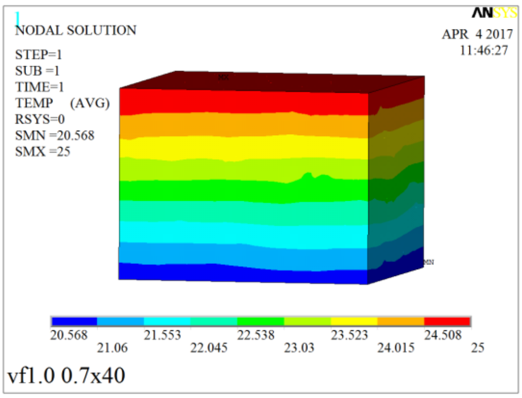

(b) 0.7 mm

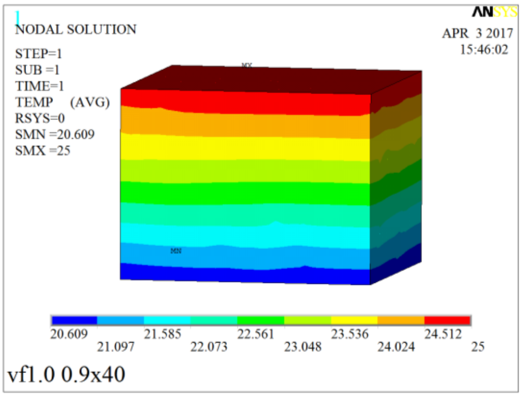

(c) 0.9 mm

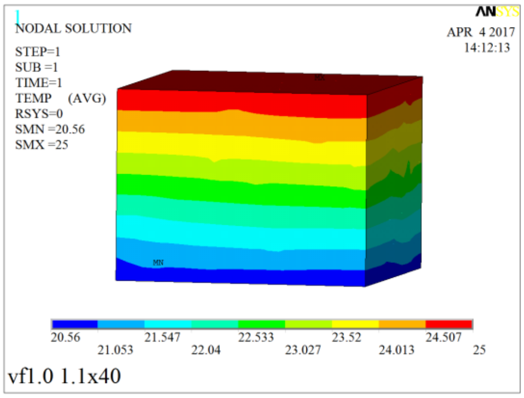

(d) 1.1 mm

Figure 6.15. Temperature distribution of models with different fibre diameters.

For the four models with fibre diameters of 0.5, 0.7, 0.9 and 1.1 mm, the total heat flow from the upper surface to the bottom surface is calculated as 0.42012, 0.42024, 0.42043 and 0.41957 W, respectively. Heat flux vector distribution of the four models is shown in Figure 6.16 (viewed from bottom). The model with 0.9 mm fibres has the minimum lowest flux vector, while it has the greatest total heat flow. It means this model experiences the most uneven flux distribution and steel fibres in this model play a bigger role in transferring heat than in the other three models.

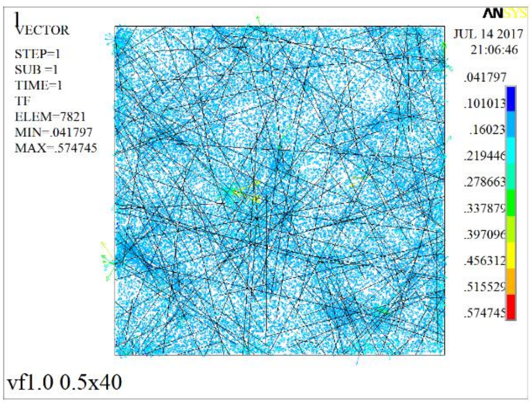

(a) 0.5 mm

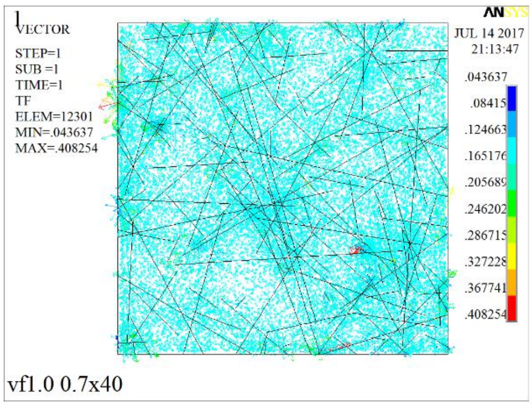

(b) 0.7 mm

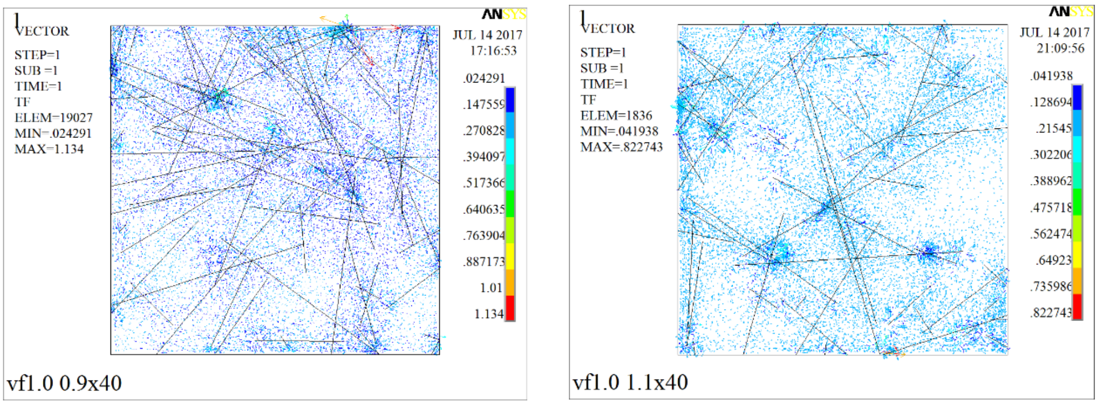

(c) 0.9 mm (d) 1.1 mm

Figure 6.16. Heat flux vector distribution of models with different fibre diameters (bottom view).

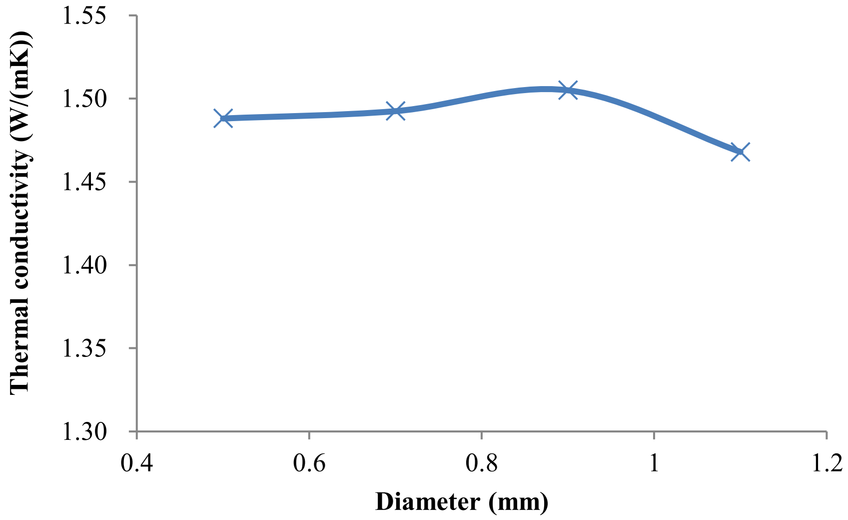

Figure 6.17. Thermal conductivity versus fibre diameter.

Figure 6.17 plots the relationship between thermal conductivity and fibre diameter. With the increase of fibre diameter, the thermal conductivity rises up to 1.505 W/(mK) at 0.9 mm but then decreases. The maximum difference among these four models is 0.037 W/(mK) or 2.5% between the models with 0.9 mm and 1.1 mm fibres. The reason could be that there are actually two contradictory factors, i.e. fibre diameter and fibre distribution density. While big fibre diameter is beneficial to heat conduction along the fibre, relatively low fibre distribution density weakens heat transfer between the two component materials.

6.4.4 Difference of thermal conductivity between edge and middle sections

This subsection is to investigate thermal conductivity of different parts of an SFRC block. Fibre distribution near the boundaries of the SFRC block is different from the interior, so thermal conductivity of these two parts of the SFRC block could be different with each other. As shown in Figure 2.21, models cut from an SFRC block can be divided into two categories according to their position in the block, i.e. middle-section model with both heat-transfer surfaces cut and edge-section model with only one of its heat-transfer surfaces cut. All models simulated in this subsection have the same parameters as in the above subsection 6.4.2.

Comparison between thermal conductivity of these two kinds of models is shown in Figure 6.18. It can be seen except the plain concrete model, all the edge-section models have lower thermal conductivity than their corresponding middle-section models. With different fibre contents, the difference of thermal conductivity between edge-section models and middle-section models is plotted in Figure 6.19. With the increase of fibre content, the difference increases by up to 8.5% for the model with a fibre content of 2% by volume. This indicates when preparing for testing of thermal conductivity, specimens cut from SFRC blocks should be consistently selected.

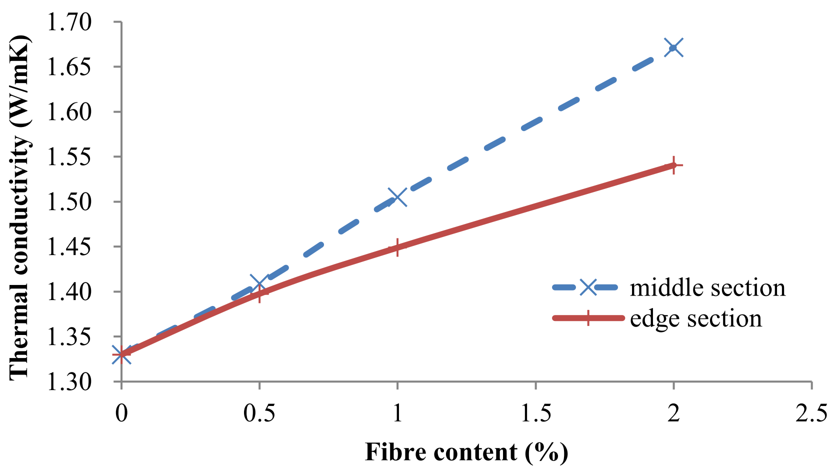

Figure 6.18. Comparison between thermal conductivity of middle-section and edge-section model.

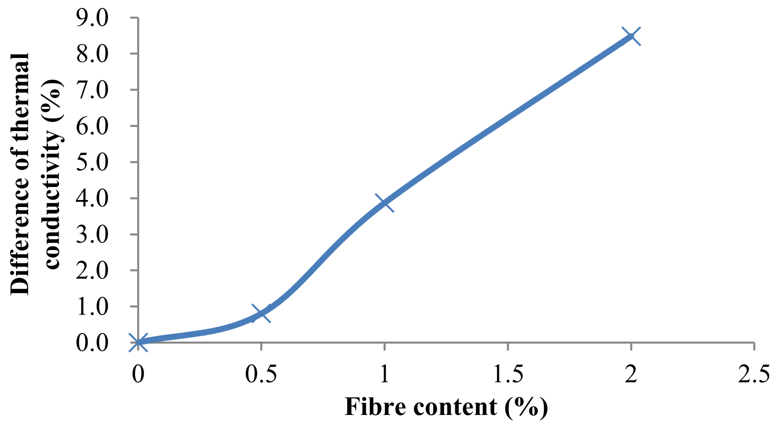

Figure 6.19. Difference of thermal conductivity versus fibre content.

6.5 Summary

To investigate thermal properties of SFRCs (UHPCs), a meso-scale model is developed, treating SFRCs as a composite material of concrete and steel fibre. Delaunay triangulation is employed to generate the mesh for the composite material so that the two constituent materials can work together with each other appropriately.

The study reveals that presence of steel fibres has an obvious impact on the distribution of temperature and heat flux vector. With the increase of model thickness, the simulation outcome of thermal conductivity converges rapidly. Overall, model thickness has an insignificant effect on the simulation outcomes of thermal conductivity for all the models with different fibre lengths ranging from 25 mm to 55 mm. It is found with the increase of steel fibres, the thermal conductivity of SFRCs improves noticeably. As for effect of aspect ratio of steel fibres, fibre length makes a negligible impact on thermal conductivity of SFRCs, while fibre diameter affects this thermal property marginally. The model with fibres of 0.9 mm in diameter has the highest thermal conductivity among all the models with different fibre diameters but the same fibre content. The reason could be this model has fibres with a relatively large diameter which benefits heat flow along the fibres and at the same time relatively dense fibre distribution which boosts heat transfer between fibres and concrete. It is also found thermal conductivity of an edge section of SFRC blocks is lower than that of a middle section, and the difference grows with increase of fibre content.

The current model does not take into account moisture content and thermochemical behaviour that could affect thermal properties of SFRCs. Also, it is unable to consider variations of density, moisture content and porosity of SFRCs due to incorporation of steel fibre. These could be addressed in the future study.

CHAPTER 7

NUMERICAL STUDY OF MECHANICAL PROPERTIES OF SFRC/UHPC USING MESO-SCALE MODELLING

7 NUMERICAL STUDY OF MECHANICAL PROPERTIES OF SFRC/UHPC USING MESO-SCALE MODELLING

Based on Delaunay triangulation, a 3D meso-scale model is successfully developed and verified. This approach modelling fibre and concrete separately and linking them with slide line contact has the capability to truly reflect the interfacial behaviour of fibre and mortar, and thus achieve high fidelity of numerical simulations. However, meso-scale modelling usually means tremendous complexity and long computational time. This paper proposes a model to achieve relatively high computation efficiency, as well as accuracy. Besides, the model has the potential to deal with small specimens cut from steel fibre reinforced concrete (SFRC) blocks.

7.1 Model validation

7.1.1 Material model, contact algorism and material properties

The hydrocode LS-DYNA is a simulation software package capable of dealing with both dynamic and static problems and is applied to all the calculations in this study. The K&C model in LS-DYNA can properly model key concrete behaviours such as post-peak softening, shear dilation and strain rate (Wu et al. 2014; Wu et al. 2012). Most importantly, this model can capture implicit confinement of reinforcement which is essential to represent fibre effect on SFRC, and thus is adopted for mortar in this research. For steel fibre, the Mat_Plastic_Kinematic material model is used. This model has the ability to simulate isotropic and kinematic hardening plasticity with the option of including rate effects. It is a very cost-effective model and is available for beam (including truss), shell, and solid elements (LS-DYNA 2013). Other materials such as plywood used in splitting tension simulation will be discussed in the related subsections.

Slide line contact or the keyword *contact_1D in LS-DYNA is chosen for contact algorism between fibres and concrete. This algorism allows a string of fibre nodes (or slave nodes) slide along a string of mortar nodes (or master nodes). In this study fibre nodes and mortar nodes coincide with each other at every fibre node location. As mentioned above, fibre pull-out process can be divided into three different stages, i.e. complete bond, partial bond and complete debond. The contact algorism in LS-DYNA can be expressed as the relationship between bond shear stress and slip as shown in Figure 7.1 where there are two portions. It needs to be noted complete bond and partial bond stages are simplified as the linear portion of the curve in Figure 7.1 while the softening portion corresponds to the stage in which fibre and concrete are completely debonded, and interfacial force is provided purely by friction.

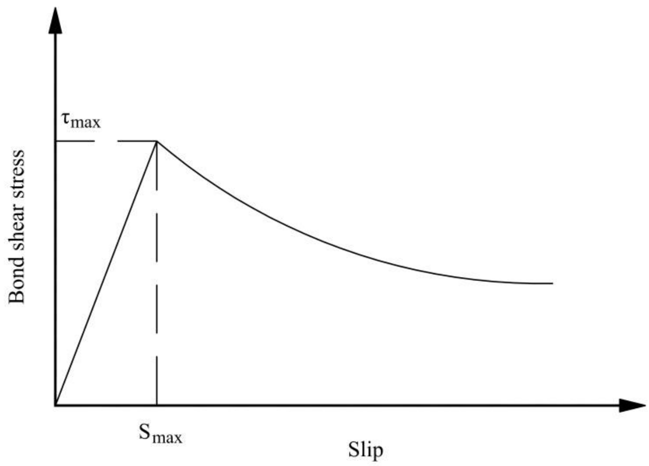

Figure 7.1. Bond shear stress versus slip.

At time n+1, the shear force on the interface can be given as follows:

$$f_{n+1} = \min(f_n - GB \cdot A_s \cdot \Delta u, GB \cdot A_s \cdot \Delta u_{max}) \quad (7.1)$$

$$u_{max} = S_{max} \cdot e^{-EXP \cdot D} \quad (7.2)$$

where *GB* is the bond shear modulus; A_s is the bond area of per unit length and $A_s = 2\pi R_e$; R_e is the outer radius of fibre; *u* is slip strain per unit length; u_{max} is the maximum slip strain; S_{max} is the maximum elastic slip strain; *EXP* is the exponent in damage curve; *D* is the damage parameter and is given as:

$$D_{n+1} = D_n + \Delta u \quad (7.3)$$

Table 7.1. Properties of steel fibre

Diameter (mm)	Density (kg/m^3)	Modulus of Elasticity (MPa)	Poisson's Ratio	Yield Stress (MPa)
0.9	7,800	2.1×10^5	0.28	1,480

Table 7.2. Constituents of SFRC

Ingredients	Weight (kg/m^3)
42.5 SR Cement	750
River sand	1,030
Silica fume	225
Silica flour	190
Superplasticizer	16
Water	190
Water/Binder	16.3%
Nano Al_2O_3	21.7
1% TF	79
2% TF	158

Table 7.3 Parameters of bond-slip contact

GB (GPa)	S_{max}	*EXP*
2.4	3×10^{-3}	0.2

Properties of steel fibres used in this paper are listed in Table 7.1. For subsections 7.1.2, 7.1.3, 7.1.4, 7.2.1.1 and 7.2.2.1, the ingredients of the SFRC with high strength are shown in Table 7.2. To define the contact between fibres and mortar, three parameters need to be determined, i.e. *GB*, S_{max} , *EXP* and they are listed in Table 7.3 for contact used in subsections 7.1.2 to 7.1.4. For subsection 7.1.5, properties of concrete and contact between fibre and concrete are reported in that subsection. It is worth noting that though in the current physical models all fibres are straight, some other types of fibres with different fibre shapes can still be properly modelled by using appropriate contact parameters. Prior to the determination, various lengths of fibre element were attempted to obtain a converged result. In this study, the average fibre element length is set at around 1.5 mm for models with tetrahedral elements and 2 mm for models with hexahedral elements. It is a requirement for the bond-slip contact algorism in LS-DYNA that there should be at least three nodes in a single contact node set, e.g. a string of nodes for a fibre. In this study fibres with length less than 3 mm are deleted because too short fibres could result in computing difficulty and they only account for less than 1% (in most cases 0.5%) of the total fibres.

7.1.2 Single fibre pull-out

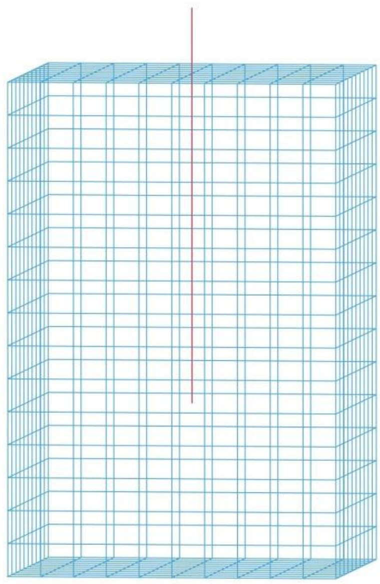

Figure 7.2. Simulation of single fibre pull-out.

The analytical model shown in Figure 7.2 has a mortar base with a dimension of $20\times20\times30$ mm, and the fibre has a total length of 24 mm with 20 mm embedded in the base. Both the mortar and the fibre have an element size of 2 mm and totally there are 1,500 solid elements for the mortar and 12 beam elements for the fibre. Fibre properties, SFRC ingredients and parameters of bond-slip contact are listed in Table 7.1, Table 7.2 and Table 7.3, respectively. The curve of pull-out force versus slip is depicted in Figure 7.3 against the test result from (Tuyan and Yazıcı 2012). It can be seen the linear portions of the simulation and the test result agree with each other well, while the softening portion of the simulation shows some difference with the test result. This is because the contact algorism adopted in LS-DYNA assumes an exponential curve for the softening portion while the test result is not so. This means reasonable accuracy can be achieved using the bond-slip contact algorism before cracks within the matrix form and spread but some error can occur afterwards. From Figure 7.3, it can be seen the simulation shows similar pull-out work to the test.

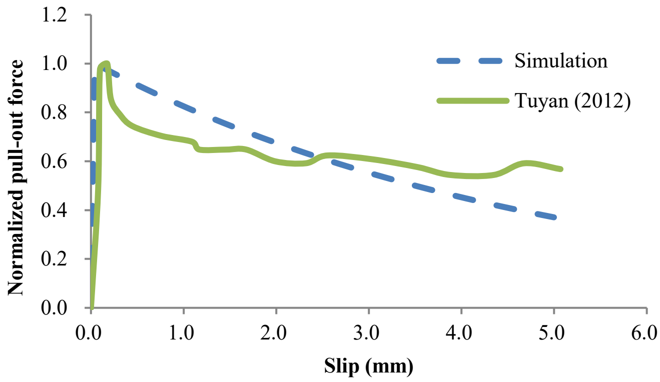

Figure 7.3. Pull-out force versus slip.

7.1.3 Quasi-static uniaxial compression

Totally three models with different fibre dosages, i.e., 0.0%, 1.0%, 2.0% by volume respectively, are simulated and results are compared with tests'. The model is a 100 mm cube under uniaxial compression. The analytical model of the sample with 1.0% fibre volume fraction is displayed in Figure 7.4. There are 97 and 184 fibres in the models with 1.0% and 2.0% fibres by volume respectively. The loading steel plate is 60 mm in length, 60 mm in width and 30 mm in height. Elastic material model is applied to the steel plate with solid element type. It has a density of $7{,}830\ \text{kg/m}^3$, modulus of elasticity of 2.07×10^5 MPa and Poisson's ratio of 0.3. The model with 2.0% fibres by volume has 50,541 mortar solid elements and 3,510 fibre truss elements. An automatic surface to surface contact is considered between the loading steel and the concrete.

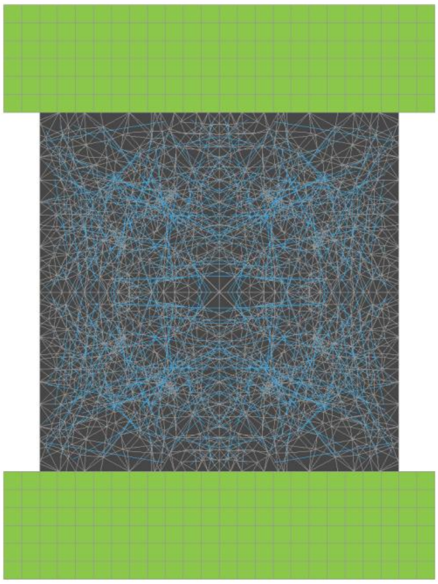

Figure 7.4. Analytical model of 1.0% fibre SFRC.

Uniaxial compressive tests were conducted so that comparison can be made and reliability of the model can be checked. Ingredients of the mortar mixture are shown in Table 7.2, where TF denotes twisted fibre with a diameter of 0.4 mm and length of 35 mm and its other properties are listed in Table 7.1. Properties of bond-slip contact between fibres and cement paste are shown in Table 7.3. To prepare the samples, type SR Sulphate Resisting cement was adopted, and small aggregates were made up of river sand with size ranging from 0.16 mm to 2.5 mm. To achieve high performance, silica materials and Nano-Al_2O_3 particles are also added to the mixture.

Curves of compressive stress versus strain from both the tests and the numerical simulations are shown in Figure 7.5, and it can be seen the simulation results agree well with the test results. Both the simulation and tests indicate with higher fibre contents, the ultimate compressive strength of SFRC increases so does the corresponding strain, which means the improvement of ductility and toughness.

7.1.4 Flexural tension simulation

A typical test setup conforming to Chinese national standards GB/T 50081-2002 is shown in Figure 7.6. The full SFRC model is a $100\times100\times400$ mm prism, but only a $50\times100\times200$ mm prism for concrete with fibres or a $50\times100\times400$ mm prism for plain concrete is modelled. The distance between the two supporting rollers is 300 mm, and that between the two loading rollers is 100 mm. Reinforced with 1% volume fraction steel fibres means there are totally 1,572 fibres within the model. Fibre properties, SFRC ingredients and parameters of bond-slip contact are listed in Table 7.1, Table 7.2 and Table 7.3, respectively. Both the steel loading plate and the steel rollers have the identical properties with the steel plate used in subsection 7.1.3. However, the loading plate is treated as a rigid material while the elastic material model is applied to the rollers. The FEA model with fibres is displayed in Figure 7.7. There are totally 133,637 tetrahedral elements for the concrete matrix, 7,892 truss elements for the fibres, 2,808 solid elements for the rollers and 300 solid elements for the loading plate. For the plain concrete model, an element size of 5 mm is applied to the concrete. Automatic surface to surface contact is considered between the loading plate and the steel rollers and between the steel rollers and the concrete.

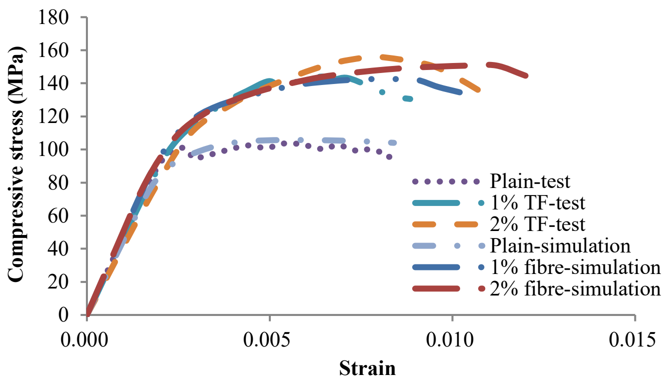

Figure 7.5. Compressive stress versus strain.

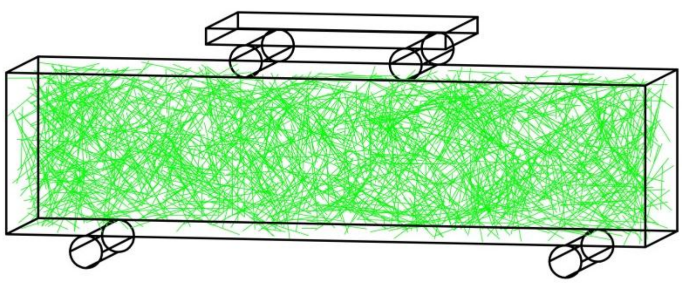

Figure 7.6. Geometric model for flexural tension simulation.

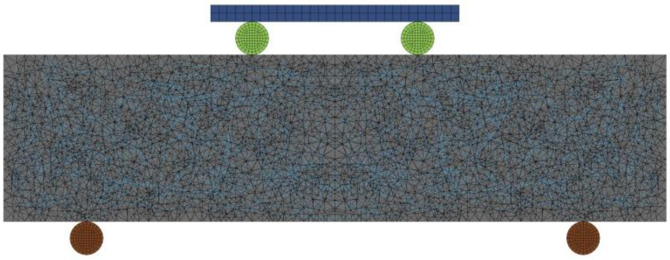

Figure 7.7. Analytical model for flexural tension simulation.

Comparison between numerical simulation and test results is shown in Figure 7.8, where TF denotes twisted fibre. It can be seen the simulation well predicts the peak load and the ductility of SFRC reinforced with 1% fibres by volume. By contrast, the plain specimen shows very brittle behaviour, as well as low peak load at only 35 kN.

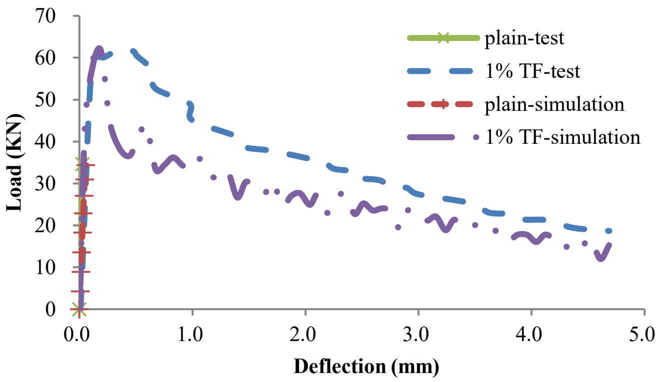

Figure 7.8. Load versus mid-span deflection.

7.1.5 Splitting tension simulation

In this subsection, a model of a 150 mm SFRC cube reinforced with 1% steel fibres by volume is prepared and analysed, and numerical results are compared with test results from (Gao et al. 2004; Gao et al. 2005). Within the full model, there are totally 1,326 fibres with a diameter of 0.9 mm and a length of 40 mm. The geometric model is displayed in Figure 7.9. The loading setup shown in Figure 7.9 complies with Chinese national standards GB/T 50081-2002. Two arc-shaped steel plates with the same depth as the model are symmetrically placed on the bottom and top of the model cushioned by two pieces of plywood. Properties of the steel plate are the same as used for uniaxial compression in subsection 7.1.3. Plastic kinematic material model is adopted for the plywood and its properties are listed in Table 7.4. The concrete matrix has a compressive strength of 60 MPa. The fibres are assumed to have the same properties as listed in Table 7.1. For the slide line contact, the three parameters *GB*, S_{max} and *EXP* are listed in Table 7.5. Material model and element type for concrete and fibre remain the same as in the previous subsection.

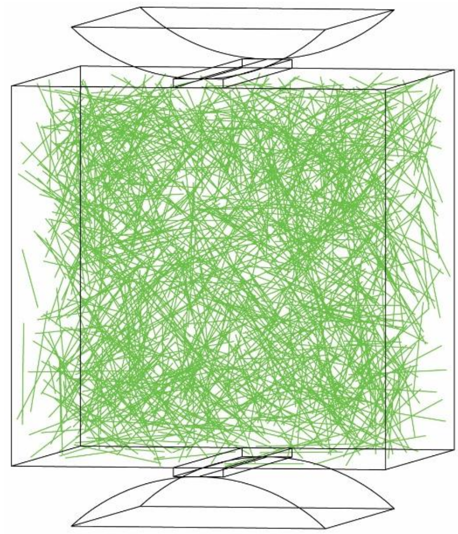

Figure 7.9. Geometric model for splitting tension simulation.

Table 7.4. Properties of plywood

Density (kg/m^3)	Modulus of Elasticity (MPa)	Tangent modulus (MPa)	Poisson's Ratio	Yield Stress (MPa)
600	6,000	1,000	0.3	30

Table 7.5. Parameters of bond-slip contact for splitting tension

GB (GPa)	S_{max}	*EXP*
1.8	3×10^{-3}	0.2

The analytical model shown in Figure 7.10 has 99,597 tetrahedral elements for the concrete, 5,337 truss elements for the fibres, 760 solid elements for the plywood and 1,900 solid elements for the loading steel plate. It should be noted only the middle part of the loading steel is modelled for simplification purpose and this doesn't incur any difference for the simulation result since a rigid material model is used for the loading steel. Automatic surface to surface contact is considered between the loading steel and the plywood and between the plywood and the concrete.

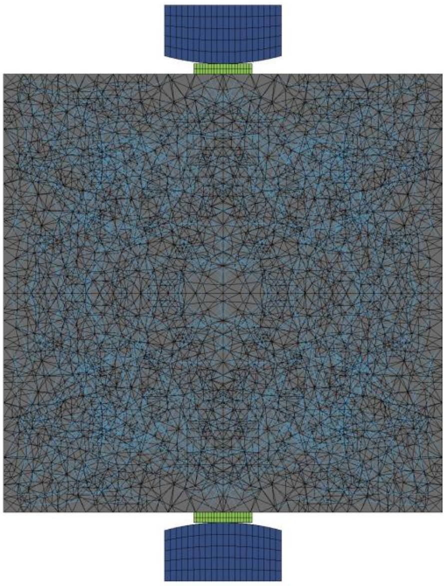

Figure 7.10. Analytical model for splitting tension simulation.

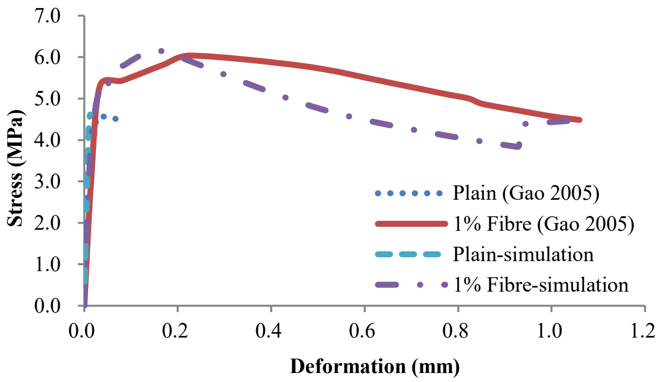

Figure 7.11. Split stress versus deformation.

Simulation results and test results are shown in Figure 7.11. It can be seen for both plain concrete and fibre reinforced concrete, the simulation results agree quite well with the test results. The curves show with the addition of 1% volume fraction steel fibres concrete displays higher strength and much better ductility than its plain counterpart. For plain concrete, the ultimate stress is 4.62 MPa calculated from simulation and 4.53 MPa obtained by experiment, while deformation is smaller than 0.1 mm. For concrete with 1%

steel fibre by volume, the ultimate stress is 6.22 MPa calculated from simulation and 6.04 MPa obtained by experiment, while deformation is larger than 1 mm.

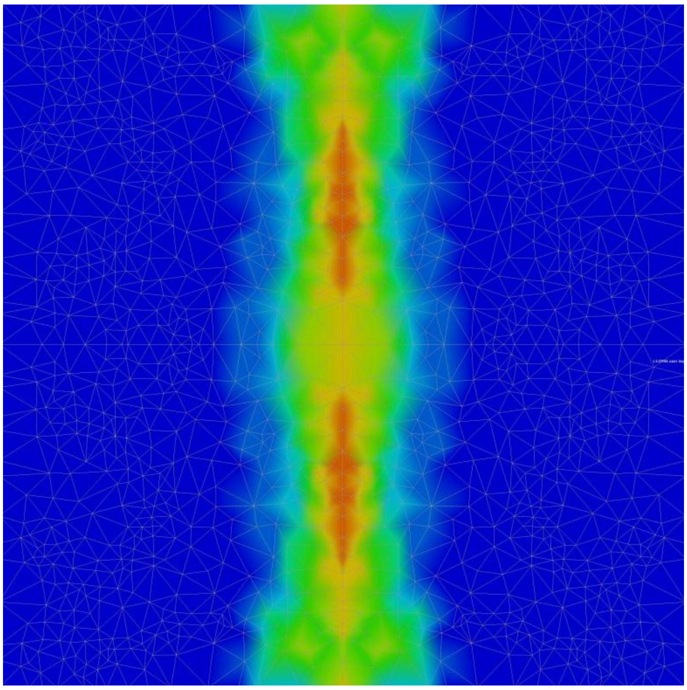

(a) Step 24/100

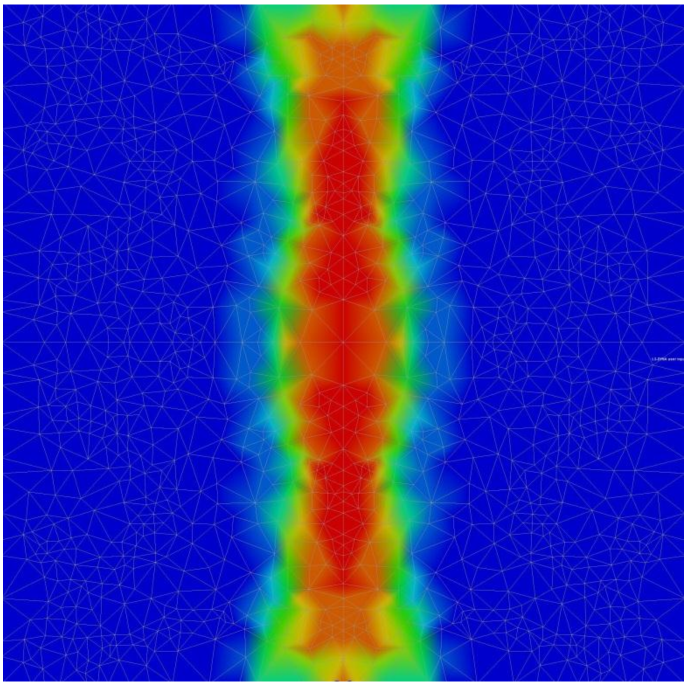

(b) Step 30/100

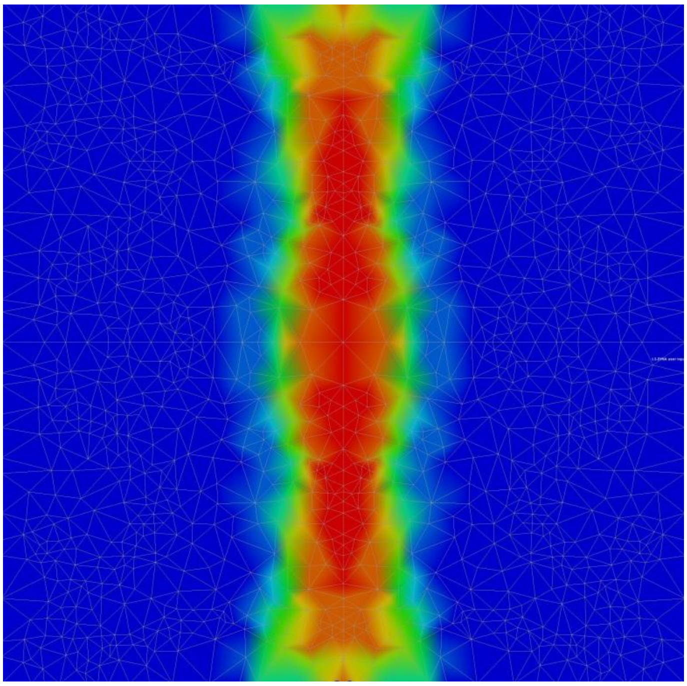

(c) Step 51/100

Figure 7.12. Damage development along loading axis.

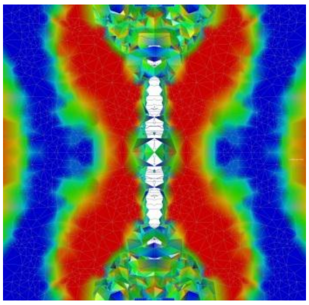

(a) Simulation

(b) test (Gao et al. 2004)

Figure 7.13. Comparison of damage mode between simulation and test.

Denneman et al. (Denneman et al. 2011) stated conventional experiment approaches apply Timoshenko and Goodier equations to the calculation of tensile strength and therefore assumed fracture mode could be rupture that begins from the centre of the specimen and then extends in the direction to the loading surfaces. The current simulation agrees well with this assumption. Figure 7.12 shows damage development along the loading axis where fringed levels represent scaled damage measure designed for the K&C

model in LS-DYNA. Scaled damage measure ranging from 0 to 1 means the material transitions from the yield failure surface to the maximum failure surface, and from 1 to 2 indicates the material moves from the maximum failure surface to the residual failure surface. It can be clearly seen damage starts from the centre of the model and then propagates vertically towards the top and bottom surfaces where the load is imposed. Eventually, rupture happens in the middle of the loading axis followed by crush around the loading strips. A comparison of damage modes between the current simulation and the test conducted by Gao et al. (Gao et al. 2004) is displayed in Figure 7.13. The test result also shows a rupture in the middle of the loading axis of the specimen and a crush on its top.

7.2 Effect of steel fibre on properties of SFRCs

In this section, how steel fibres including fibre content and aspect ratio affect properties of SFRCs will be investigated based on the validated 3D models. Fibre contents are divided into four groups: 0, 0.5%, 1% and 2% and fibres have a diameter of 0.9 mm and a length of 40 mm, while studies on fibre aspect ratio involve four different fibre lengths: 30, 40, 50 and 60 mm with all fibres having an identical diameter of 0.9 mm (i.e. aspect ratio of 33.3, 44.4, 55.6, and 66.7).

7.2.1 Study on effect of fibre content on properties of SFRCs

As shown in Figure 7.14, four 100 mm cubic models with various fibre contents, i.e. 0, 0.5%, 1% and 2% are numerically studied to investigate the relationship between fibre contents and SFRC properties such as compressive strength and splitting tensile strength. All fibres have a diameter of 0.9 mm and length of 40 mm, and other parameters of fibre are listed in Table 7.1.

7.2.1.1 Compressive strength

In this subsection, high strength concrete has the ingredients as reported in Table 7.2 and parameters of bond-slip contact are listed in Table 7.3. Under different fibre contents, curves of compressive strength versus strain are plotted in Figure 7.15 and the relationship between compressive strength and fibre content is displayed in Figure 7.16. As expected, compressive strengths of the model with steel fibres are much higher than the plain model, and the larger fibre contents the higher peak strength and peak strain. That also means toughness of models improves greatly with the increase of the addition of steel fibres. For models with various fibre contents, peak compressive stress and peak strain are listed in Table 7.6.

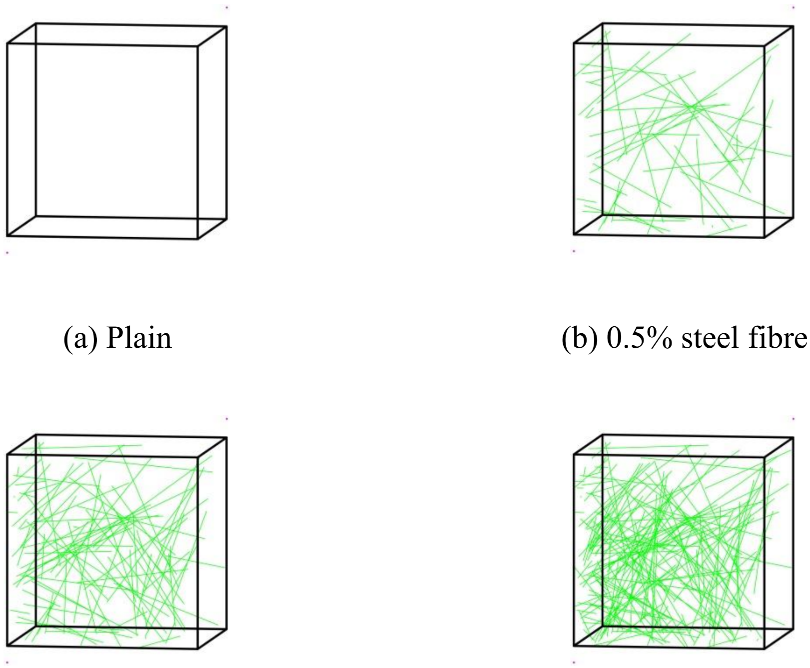

(a) Plain

(b) 0.5% steel fibre

(c) 1% steel fibre

(d) 2% steel fibre

Figure 7.14. Geometric models with different fibre contents.

Table 7.6. Peak compressive stress and peak strain under various fibre contents

	Fibre content (by volume)			
	Plain	0.5%	1%	2%
Peak strength (MPa)	105.7	138.8	142.6	150.8
Peak strain (10^{-3})	5.4	6.6	8.4	11.2

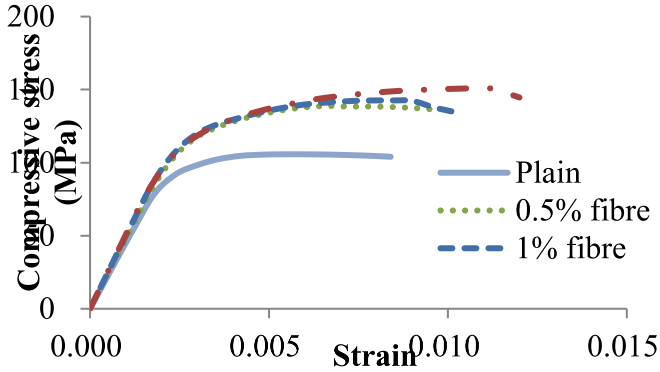

Figure 7.15. Compressive strength versus strain under different fibre contents.

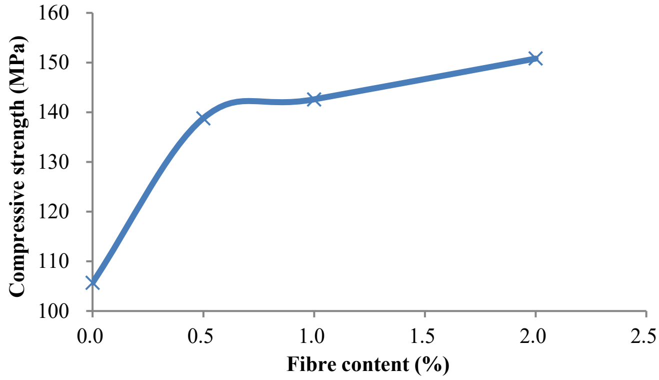

Figure 7.16. Relationship between compressive strength and fibre content.

7.2.1.2 Splitting tensile strength

Table 7.7. Peak split stress and peak deformation under various fibre contents

	Fibre content (by volume)			
	Plain	0.5%	1%	2%
Peak stress (MPa)	5.1	7.3	7.5	8.7
Peak deformation (mm)	0.024	0.171	0.167	0.821

In this subsection, concrete has a compressive strength of 60 MPa. Contact properties between concrete and fibre, properties of loading steel and plywood are the same as those in subsection 7.1.5. Similar to compression strength, with the increase of steel fibre content both peak split stress and peak deformation improve as displayed in Figure 7.17. The model with 2% steel fibre by volume has a much higher peak split stress and peak deformation than the other three models, indicating splitting tensile toughness of SFRCs could be dramatically enhanced by adding enough steel fibres. Figure 7.18 plots relationship between splitting tensile strength and fibre content, and Table 7.7 lists the peak split stress and peak deformation under various fibre contents. As can be seen from Table 7.7, the model with 2vol% steel fibre has a 71% improvement in split stress compared to the plain model. An experimental study (Goaiz et al. 2018) on an SFRC with compressive strength of 50 MPa showed a 61% and 108% increase in direct tensile strength for specimens with 1.5vol% and 3vol% steel fibre respectively.

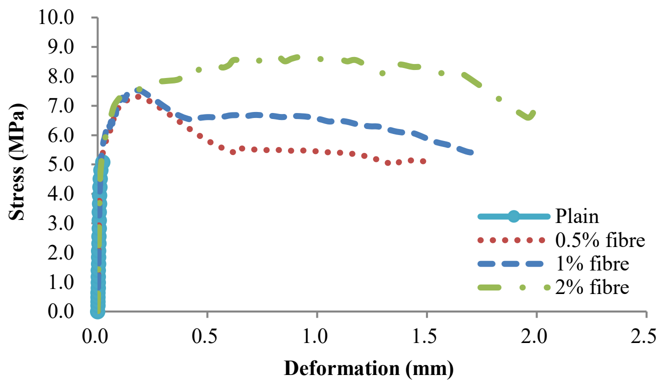

Figure 7.17. Split stress versus deformation under different fibre contents.

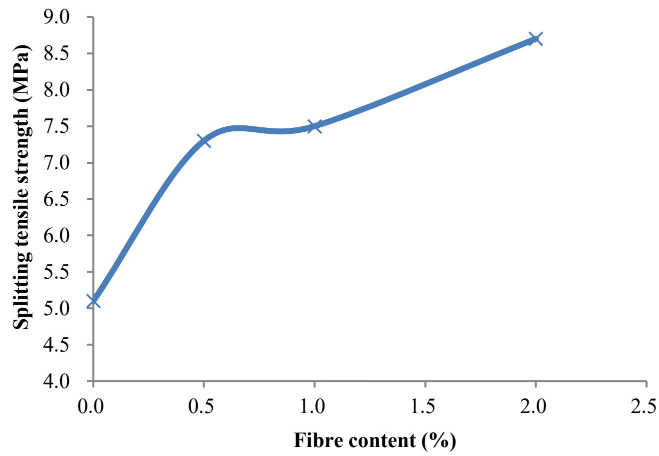

Figure 7.18. Relationship between splitting tensile strength and fibre content.

7.2.2 Study on effect of fibre length (aspect ratio) on properties of SFRCs

Four 150 mm cubic models with fibre content 1% by volume but different fibre lengths, i.e. 30, 40, 50 and 60 mm, are simulated in this subsection. All fibres have a diameter of 0.9 mm, and other parameters of fibre are listed in Table 7.1.

7.2.2.1 Compressive strength

In this subsection, high strength concrete has the ingredients as reported in Table 7.2 and parameters of bond-slip contact are listed in Table 7.3. With a diameter of 0.9 mm, fibres in length of 30, 40, 50, 60 mm have an aspect ratio of 33.3, 44.4, 55.6, 66.7, respectively. Figure 7.19 shows curves of compressive strength versus strain for these four models reinforced with fibres with different lengths, and Figure 7.20 depicts the relationship between compressive strength and fibre aspect ratio. Table 7.8 lists peak compressive strength and peak strain for the four cases. It can be seen with the increase of fibre length or aspect ratio, compressive strength increases slightly from 132.6 to 138.2 MPa, while there is no such trend for peak strain. A similar trend was also found by Su et al. (Su et al. 2016).

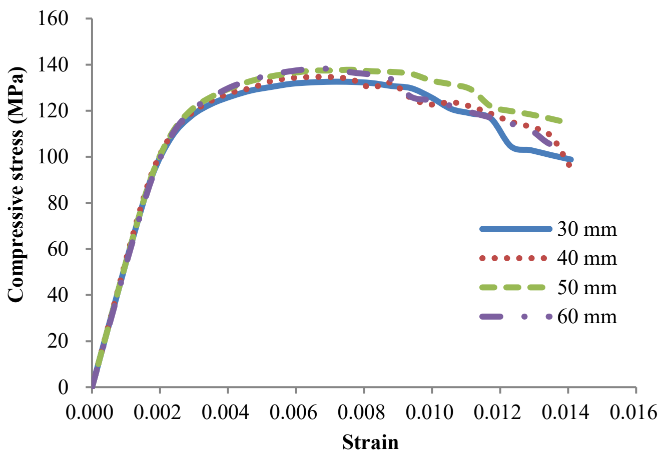

Figure 7.19. Compressive strength versus strain under different fibre lengths.

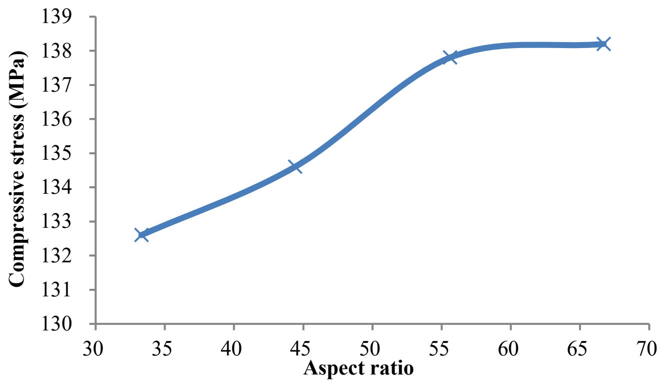

Figure 7.20. Relationship between compressive strength and fibre aspect ratio.

Table 7.8. Peak compressive strength and peak strain under various fibre lengths

	Fibre length (mm) / Aspect ratio			
	30/33.3	40/44.4	50/55.6	60/66.7
Peak strength (MPa)	132.6	134.6	137.8	138.2
Peak strain (10^{-3})	7.0	6.5	7.6	6.5

7.2.2.2 Splitting tensile strength

In this subsection, concrete has a compressive strength of 60 MPa. Contact properties between concrete and fibre, properties of loading steel and plywood are the same as those in subsection 7.1.5. Curves of split stress versus deformation under different fibre lengths are shown in Figure 7.21 and the relationship between splitting tensile strength and fibre aspect ratio is shown in Figure 7.22. As can be seen with fibre length varying from 30 mm to 60 mm (or aspect ratio from 33.3 to 66.7), splitting tensile strength has a slight improvement from 5.94 MPa to 6.32 MPa. However, the difference of softening branches between them is much more notable as displayed in Figure 7.21. Models with longer (or larger aspect ratio) fibres have higher splitting tensile toughness.

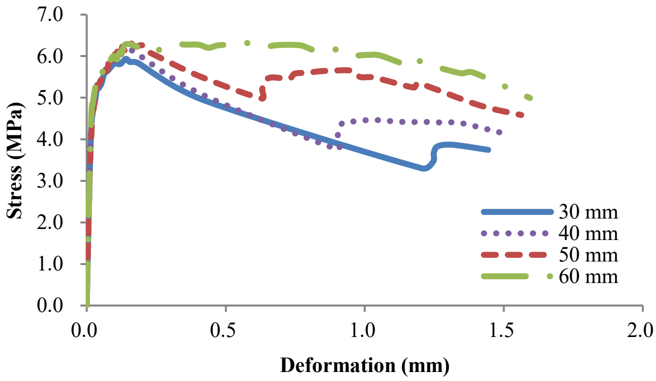

Figure 7.21. Split stress versus deformation under different fibre lengths.

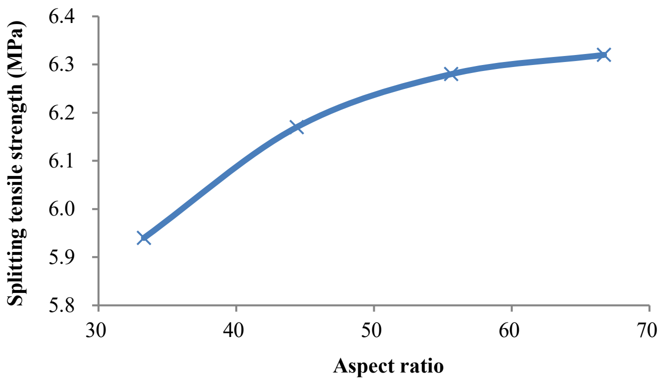

Figure 7.22. Relationship between splitting tensile strength and fibre aspect ratio.

7.3 Summary

In this chapter, a 3D meso-scale model is proposed. Simulations of uniaxial compression, flexural tension and splitting tension are conducted so that the model is successfully verified. Then, parameter study is carried out on effect of steel fibre on properties of SFRCs. The following conclusions can be drawn:

- Delaunay triangulation proves to be an effective tool for unstructured mesh of SFRC models. In other words, it enables randomly distributed fibres to have an appropriate link with concrete matrix.
- The Delaunay triangulation program is designed so as to deal with situations where fibre endpoints are right on the model surface. An advantage of this is the developed model can simulate specimens cut from an SFRC block, which contributes to better

accuracy and efficiency.

- Slide line contact has the capability to truly reflect the interfacial behaviour of fibre and mortar, which is explicitly modelled in this work.
- It is found that both fibre content and fibre aspect ratios have a positive effect on the compressive strength and splitting tensile strength of SFRCs.

CHAPTER 8

CONCLUSIONS AND RECOMMENDATIONS

8 CONCLUSIONS AND RECOMMENDATIONS

8.1 Summary and conclusions

8.1.1 Development of UHPC with high fire resistance

A UHPC with excellent fire resistance has been successfully developed and comparison was made among a total of six UHPC mixtures using quartz sand or steel slag as fine aggregate, with or without steel fibre, PP fibre or hybrid fibre. Mass loss was analysed and special attention was paid to explosive spalling of the UHPCs subjected to elevated temperatures since UHPCs are usually of compact structure and thus vulnerable to explosive spalling. Besides, residual compressive strengths and stress-strain relationships of the UHPC mixtures are discussed after they were heated to elevated temperatures up to 1,000 °C. To better understand the mechanism of relationship between behaviour of the UHPCs and temperature, SEM analysis was also conducted. Based on the test results and analyses, the following conclusions could be drawn:

- Most mass loss of the mixtures with PP fibre happened between 200 °C and 400 °C due to water evaporation and PP volatilisation.
- Heating rate had little effect on explosive spalling occurrence of the UHPC, which had very dense matrix without PP fibres. However, higher heating rate could result in more intense explosive spalling.
- Vapour pressure was a significant contribution to explosive spalling. PP fibre was an effective additive to control explosive spalling, though failed to eliminate it completely. Steel fibre could reduce the probability and intensity of spalling resulting from thermal stress and incompatibility between aggregate and cement paste.
- A UHPC mixture with excellent fire-resistance properties was successfully developed. After being exposed to 1,000 °C, it retained 69% of its original compressive strength, much higher than the existing concretes. Reinforced with hybrid fibre, this concrete also greatly decreased the occurrence of explosive spalling.
- Addition of steel slag to UHPC mixtures reduced amount of CH formed during hydration. With rough surface, steel slag could improve ITZ properties of UHPCs

exposed to elevated temperatures. Having high thermal stability and similar chemical compositions to cement, steel slag as fine aggregate also relieved thermal incompatibility between aggregate and cement paste. These features of steel slag may significantly improve residual properties of UHPCs using steel slag as fine aggregate.

8.1.2 Dynamic properties of the UHPC with high fire resistance

To further study combined effect of impact loading and high temperature, dynamic compressive tests and dynamic splitting tensile tests were carried out on the above newly developed UHPC with high fire resistance. The tests were done using an electricity-furnace-integrated SHPB system, either under high temperatures or after cooling down. Comparisons were made between these two scenarios, as well as between compressive strength and tensile strength under coupled effect of temperature and impact loading. Based on the tests, the following conclusions can be drawn:

- The UHPC had relatively high static and dynamic residual strengths after exposure to elevated temperatures.
- The highest compressive strength of the UHPC under simultaneous thermal and impact loading occurred to 600 °C, while after cooling down to room temperature the UHPC achieved its maximum strength at 400 °C both in static and dynamic compression cases.
- Tested in hot state, the UHPC suffered severe degradation in strength and rigidity under 200 °C due to great internal vapour pressure. Much less such degradation happened to the UHPC under 400 °C and no such degradation was observed above 600 °C.
- PP fibre melting at around 160 °C helped release vapour pressure and reduce explosive spalling possibility. However, PP decomposed into various volatiles between temperature range of 360 to 400 °C, increasing internal vapour pressure. In this study, most explosive spalling happened under around 370 °C. Heating rate needed to be strictly limited to prevent explosive spalling especially between 320 and 380 °C.
- The UHPC under high temperatures was softer and had lower dynamic strength than

the one cooled down to room temperature after being heated to the same temperatures as the former.

- Strain rate effect was observed on both strength and modulus of elasticity of the UHPC. With increase of strain rate, strength tended to rise while modulus of elasticity had a trend of decrease under high temperatures from 200 to 800 °C.
- In splitting tensile tests, failure of the UHPC heated to 800 °C could be induced by crush instead of splitting tension, indicating splitting tensile tests may be inappropriate for concretes at relatively high temperatures.
- Under both static and dynamic loading, splitting tensile strength fluctuated from room temperature to 400 °C and then dropped sharply beyond 400 °C. Specifically, the static splitting tensile strength fell to 41% of its original strength, but was still relatively high compared to other concretes from the literature.
- The ratio of compressive strength to splitting tensile strength fluctuated wildly with temperature increasing from 20 to 800 °C, which means taking compressive strength as the representative of the mechanical properties of a concrete at elevated temperatures is no longer acceptable. The fluctuation of the ratio under dynamic loading was smaller than static loading across the temperature range.
- The mechanism of damage induced by elevated temperature to tensile strength was different with compressive strength of the UHPC. While degradation of steel fibre weighed heavily on loss of tensile strength above 600 °C, built-up pore pressure and cracks played an important role in deterioration of compressive strength especially from 200 to 400 °C.

8.1.3 Meso-scale modelling of SFRCs/UHPCs

Applying Delaunay triangulation meshing, two 3D meso-scale models, i.e. one for thermal analysis and one for mechanical properties of UHPCs, have been successfully developed. They are able to achieve relatively high computation efficiency, as well as accuracy. Besides, the models have the potential to deal with small specimens cut from UHPC blocks. It is well known interfacial properties of steel fibre and UHPC matrix plays a great role in mechanical properties of the UHPC. To study how temperature impacts the interfacial properties, a numerical study on bond-slip behaviour of steel fibre in UHPC exposed to high temperature has also been conducted. Based on the results of these simulations, some conclusions were made as below.

<u>Meso-scale modelling of thermal properties of SFRCs/UHPCs:</u>

- The simulation reveals that presence of steel fibres has an obvious impact on the distribution of temperature and heat flux vector.
- With increase of model thickness, the simulation outcome of thermal conductivity converges rapidly. Overall, model thickness has an insignificant effect on the simulation outcomes of thermal conductivity for all the models with different fibre lengths ranging from 25 mm to 55 mm.
- It is found with increase of steel fibres, the thermal conductivity of SFRCs improves noticeably.
- As for effect of aspect ratio of steel fibres, fibre length makes a negligible impact on thermal conductivity of SFRCs, while fibre diameter affects the thermal property marginally. The model with fibres of 0.9 mm in diameter has the highest thermal conductivity among all the models with different fibre diameters but the same fibre content. The reason could be this model has fibres with a relatively large diameter which benefits heat flow along the fibres and at the same time relatively dense fibre distribution which boosts heat transfer between fibres and concrete.
- It is also found thermal conductivity of an edge section of SFRC blocks is lower than that of a middle section, and the difference grows with increase of fibre content.

<u>Meso-scale modelling of mechanical properties of SFRCs/UHPCs:</u>

- Delaunay triangulation proves to be an effective tool for unstructured mesh of SFRC models for simulating mechanical properties of SFRCs. In other words, it enables randomly distributed fibres to have an appropriate link with concrete matrix.
- The Delaunay triangulation program is designed so as to deal with situations where fibre endpoints are right on the model surface. An advantage of this is the developed model can simulate specimens cut from an SFRC block, which contributes to better

accuracy and efficiency.

- Slide line contact has the capability to truly reflect the interfacial behaviour of fibre and mortar, which is explicitly modelled in this work.
- It is found that both fibre content and fibre aspect ratio have a positive effect on the compressive strength and splitting tensile strength of SFRCs.

8.2 Recommendations and future works

It is well acknowledged that concretes especially UHPCs are vulnerable to fire or high temperatures. It is important to reduce damage and degradation of UHPCs resulting from exposure to fire or combined effect of fire and blast. Meso-scale modelling is a relatively new method to numerically investigate properties of UHPCs either under ambient temperature or elevated temperatures. This PhD project has achieved some progress in these areas but some issues remain open to resolution. Further work and some refinements are listed as the following:

- The mechanism of improved residual mechanical properties of UHPCs exposed to high temperatures by using steel slag as fine aggregate needs to be further studied.
- The effect of content of steel slag as fine aggregate in UHPCs has not been studied.
- The current meso-scale model for thermal analysis does not take into account moisture content and thermochemical behaviour that could affect thermal properties of UHPCs. Also, it is unable to consider variations of density, moisture content and porosity of SFRCs resulting from incorporation of steel fibre.
- The meso-scale model needs to be further developed and validated by using experimental data such as under impact loading, high temperature or combined effect of them.

REFERENCES

REFERENCES

Akca, A. H., and Özyurt Zihnioğlu, N. (2013). "High performance concrete under elevated temperatures." *Construction and Building Materials*, 44, 317-328.

Al-Jabri, K. S., Al-Saidy, A. H., and Taha, R. (2011). "Effect of copper slag as a fine aggregate on the properties of cement mortars and concrete." *Construction and Building Materials*, 25(2), 933-938.

Ambily, P. S., Umarani, C., Ravisankar, K., Prem, P. R., Bharatkumar, B. H., and Iyer, N. R. (2015). "Studies on ultra high performance concrete incorporating copper slag as fine aggregate." *Construction and Building Materials*, 77, 233-240.

Aslani, F., and Nejadi, S. (2012). "Bond characteristics of steel fibre reinforced self-compacting concrete." *Canadian Journal of Civil Engineering*, 39(7), 834-848.

Aslani, F., and Samali, B. (2013). "Constitutive Relationships for Steel Fibre Reinforced Concrete at Elevated Temperatures." *Fire Technology*, 50(5), 1249-1268.

Aslani, F., and Samali, B. (2013). "High Strength Polypropylene Fibre Reinforcement Concrete at High Temperature." *Fire Technology*, 50(5), 1229-1247.

ASTM (2014). "ASTM Standard E831-14, Standard test method for linear thermal expansion of solid materials by thermomechanical analysis." ASTM International, West Conshohocken, PA.

Banthia, N., Mindess, S., and Trottier, J.-F. (1996). "Impact Resistance of Steel Fiber Reinforced Concrete." *ACI Materials Journal*, 93(5), 472-479.

Bažant, Z. P., and Caner, F. C. (2005). "Microplane model M5 with kinematic and static constraints for concrete fracture and anelasticity. I: Theory." *Journal of Engineering Mechanics*, 131(1), 31-40.

Bažant, Z. P., and Caner, F. C. (2005). "Microplane Model M5 with Kinematic and Static Constraints for Concrete Fracture and Anelasticity. II: Computation." *JOURNAL OF ENGINEERING MECHANICS*, 131(1), 41-47.

Behnood, A., and Ghandehari, M. (2009). "Comparison of compressive and splitting tensile strength of high-strength concrete with and without polypropylene fibers heated to high temperatures." *Fire Safety Journal*, 44(8), 1015-1022.

Bindiganavile, V., Banthia, N., and Aarup, B. (2002). "Impact Response of Ultra-High-Strength Fiber-Reinforced Cement Composite." *ACI Materials Journal*, 99(6), 543-548.

Biskri, Y., Achoura, D., Chelghoum, N., and Mouret, M. (2017). "Mechanical and durability characteristics of High Performance Concrete containing steel slag and crystalized slag as aggregates." *Construction and Building Materials*, 150, 167-178.

Bolander, J. E., Choi, S., and Duddukuri, S. R. (2008). "Fracture of fiber-reinforced cement composites: effects of fiber dispersion." *International Journal of Fracture*, 154(1-2), 73-86.

Borouchaki, H., and Lo, S. H. (1995). "Fast Delaunay triangulation in three dimensions." *Comput. Methods Appl. Mech. Engrg.*, 128, 153-167.

Bowyer, A. (1981). "Computing Dirichlet tessellations." *The Computer Journal*, 24(2), 162-166.

Caggiano, A., Etse, G., and Martinelli, E. (2012). "Zero-thickness interface model formulation for failure behavior of fiber-reinforced cementitious composites." *Computers & Structures*, 98-99, 23-32.

Caverzan, A., Cadoni, E., and Prisco, M. d. (2013). "Dynamic tensile behaviour of high performance fibre reinforced cementitious composites after high temperature exposure." *Mechanics of Materials*, 59, 87-109.

Chan, Y. N., Luo, X., and Sun, W. (2000). "Compressive strength and pore structure of high-performance concrete after exposure to high temperature up to 800°C." *Cement and Concrete Research*, 30, 247-251.

Chan, Y. N., Luo, X., and Sun, W. (2000). "Effect of high temperature and cooling regimes on the Compressive Strength and Pore Properties of High Performance Concrete." *Construction and Building Materials*, 14, 261-266.

Chen, L., Fang, Q., Jiang, X., Ruan, Z., and Hong, J. (2015). "Combined effects of high temperature and high strain rate on normal weight concrete." *International Journal of Impact Engineering*, 86, 40-56.

Choe, G., Kim, G., Gucunski, N., and Lee, S. (2015). "Evaluation of the mechanical properties of 200MPa ultra-high-strength concrete at elevated temperatures and residual strength of column." *Construction and Building Materials*, 86, 159-168.

Corinaldesi, V., and Moriconi, G. (2012). "Mechanical and thermal evaluation of Ultra High Performance Fiber Reinforced Concretes for engineering applications." *Construction and Building Materials*, 26(1), 289-294.

Cunha, V. M. C. F., Barros, J. A. O., and Sena-Cruz, J. M. (2012). "A finite element model with discrete embedded elements for fibre reinforced composites." *Computers & Structures*, 94-95, 22-33.

Dancygier, A. N., and Yankelevsky, D. Z. (1999). "Effects of Reinforced Concrete Properties on Resistance to Hard Projectile Impact." *ACI Structural Journal*, 96(2), 259-268.

Debicki, G., Haniche, R., and Delhomme, F. (2012). "An experimental method for assessing the spalling sensitivity of concrete mixture submitted to high temperature." *Cement and Concrete Composites*, 34(8), 958-963.

Denneman, E., Kearsley, E. P., and Visser, A. T. (2011). "Splitting tensile test for fibre reinforced concrete." *Materials and Structures*, 44(8), 1441-1449.

Ducman, V., and Mladenovič, A. (2011). "The potential use of steel slag in refractory concrete." *Materials Characterization*, 62(7), 716-723.

Eurocode (2004). *EN 1992-1-2 Eurocode 2: Design of Concrete Structures*, European Committee for Standardization (CEN), Brussels.

Eurocode (2005). *EN 1993-1-2 Eurocode 3: Design of steel structures*, European Committee for Standardization (CEN), Brussels.

Faiyadh, F. I., and AI-Ausi, M. A. (1989). "Effect of elevated temperature on splitting tensile strength of fibre concrete." *The Intemational Journal of Cement Composites and Lightweight Concrete*, 11(3), 175-178.

Fang, Q., and Zhang, J. (2013). "Three-dimensional modelling of steel fiber reinforced concrete material under intense dynamic loading." *Construction and Building Materials*, 44, 118-132.

Gül, R., Okuyucu, E., Türkmen, İ., and Aydin, A. C. (2007). "Thermo-mechanical properties of fiber reinforced raw perlite concrete." *Materials Letters*, 61(29), 5145-5149.

Gal, E., and Kryvoruk, R. (2011). "Meso-scale analysis of FRC using a two-step homogenization approach." *Computers & Structures*, 89(11-12), 921-929.

Gallé, C. (2001). "Effect of drying on cement-based materials pore structure as identified by mercury intrusion porosimetry: A comparative study between oven-, vacuum-, and freeze-drying." *Cement and Concrete Research*, 31, 1467-1477.

Ganesan, N., Indira, P. V., and Sabeena, M. V. (2014). "Bond stress slip response of bars embedded in hybrid fibre reinforced high performance concrete." *Construction and Building Materials*, 50, 108-115.

Ganjian, E. (1990). "The relationship between porosity and thermal conductivity of concrete." PhD, The University of Leeds.

Gao, D., Li, X., Yang, S., and Wang, Q. (2012). "Splitting properties of fibre reinforced ground granulated blast furnace slag concrete after high temperature (in Chinese)." *Concrete*, 271(5), 133-137.

Gao, D., Zhao, J., and Tang, J. (2004). "Experimental study on the dimensional effect of steel fiber reinforced high-strength concrete (SFRHSC) under splitting tension (in Chinese)." *Journal of Building Materials*, 7(3), 295-298.

Gao, D., Zhao, J., and Tang, J. (2005). "An experimental study on the behavior of fiber reinforced high-strength concrete under splitting tension (in Chinese)." *China Civil Engineering Journal*, 2005(7), 21-26.

Goaiz, H. A., Farhan, N. A., Sheikh, M. N., Yu, T., and Hadi, M. N. S. (2018). "Experimental Evaluation of Tensile Strength Test Methods for Steel Fibre Reinforced Concrete." *Magazine of Concrete Research*, 1-42.

Grote, D. L., Park1, S. W., and Zhou, M. (2001). "Dynamic behavior of concrete at high strain rates and pressures: I. experimental characterization." *International Journal of Impact Engineering*, 25, 869-886.

Guo, X., Shi, H., and Wu, K. (2014). "Effects of steel slag powder on workability and durability of concrete." *Journal of Wuhan University of Technology-Mater. Sci. Ed.*, 29(4), 733-739.

Häfner, S., Eckardt, S., Luther, T., and Könke, C. (2006). "Mesoscale modeling of concrete: Geometry and numerics." *Computers & Structures*, 84(7), 450-461.

Hager, I. (2013). "Behaviour of cement concrete at high temperature." *Bulletin of the Polish Academy of Sciences: Technical Sciences*, 61(1), 145-154.

Hrynyk, T. D., and Vecchio, F. J. (2014). "Behavior of Steel Fiber-Reinforced Concrete Slabs under Impact Load." *ACI Structural Journal*, 111(5), 1213-1223.

Huo, J. S., He, Y. M., and Chen, B. S. (2013). "Experimental study on impact behaviour of concrete-filled steel tubes at elevated temperatures up to 800 °C." *Materials and Structures*, 47(1-2), 263-283.

Huo, J. S., He, Y. M., Xiao, L. P., and Chen, B. S. (2012). "Experimental study on dynamic behaviours of concrete after exposure to high temperatures up to 700 °C." *Materials and Structures*, 46(1-2), 255-265.

ISO (1999). "ISO 834-1-1999 (E), Fire-resistance tests - Elements of building construction - Part 1: General requirements." International Organization for Standardization, Geveve.

Israngkura Na Ayudhya, B. (2015). "Comparison of compressive and splitting tensile strength of autoclaved aerated concrete (AAC) containing water hyacinth and polypropylene fibre subjected to elevated temperatures." *Materials and Structures*, 49(4), 1455-1468.

Jia, B. (2011). "Static and Dynamic Mechanical Behavior of Concrete at Elevated Temperature (in Chinese)." Doctor Doctoral dissertation, College of Civil Engineering of Chongqing University.

Jin, F., Xu, J., Fan, F., and Su, H. (2013). "Strength Property of Steel Fiber Reinforced Concrete at Elevated Temperature (in Chinese)." *Bulletin of the Chinese Ceramic Society*, 32(4).

Kahanji, C., Ali, F., and Nadjai, A. (2016). "Experimental study of ultra-high performance fibre reinforced concrete under ISO 834 fire." *Structures in Fire (Proceedings of the Ninth International Conference)*.

Kahanji, C., Ali, F., and Nadjai, A. (2016). "Explosive spalling of ultra-high performance fibre reinforced concrete beams under fire." *Journal of Structural Fire Engineering*, 7(4), 328-348.

Kakogiannis, D., Pascualena, F., Reymen, B., Pyl, L., Ndambi, J. M., Segers, E., Lecompte, D., Vantomme, J., and Krauthammer, T. (2013). "Blast performance of reinforced concrete hollow core slabs in combination with fire: Numerical and experimental assessment." *Fire Safety Journal*, 57, 69-82.

Khaliq, W., and Kodur, V. (2011). "Thermal and mechanical properties of fiber reinforced high performance self-consolidating concrete at elevated temperatures." *Cement and Concrete Research*, 41(11), 1112-1122.

Khaliq, W., and Kodur, V. K. R. (2011). "Effect of High Temperature on Tensile Strength of Different Types of High-Strength Concrete." *ACI Materials Journal*, 108(4), 394-402.

Khoury, G. A., Grainger, B. N., and Sullivan, P. J. E. (1985). "Transient thermal strain of concrete: literature review, conditions within specimen and behaviour of individual constituent." *Magazine of Concrete Research*, 37(132), 131-144.

Kodur, V., and Khaliq, W. (2011). "Effect of Temperature on Thermal Properties of Different Types of High-Strength Concrete." *Journal of Materials in Civil Engineering*, 23(6), 793-801.

Kodur, V. K. R., and Sultan, M. A. (2003). "Effect of Temperature on Thermal Properties of High-Strength Concrete." *Journal of Materials in Civil Engineering*, 15, 101-107.

Lau, A., and Anson, M. (2006). "Effect of high temperatures on high performance steel fibre reinforced concrete." *Cement and Concrete Research*, 36(9), 1698-1707.

Lee, O. S., Choi, H., and Kim, H. (2011). "High-temperature dynamic deformation of aluminum alloys using SHPB." *Journal of Mechanical Science and Technology*, 25(1), 143-148.

Lee, Y. W., Kim, G. Y., Gucunski, N., Choe, G. C., and Yoon, M. H. (2015). "Thermal strain behavior and strength degradation of ultra-high-strength-concrete." *Materials and Structures*, 49(8), 3411-3421.

Li, H., Wang, Y., Xie, H., and Zheng, W. (2012). "Microstructure analysis of reactive powder concrete after exposed to high temperature (in Chinese)." *J. Huazhong Univ. of Sci. & Tech. (Natural Science Edition)*, 40(5), 71-75.

Li, J., Wu, C., and Hao, H. (2015). "An experimental and numerical study of reinforced ultra-high performance concrete slabs under blast loads." *Materials & Design*, 82, 64-76.

Li, X. (2001). "Sliver-free Three Dimensional Delaunay Mesh Generation." PhD, University of Illinois at Urbana Champaign, Urbana Illinois.

Liang, X., Wu, C., Su, Y., Chen, Z., and Li, Z. (2018). "Development of ultra-high performance concrete with high fire resistance." *Construction and Building Materials*, 179, 400-412.

Lie, T. T., and Kodur, V. K. R. (1995). "Effect of temperature on thermal and mechanical properties of steel fibre reinforced concrete." Insititute for Research in Construction, National Research Council Canada, Canada.

Lin, W. M., Lin, T. D., and Powers-Couche, L. J. (1996). "Microstructures of fire-damaged concrete." *ACI Materials Journal*, 93(3), 199-205.

Liu, C. X., Li, Y. L., Wu, Z., Guo, W. G., and Ge, Y. Z. (2011). "Dynamic Compression Behavior of Heated Concrete (in Chinese)." *CHINA CIVIL ENGINEERING JOURNAL*, 44(4), 78-83

Liu, X. R., Zhu, Y. H., Zhou, L., and Chen, S. J. (2009). "Analysis of reinforcement mechanism of interfacial stress within SFRC (in Chinses)." *China Concrete and Cement Products*(165).

LS-DYNA (2013). *Keyword Users Manual*, LSTC.

Ma, Q., Guo, R., Zhao, Z., Lin, Z., and He, K. (2015). "Mechanical properties of concrete at high temperature—A review." *Construction and Building Materials*, 93, 371-383.

Mahmud, G. H., Yang, Z., and Hassan, A. M. T. (2013). "Experimental and numerical studies of size effects of Ultra High Performance Steel Fibre Reinforced Concrete (UHPFRC) beams." *Construction and Building Materials*, 48, 1027-1034.

Marfia, S., and Sacco, E. (2003). "Numerical techniques for the analysis of crack propagation in cohesive materials." *International Journal for Numerical Methods in Engineering*, 57(11), 1577-1602.

Mendes, A., Sanjayan, J., and Collins, F. (2007). "Phase transformations and mechanical strength of OPC/Slag pastes submitted to high temperatures." *Materials and Structures*, 41(2), 345-350.

Miloud, B. (2005). "Permeability and porosity characteristics of steel fiber reinforced concrete." *Asian Journal of Civil Engineering (Building and Housing)*, 6(4), 317-330.

Nagy, B., Nehme, S. G., and Szagri, D. (2015). "Thermal Properties and Modeling of Fiber Reinforced Concretes." *Energy Procedia*, 78, 2742-2747.

Nagy, B., and Szagri, D. (2016). "Hygrothermal Properties of Steel Fiber Reinforced Concretes." *Applied Mechanics and Materials*, 824, 579-588.

Netinger, I., &, M. J. R., Bjegović, D., and Mladenovič, A. (2012). "Concrete containing steel slag aggregate: Performance after high temperature exposure." *Concrete Repair, Rehabilitation and Retrofi tting III*, Taylor & Francis Group, London.

Netinger, I., Bjegović, D., and Vrhovac, G. (2011). "Utilisation of steel slag as an aggregate in concrete." *Materials and Structures*, 44(9), 1565-1575.

Netinger, I., Varevac, D., Bjegović, D., and Morić, D. (2013). "Effect of high temperature on properties of steel slag aggregate concrete." *Fire Safety Journal*, 59, 1-7.

Novák, J., and Kohoutková, A. (2017). "Fire response of Hybrid Fiber Reinforced Concrete to High Temperature." *Procedia Engineering*, 172, 784-790.

Nyström, U., and Gylltoft, K. (2011). "Comparative numerical studies of projectile impacts on plain and steel-fibre reinforced concrete." *International Journal of Impact Engineering*, 38(2-3), 95-105.

Okpala, D. C. (1989). "Pore structure of hardened cement paste and mortar." *The InternationaI Journat of Cement Composite$ and Lightweight Concrete*, 11(4), 245-254.

Oliver, J., Mora, D. F., Huespe, A. E., and Weyler, R. (2012). "A micromorphic model for steel fiber reinforced concrete." *Int J Solids Struct*, 49(21), 2990-3007.

Peng, G.-F., Yang, W.-W., Zhao, J., Liu, Y.-F., Bian, S.-H., and Zhao, L.-H. (2006). "Explosive spalling and residual mechanical properties of fiber-toughened high-performance concrete subjected to high temperatures." *Cement and Concrete Research*, 36(4), 723-727.

Poon, C. S., Shui, Z. H., and Lam, L. (2004). "Compressive behavior of fiber reinforced high-performance concrete subjected to elevated temperatures." *Cement and Concrete Research*, 34(12), 2215-2222.

Pros, A., Diez, P., and Molins, C. (2012). "Modeling steel fiber reinforced concrete: numerical immersed boundary approach and a phenomenological mesomodel for concrete-fiber interaction." *International Journal for Numerical Methods in Engineering*, 90(1), 65-86.

Pyo, S., and Kim, H.-K. (2017). "Fresh and hardened properties of ultra-high performance concrete incorporating coal bottom ash and slag powder." *Construction and Building Materials*, 131, 459-466.

Qasrawi, H., Shalabi, F., and Asi, I. (2009). "Use of low CaO unprocessed steel slag in concrete as fine aggregate." *Construction and Building Materials*, 23(2), 1118-1125.

Qiu, Y., and Liang, J. (2009). "Comparison between Simulated Value and Measured Value of Thermal Conductivity Coefficient of LDPE/Graphite Composite." *Plastics Technology*, 37(8), 38-41.

Rashad, A. M., Bai, Y., Basheer, P. A. M., Collier, N. C., and Milestone, N. B. (2012). "Chemical and mechanical stability of sodium sulfate activated slag after exposure to elevated temperature." *Cement and Concrete Research*, 42(2), 333-343.

Rong, Z., Sun, W., and Zhang, Y. (2010). "Dynamic compression behavior of ultra-high performance cement based composites." *International Journal of Impact Engineering*, 37(5), 515-520.

Schauffert, E. A., and Cusatis, G. (2012). "Lattice discrete particle model for fiber-reinforced concrete. I: Theory." *Journal Of Engineering Mechanics*, 138(7), 826-833.

Shannag, M. J., Brincker, R., and Hansen, W. (1997). "Pullout behavior of steel fibers from cement-based composites." *Cement and Concrete Research*, 27(6), 925-936.

Shi, Y., Li, Z.-X., and Hao, H. (2009). "Bond slip modelling and its effect on numerical analysis of blast-induced responses of RC columns." *Structural Engineering and Mechanics*, 32(2), 251-267.

Sobia, A. Q., Hamidah, M. S., Azmi, I., and Rafeeqi, S. F. A. (2015). "Elevated temperature resistance of ultra-high-performance fibre-reinforced cementitious composites." *Magazine of Concrete Research*, 67(17), 923-937.

Soetens, T., Van Gysel, A., Matthys, S., and Taerwe, L. (2013). "A semi-analytical model to predict the pull-out behaviour of inclined hooked-end steel fibres." *Construction and Building Materials*, 43, 253-265.

Sovják, R., Vavřiník, T., Zatloukal, J., Máca, P., Mičunek, T., and Frydrýn, M. (2015). "Resistance of slim UHPFRC targets to projectile impact using in-service bullets." *International Journal of Impact Engineering*, 76, 166-177.

Su, H. Y., Xu, J. Y., and Ren, W. B. (2014). "Experimental study on the dynamic compressive mechanical properties of concrete at elevated temperature." *Materials & Design*, 56, 579-588.

Su, Y., Li, J., Wu, C., Wu, P., and Li, Z.-X. (2016). "Effects of steel fibres on dynamic strength of UHPC." *Construction and Building Materials*, 114, 708-718.

Su, Y., Li, J., Wu, C., Wu, P., and Li, Z.-X. (2016). "Influences of nano-particles on dynamic strength of ultra-high performance concrete." *Composites Part B: Engineering*, 91, 595-609.

Su, Y., Li, J., Wu, C., Wu, P., Tao, M., and Li, X. (2017). "Mesoscale study of steel fibre-reinforced ultra-high performance concrete under static and dynamic loads." *Materials & Design*, 116, 340-351.

Su, Y., Wu, C., Li, J., Li, Z.-X., and Li, W. (2017). "Development of novel ultra-high performance concrete: From material to structure." *Construction and Building Materials*, 135, 517-528.

Tanyildizi, H., and Coskun, A. (2008). "The effect of high temperature on compressive strength and splitting tensile strength of structural lightweight concrete containing fly ash." *Construction and Building Materials*, 22(11), 2269-2275.

Tsuchiya, Y., and Sumi, K. (1969). "Thermal decomposition products of polypropylene." *Journal of Polymer Science: Part A-1*, 7, 1599-1607.

Tuyan, M., and Yazıcı, H. (2012). "Pull-out behavior of single steel fiber from SIFCON matrix." *Construction and Building Materials*, 35, 571-577.

Wang, Z., Xu, j., Fan, J., and Yin, Y. (2014). "Study on Energy Absorption Properties of Steel Fibre Reinforced Concrete at Elevated Temperatures (in Chinese)." *Concrete*, 292, 14-17.

Wang, Z. M., Kwan, A. K. H., and Chan, H. C. (1999). "Mesoscopic study of concrete I: generation of random aggregate structure and finite element mesh." *Computers & Structures*, 70, 533-544.

Watson, D. F. (1981). "Computing the n-dimensional Delaunay tessellation with application to Voronoi polytopes." *The Computer Journal*, 24(2), 167-172.

Wu, C., Oehlers, D. J., Rebentrost, M., Leach, J., and Whittaker, A. S. (2009). "Blast testing of ultra-high performance fibre and FRP-retrofitted concrete slabs." *Engineering Structures*, 31(9), 2060-2069.

Wu, Y., Crawford, J. E., Lan, S., and Magallanes, J. M. (2014). "Validation Studies for Concrete Constitutive Models with Blast Test Data." *13th International LS-*

DYNA Users Conference.

Wu, Y., Crawford, J. E., and Magallanes, J. M. (2012). "Performance of LS-DYNA® Concrete Constitutive Models." *12th International LS-DYNA® Users Conference*.

Wu, Z., Li, H., Wang, H., and Wu, X. (2008). "Numerical simulation and discussion of the dynamic splitting test." *Journal of Hefei University of Technology*, 31(10), 1676-1679.

Xargay, H., Folino, P., Sambataro, L., and Etse, G. (2018). "Temperature effects on failure behavior of self-compacting high strength plain and fiber reinforced concrete." *Construction and Building Materials*, 165, 723-734.

Xiong, M.-X., and Liew, J. Y. R. (2016). "Mechanical behaviour of ultra-high strength concrete at elevated temperatures and fire resistance of ultra-high strength concrete filled steel tubes." *Materials & Design*, 104, 414-427.

Xiong, M., and Liew, R. J. Y. (2015). "Spalling behavior and residual resistance of fibre reinforced Ultra-High performance concrete after exposure to high temperatures." *Materiales de Construcción*, 65(320), e071.

Xu, M., and Wille, K. (2014). "Calibration of K&C Concrete Model for UHPC in LS-DYNA." *Advanced Materials Research*, 1081, 254-259.

Xu, Z., Hao, H., and Li, H. N. (2012). "Mesoscale modelling of fibre reinforced concrete material under compressive impact loading." *Construction and Building Materials*, 26(1), 274-288.

Yüksel, İ., Siddique, R., and Özkan, Ö. (2011). "Influence of high temperature on the properties of concretes made with industrial by-products as fine aggregate replacement." *Construction and Building Materials*, 25(2), 967-972.

Yang, E.-H., Wang, S., Yang, Y., and Li, V. C. (2008). "Fiber-bridging constitutive law of engineered cementitious composites." *Journal of Advanced Concrete Technology*, 6(1), 181-193.

Yang, Q. (2005). *Constrained Delaunay Triangulation Meshing Technique*, Publishing House of Electronics Industry, Beijing.

Yang, S., and Ba, H. (2009). "Split Hopkinson Bar Measurements of Steel Fiber Reinforced Concrete Exposed to High Temperature (in Chinese)." *Journal of China University of Mining & Technology*, 38(4), 562-565.

Zhang, J., Liu, Z., and Liu, W. (2007). "Experimental Research on Natural Convective Coefficient of Concrete Surface (in Chinese)." *Sichuan Building Science*, 33(5), 143-146.

Zhao, Z., Jing, L., Pei, Q., Ma, H. W., and Wang, Z. H. (2016). "An Experimental Study of the Dynamic Split Tension Properties of Reinforced Concrete." *Strength of Materials*, 48(1), 63-68.

Zheng, W., Li, H., and Wang, Y. (2012). "Compressive behaviour of hybrid fiber-reinforced reactive powder concrete after high temperature." *Materials & Design*, 41, 403-409.

Zhu, W. C., Bai, Y., Li, X. B., and Niu, L. L. (2012). "Numerical simulation on rock failure under combined static and dynamic loading during SHPB tests." *International Journal of Impact Engineering*, 49, 142-157.

APPENDICES

APPENDIX A (CHAPTER 3)

Figure A.1. Compression test setup.

Figure A.2. 1000 kN capacity electrohydraulic servo pressure testing machine.

Figure A.3. Water tank with thermostatic control.

Figure A.4. Mixer.

Figure A.5. Mixing agitator.

Figure A.6. Sieves.

Figure A.7. Electric furnace.

Figure A.8. Steel mould.

Table A.1. Mass record during drying

Sample No	Time 1	Mass 1 (kg)	Time 2	Mass 2 (kg)	Time 3	Mass 3 (kg)
5	16:00 18/02/2017	0.311	9:00 19/02/2017	0.31	17:00 19/02/2017	0.310
7-1		0.318		0.317		0.317
7-2		0.314		0.313		0.313
8-1		0.316		0.313		0.313
8-2		317		0.314		0.314

Table A.2. Effect of duration of curing in hot water on compression strength

Admixture	Duration of curing in hot water	Temperature (°C)	Compression strength (MPa)	Improvement (%)
Q-0	9–10/02/2017	90	104	2.30
Q-0	9–11/02/2017	90	106.4	
S-0	9–10/02/2017	90	79.4	3.70
S-0	9–11/02/2017	90	82.3	

Table A.3. Data of compression test for admixture Q-0

Duration of drying (h)	Temperature (°C)	Sample No	Force (kN)	Compression strength (Mpa)
24	20	1-1	232	93
		1-2	284.97	113,6
		1-3	381.66	153
		1-4	285.78	114
	200	6-1	463.84	186
		6-2	413.39	165
		6-3	436	174
		6-4	392.1	157
0	20 (24h hot water curing)	1-1	350.5	140.2
		1-2	260.06	104
		1-3	240.81	96
	20 (48h hot water curing)	1-1	243.8	97.5
		1-2	266.7	106.7
		1-3	379.67	152
	Standard curing	1-1	310.85	124
		1-2	255.44	102

Table A.4. Data of compression test for admixture Q-S

Duration of drying (h)	Temperature (°C)	Sample No	Force (kN)	Compression strength (Mpa)
24	20	2-21	431.24	172
		2-22	450.6	180
		2-23	479.75	192
		2-24	469.75	188
	200	5-1	482.94	193
		5-2	515.52	206
		5-3	531.6	213
		5-4	526.17	210

Table A.5. Data of compression test for admixture Q-P

Duration of drying (h)	Temperature (°C)	Sample No	Force (kN)	Compression strength (Mpa)
24	20	14-20	318.18	127
		14-21	366.87	147
		14-22	308.35	123
	200	12-1	297.43	119
		12-2	427.6	171
		12-3	337.93	135
	400	12-4	408.68	163
		12-5	353.52	141
		12-6	404.6	162
		12-7	428.06	171
	600	12-8	281.12	112
		12-9	91.83	37
		12-10	276.94	111
		12-11	218.85	88
	800	12-12	44.69	18
		12-13	25.92	10
		12-14	96.78	39
		12-15	76.38	31
	1000	14-16	53.08	21
		14-17	94.32	38
		14-18	39.52	16
		14-19	84.79	34

Table A.6. Data of compression test for admixture Q-SP

Duration of drying (h)	Temperature (°C)	Sample No	Force (kN)	Compression strength (Mpa)
24	20	13-20	378.67	151
		13-21	406.39	163
		13-22	418.13	167
		11-23	424.9	170
	200	11-1	431.51	173
		11-2	445.25	178
		11-3	435.17	174
	400	11-4	582.56	233
		11-5	532.89	213
		11-6	569.74	228
		11-7	N/A	
	600	11-8	383.33	153
		11-9	404.88	162
		11-10	384.71	154
		11-11	352.95	141
	800	11-12	96.1	38
		13-13	94.12	38
		13-14	99.96	40
		11-15	92.29	37
	1000	13-16	103.06	41
		13-17	88.86	36
		13-18	101.05	40
		11-19	100	40

Table A.7. Data of compression test for admixture S-0

Duration of drying (h)	温度	Sample No	Force (kN)	Compression strength (Mpa)
24	20	8-13	246.53	99
		8-14	245.02	98
		8-15	216.36	87
		8-16	230.69	92
	200	7-1	498.49	199
		7-2	516.97	207
		7-3	444.86	178
		7-4	395.17	158
0	20 (24h hot water curing)	8-1	190.6	76.2
		8-2	198.47	79.8
		8-3	238.04	95
	20 (48h hot water curing)	8-1	202.16	80.9
		8-2	205.76	82.3
		8-3	243.94	98
	Standard curing	8-1	216.72	87
		8-2	216.65	87

Table A.8. Data of compression test for admixture S-SP

Duration of drying (h)	Temperature (°C)	Sample No	Force (kN)	Compression strength (Mpa)
24	20	3-21	408.26	163
		4-22	469.82	188
		4-23	337.26	135
		4-24	439.23	176
	200	4-1	458.72	183
		4-2	439.3	176
		3-3	480.04	192
		3-4	465.2	186
	400	4-5	586.9	235
		4-6	561.65	225
		3-7	565.7	226
		3-8	550.06	220
	600	3-9	535.2	214
		3-10	553.3	221
		4-11	508.73	203
		3-12	521.64	209
	800	3-13	337.68	151
		4-14	375.89	150
		4-15	387.85	155
		4-16	266.03	106
	1000	4-17	298.29	119
		3-18	298.42	119
		3-19	238.38	95
		3-20	264.34	106

APPENDIX B (CHAPTER 4 & 5)

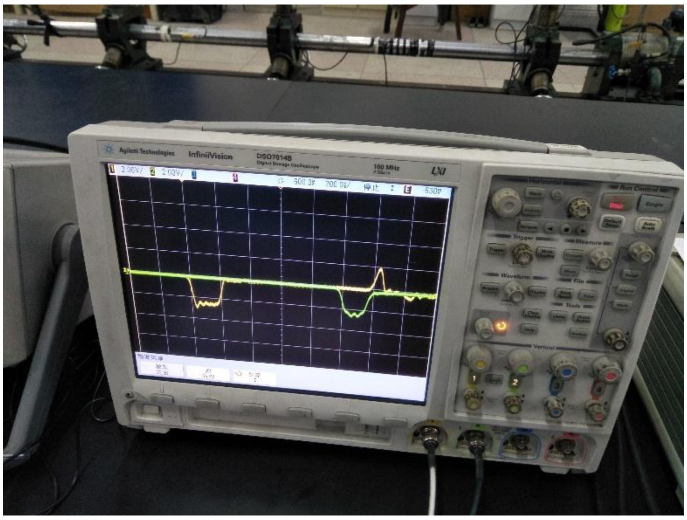

Figure B.1. DSO7014B oscilloscope

Figure B.2. Constant-temperature drying oven

Table B.1. Record of SHPB waves for 20 °C compressive tests

Gas pressure (MPa)	Specimen #1	Specimen #2	Specimen #3
0.25	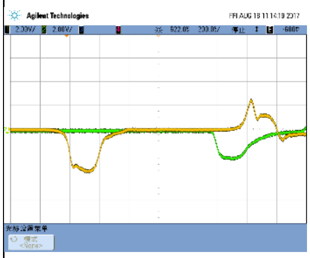	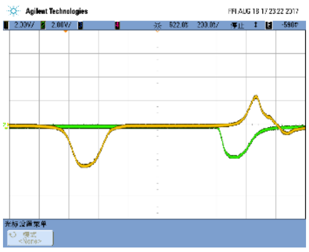	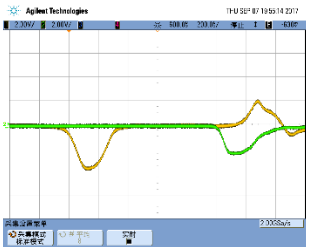
0.3	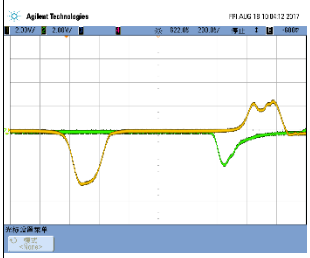	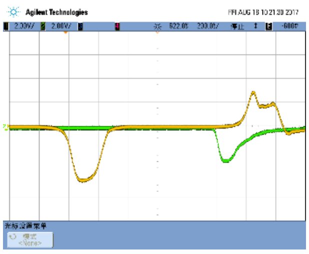	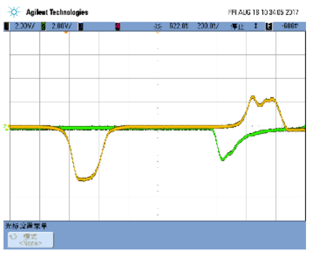
0.35	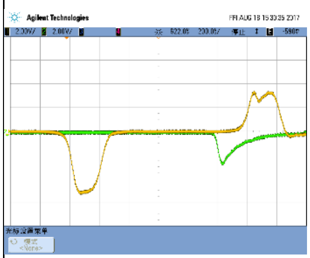	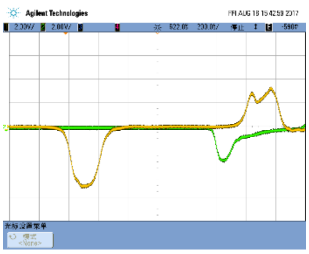	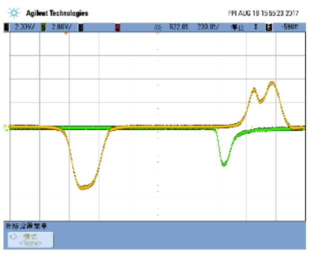
0.4	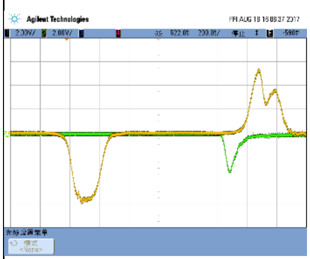	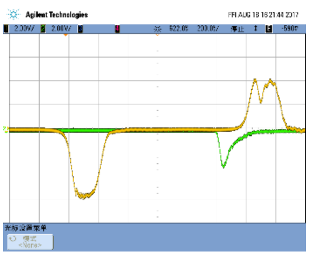	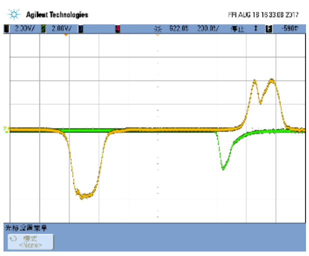
0.45	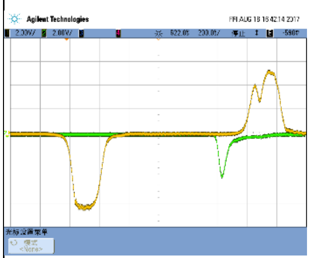	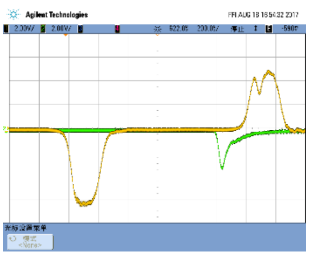	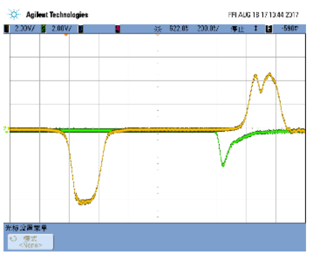

Table B.2. Record of SHPB waves for 200 °C compressive tests

Gas pressure (MPa)	Specimen #1	Specimen #2	Specimen #3
0.25	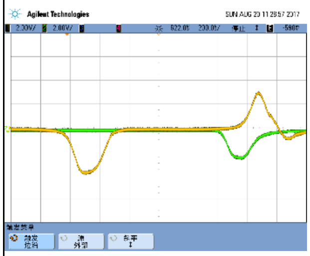	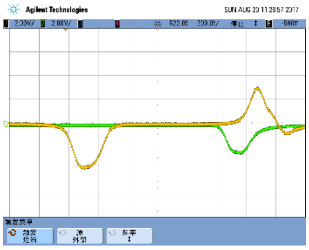	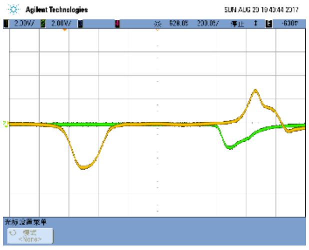
0.3	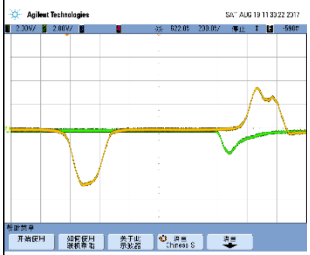	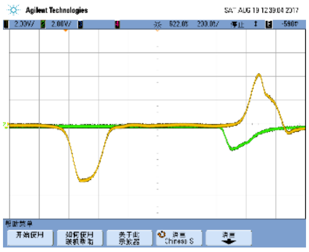	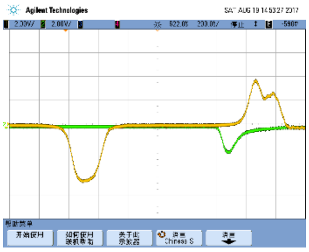
0.35	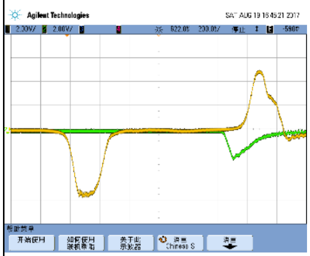	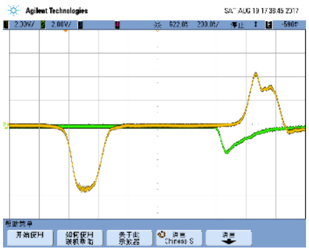	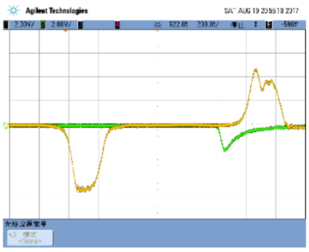
0.4	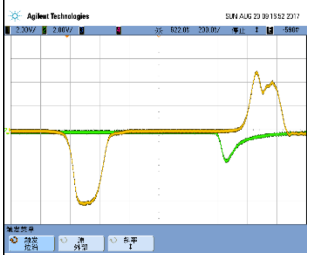	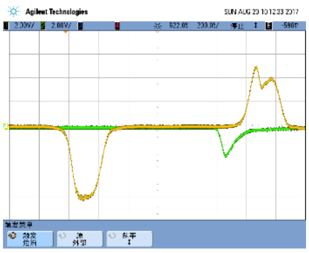	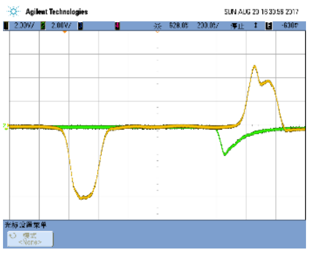
0.45	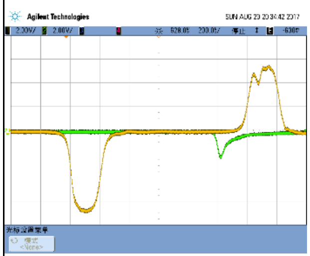	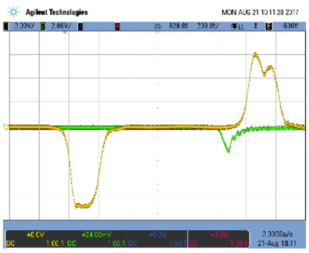	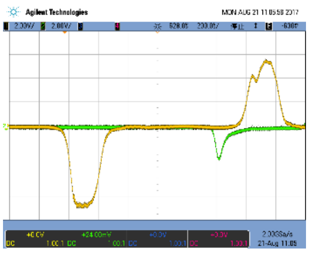

Table B.3. Record of SHPB waves for 400 °C compressive tests

Gas pressure (MPa)	Specimen #1	Specimen #2	Specimen #3
0.25	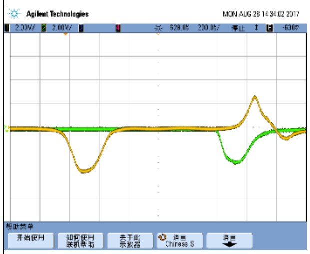		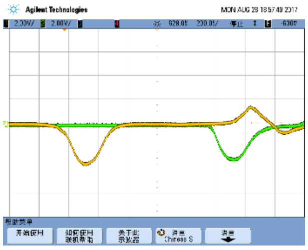
0.3	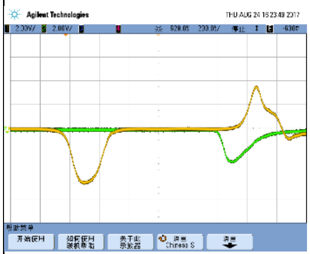	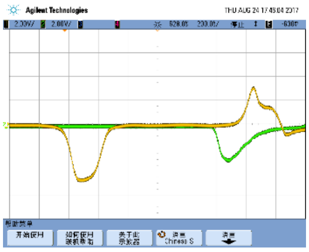	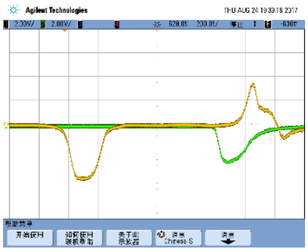
0.35	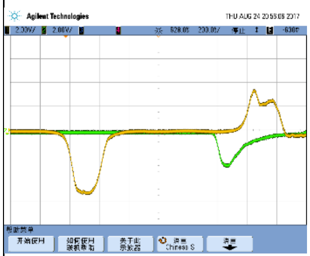	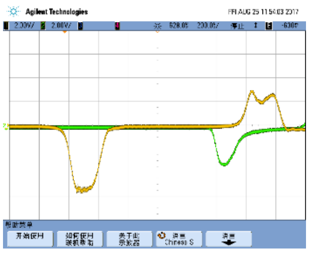	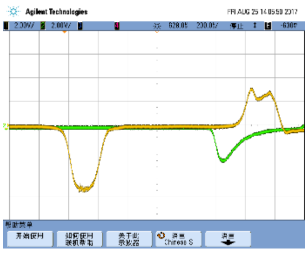
0.4	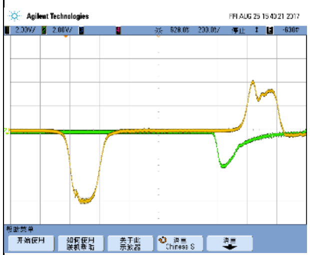	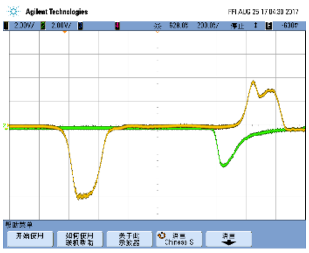	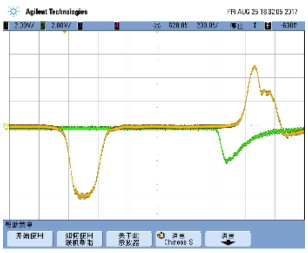
0.45	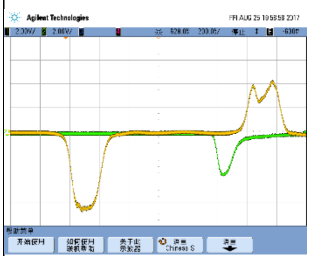	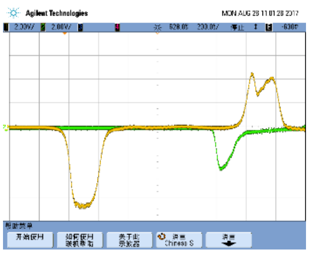	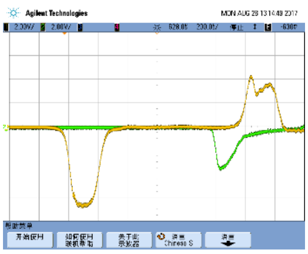

Table B.4. Record of SHPB waves for 600 °C compressive tests

Gas pressure (MPa)	Specimen #1	Specimen #2	Specimen #3
0.25	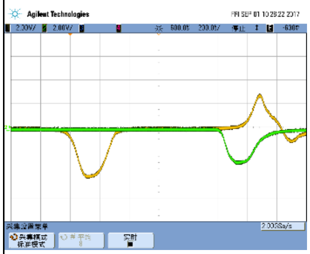	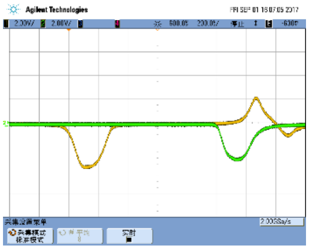	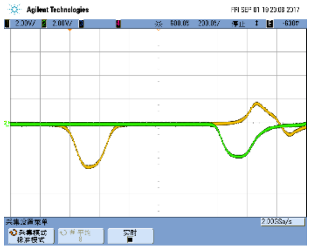
0.3	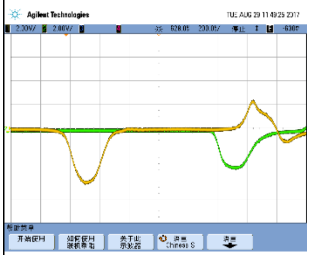	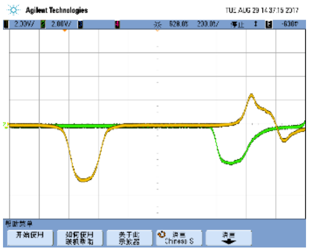	
0.35	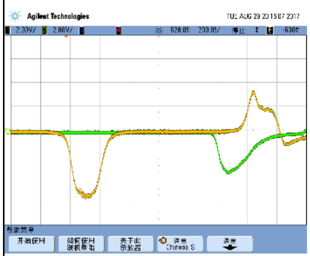	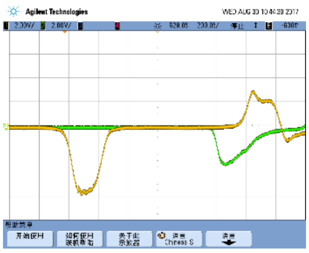	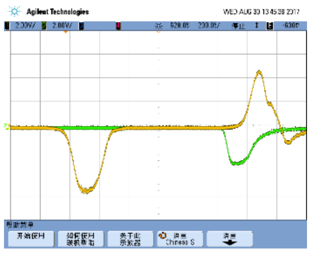
0.4	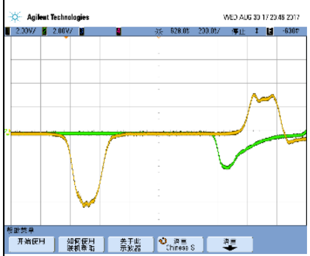	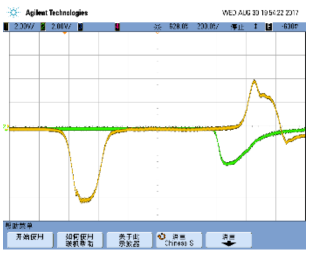	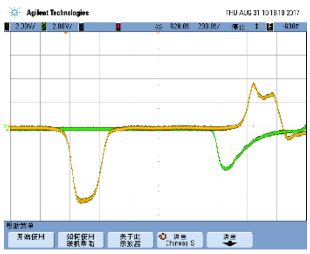
0.45	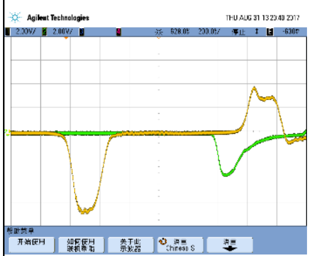		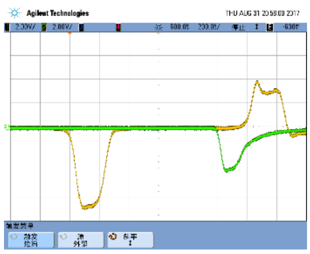

Table B.5. Record of SHPB waves for 800 °C compressive tests

Gas pressure (MPa)	Specimen #1	Specimen #2	Specimen #3
0.25	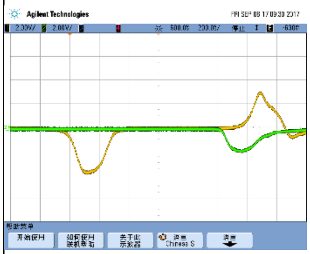	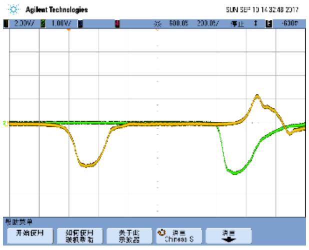	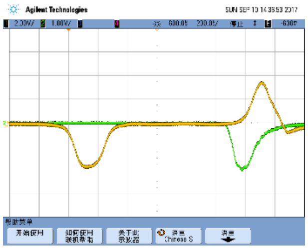
0.3	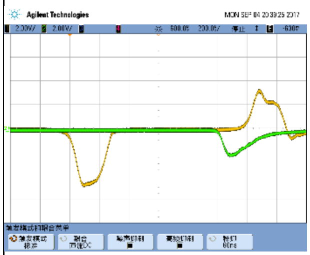		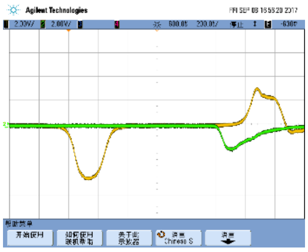
0.35	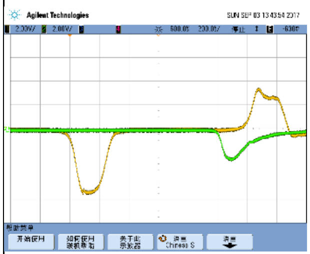	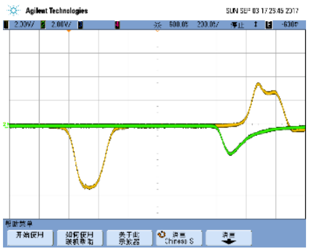	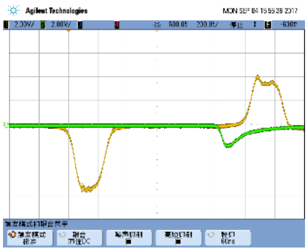
0.4	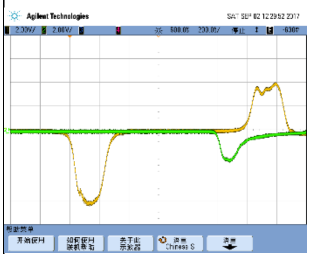	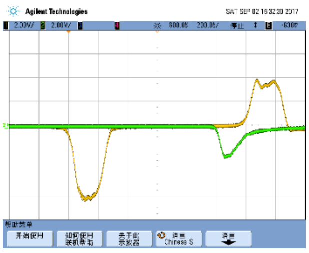	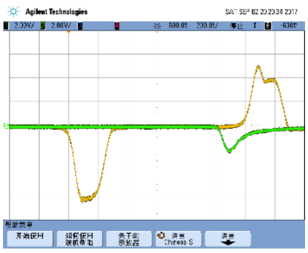
0.45	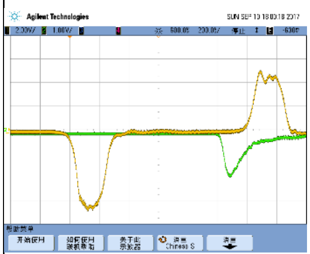	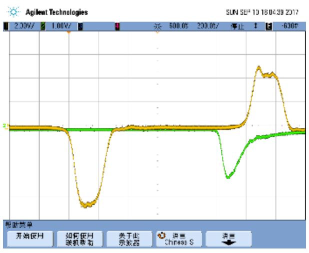	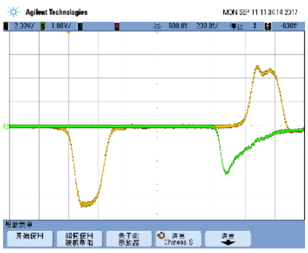

Table B.6. Record of SHPB waves for 20 °C splitting tensile tests

Gas pressure (MPa)	Specimen #1	Specimen #2	Specimen #3
0.15	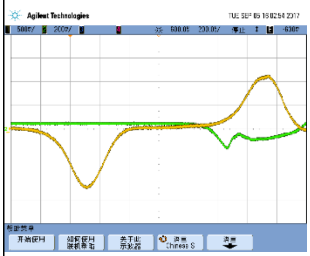	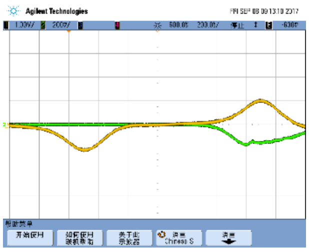	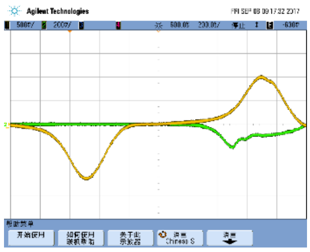
0.2	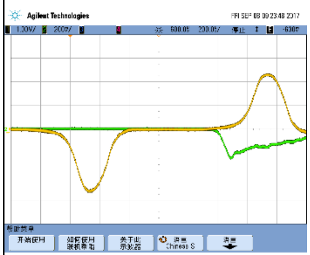	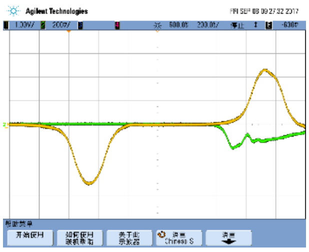	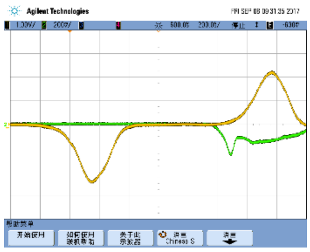
0.25	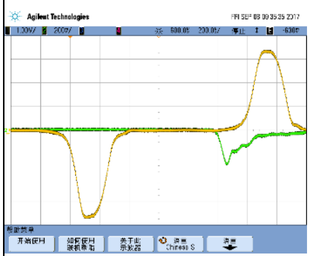	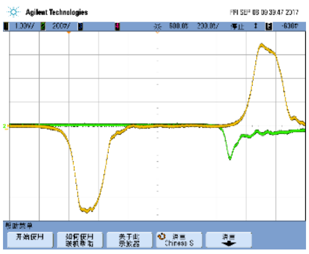	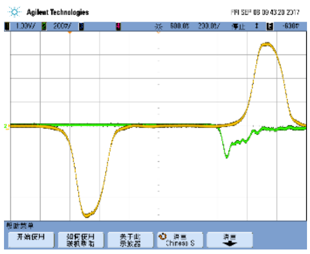

Table B.7. Record of SHPB waves for 200 °C splitting tensile tests

Gas pressure (MPa)	Specimen #1	Specimen #2	Specimen #3
0.15	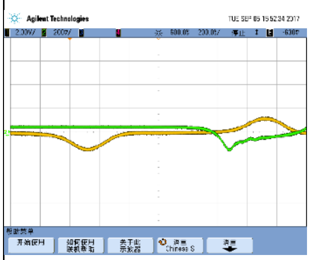	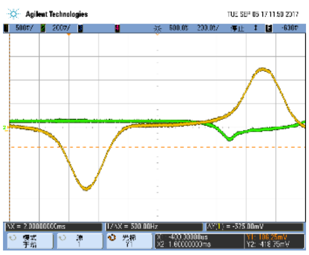	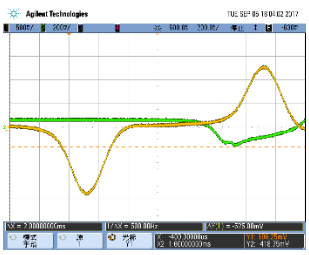
0.2	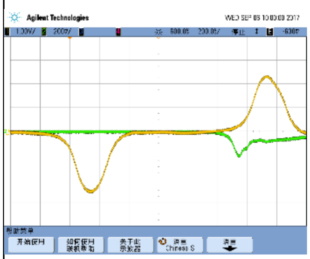	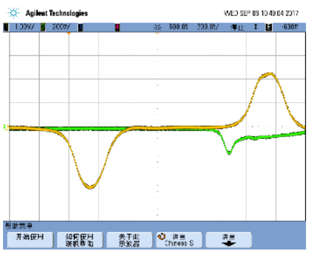	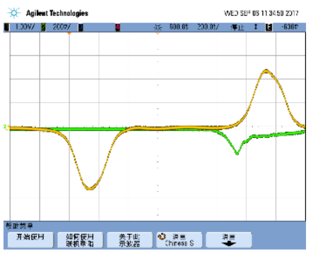
0.25	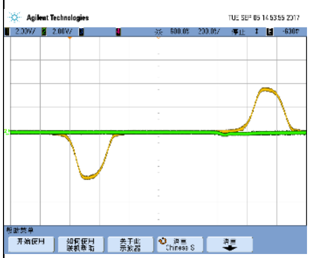	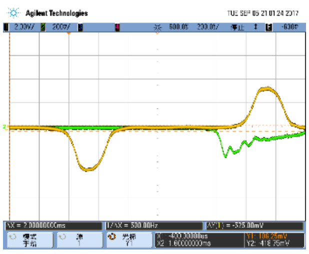	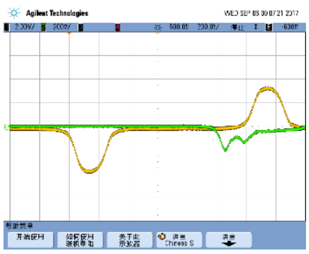

Table B.8. Record of SHPB waves for 400 °C splitting tensile tests

Gas pressure (MPa)	Specimen #1	Specimen #2	Specimen #3
0.15	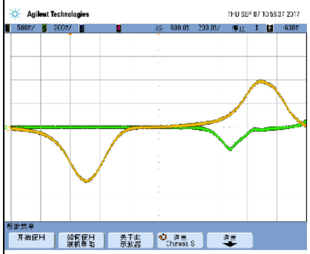	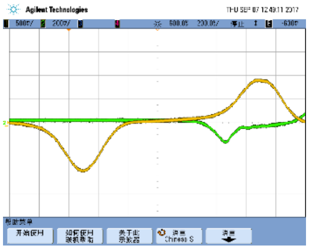	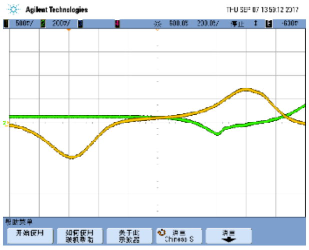
0.2	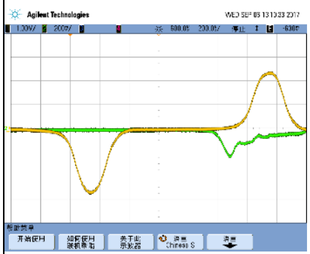	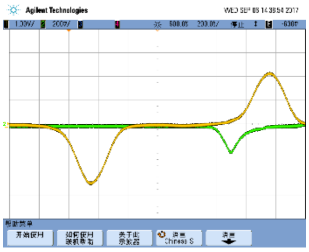	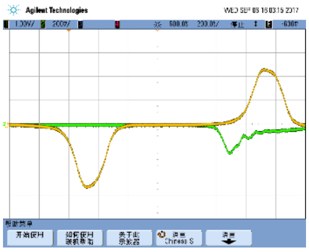
0.25	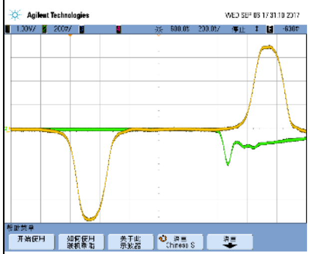	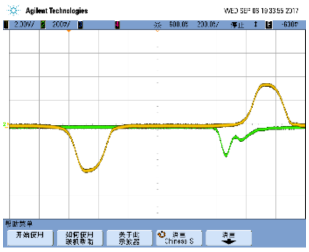	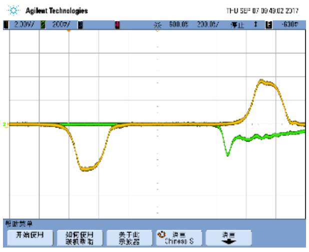

Table B.9. Record of SHPB waves for 600 °C splitting tensile tests

Gas pressure (MPa)	Specimen #1	Specimen #2	Specimen #3
0.15	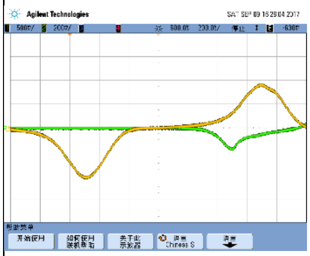	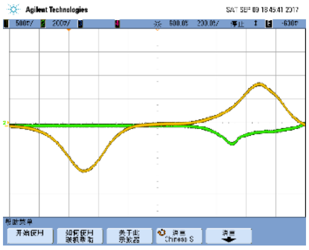	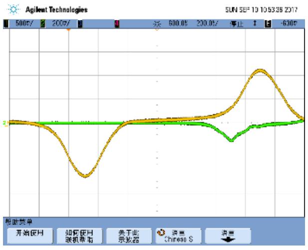
0.2	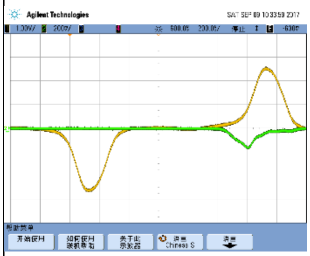	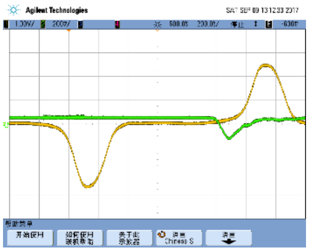	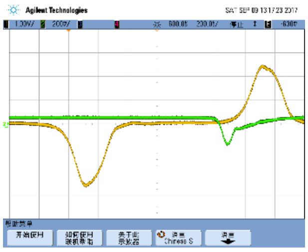
0.25	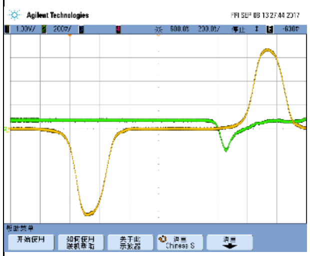	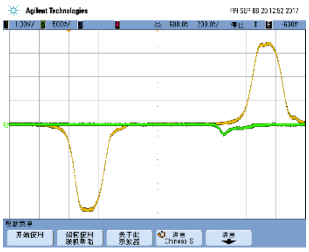	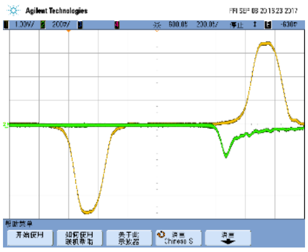

Table B.10. Record of SHPB waves for 800 °C splitting tensile tests

Gas pressure (MPa)	Specimen #1	Specimen #2	Specimen #3
0.15	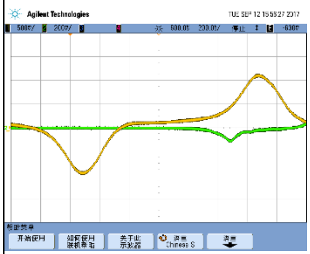	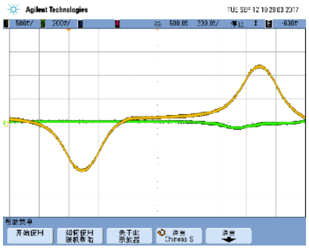	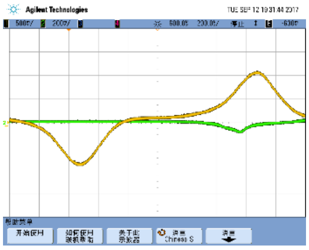
0.2	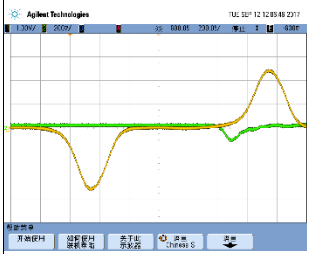	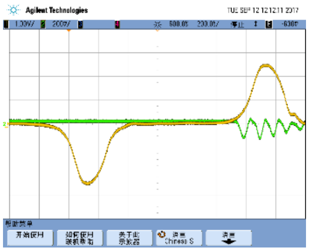	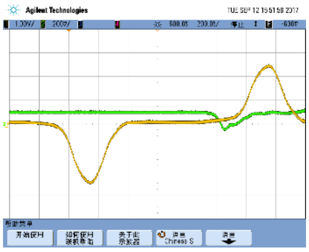
0.25